Dissertation

# Compact realizations of optical super-resolution microscopy for the life sciences

Alice Sandmeyer

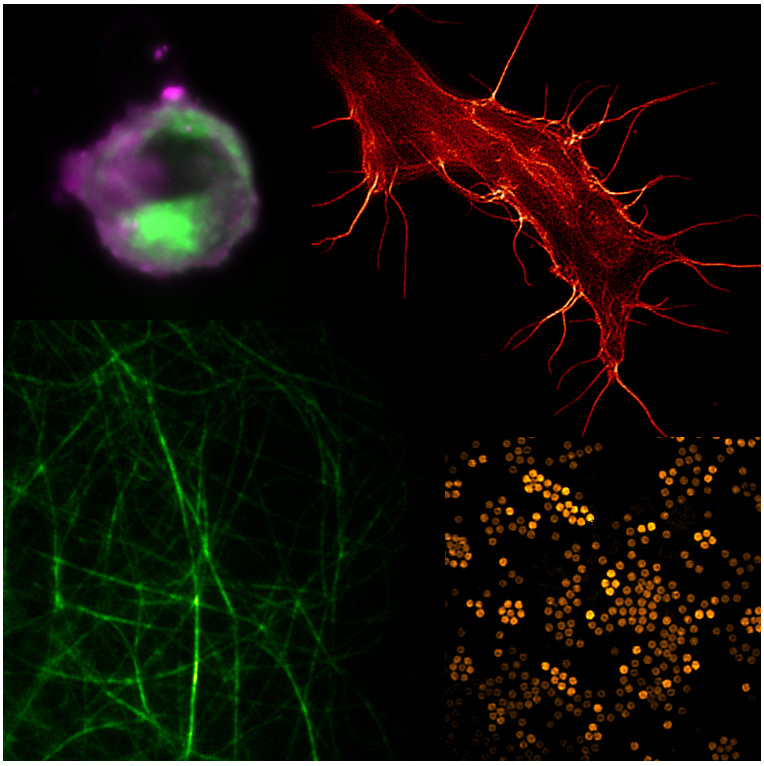

Bielefeld University
Faculty of Physics

Dissertation

# Compact realizations of optical super-resolution microscopy for the life sciences

*Author:*
Alice Sandmeyer
(geb. Wilking)

October 31, 2019

Referees:
Prof. Dr. Thomas Huser
Prof. Dr. Andreas Hütten

*Printed on non-aging paper DIN ISO 9706*

# Summary

In physics, the ability to break fundamental barriers and limits is one of the main challenges and most desired achievements. In the case of optical microscopy, the diffraction limit as described by Abbe can be mitigated by so-called super-resolution microscopy techniques. In the last decades, several approaches to overcome Abbe's limit were developed and continuously improved to cover a wide range of applications in research fields such as the biomedical and life sciences. Such high-end microscope systems are, however, often located in centralized and shared research facilities as they are cost-intensive to purchase and operate. Therefore, for many researchers there is currently no easy access to advanced fluorescence microscopy methods if they cannot readily access those specialized facilities or purchase and operate dedicated instruments. In this thesis, three fluorescence microscopy methods were developed as compact and cost-efficient systems in an effort to democratize them, i.e. making these advanced methods more widely accessible to the scientific community.

Conventional fluorescence microscopy methods provide a spatial resolution of about 200 nm using high-NA oil immersion objectives. This is sufficient for several applications, and therefore, the first project focused on constructing a wide-field microscope which was used to image the infection pathway of HIV-1 in living samples. Further, fast 3D data acquisition was implemented to visualize the dynamics of HIV particles and fast image processing via deconvolution increased the quality of the obtained results. The suitable environment for these experiments, however, is at the Icahn School of Medicine at Mount Sinai in New York City. To facilitate this in a collaborative fashion, the microscope was designed with a very small footprint, so that it could easily be shipped to the United States. To observe the transfer of individual virus particles with a diameter of approximately 120 nm, however, super-resolution microscopy is required. Here, fixed HIV-1 samples were analyzed by super-resolution structured illumination microscopy to confirm the previous results.

The cost of scientific-grade cameras contributes a significant portion to the total cost of an advanced imaging system. By exchanging these cameras with cost-effective industry-grade cameras, this overall cost can be tremendously decreased.

Such low-cost alternatives have to be carefully characterized and tested - to determine whether they are suitable for super-resolution microscopy and if they can provide comparable data quality. For the work at hand, the performance of industry-grade CMOS cameras for their use in conventional fluorescence microscopy and super-resolution optical fluctuation imaging (SOFI) was analyzed qualitatively and quantitatively - using super-resolution image quality metrics. By directly comparing these cameras to scientific-grade CMOS cameras both mounted to a scientific microscope, the image quality was analyzed and evaluated by conducting live-cell imaging experiments of parts of the cytoskeleton in Cos-7 cells and the same experiments were also carried out on the compact microscope described above.

In a final step, a setup that facilitates cost-effective super-resolution structured illumination microscopy (SIM) was developed. SIM also provides the capability of super-resolution imaging by illuminating the sample with an illumination pattern exhibiting a periodicity at the limit of what can still be resolved by a conventional microscope. By shifting the phase and angle of this sinusoidal intensity pattern, and by reconstructing the raw images utilizing a signal processing algorithm, super-resolution information at twice the spatial resolution of a conventional microscope can be obtained. To optimize image reconstruction with minimal artifacts, the illumination pattern has to be of high contrast, and therefore the generation of the pattern is a crucial parameter. In this thesis, a digital micromirror device was precisely analyzed and utilized for the creation of the pattern. The cost-effective industry-grade camera and a low-cost laser were also employed, which resulted in an overall reduction of the costs of the system by a factor of approximately ten in comparison to commercial systems. Imaging actin filaments and lysosomes in fixed cell samples, and visualizing the dynamics of mitochondria and the endoplasmic reticulum in living cells demonstrated that the structured illumination microscope developed here can easily compete with commercial implementations - with additional benefits, such as instant image reconstruction. To this end, also the internal morphology of smart microgels was used as a test bed to demonstrate the extensive application range of cost-effective super-resolution microscopes.

# Contents

# 1. Introduction and motivation

Fluorescence microscopy has become one of the standard imaging methods in the life sciences to visualize structures and dynamics in cells and even living organisms. The main advantage of fluorescence microscopy is its ability to precisely identify and locate molecules of interest by labeling them with fluorescent probes. This allows us to study basic functions and processes from single cells to model organism such as mice and fish through imaging [1].

The resolution achieved in classical fluorescence microscopy is limited to approximately 200 nm. This limit, described first by Abbe [2] in 1873 is fundamental rather than technical, as it is caused by the diffraction of light. For various applications this resolution is sufficient to analyze research questions [3] in applications such as the characterization of macromolecular complexes and viruses [4] all the way to in-vivo brain studies [5]. For structures on the nanometer-scale, however, so-called super-resolution microscopy is required. Super-resolution optical microscopy techniques, also called *nanoscopy*, circumvent Abbe's limit and the pioneers in this field were awarded with the Nobel prize in Chemistry in 2014 [6].

The super-resolution optical imaging techniques can be divided into four classes: One early member is STED [7] (stimulated emission depletion), which utilizes a doughnut-shaped beam to stimulate the emission of fluorescent probes and shape the laser focus even sharper. Another early member is SMLM (single molecule localization microscopy), which localizes the center of the emission spot generated by a single "blinking" fluorescent molecule. The first member of the class of SMLM techniques is PALM [8] (photo-activated localization microscopy), which, together with STED, was awarded the above mentioned Nobel prize. Other SMLM methods such as dSTORM [9, 10] (direct stochastic optical reconstruction microscopy) or PAINT [11] (point accumulation for imaging in nanoscale topography) also localize the center of the emission spot of fluorescent molecules, but employ different techniques to create the blinking of the fluorescent dyes. Similar to SMLM are techniques which are based on the analysis of the fluctuation time trace of fluorescent dyes, where SOFI [12] (super-resolution optical fluctuation imaging) is the most prominent method. The last class of super-resolution optical imaging techniques is SIM [13, 14] (structured illumination microscopy), which utilizes a sinusoidal

illumination pattern in the sample, which is rotated and shifted to reconstruct a super-resolved image. Ongoing developments of these techniques have improved various aspects such as their spatial and temporal resolution, life-cell compatibility and reduced system complexity. Further, combinations among the classes and combinations with other fluorescent microscopy and spectroscopy methods increased the application range of fluorescence microscopy even more [1, 15].

Most importantly, to perform a successful measurement with fluorescence microscopy, the right technique has to be chosen to match the requirements of the experiment [1]. Although SMLM provides very high spatial resolution, it lacks live-cell compatibility and imaging speed. STED, on the other side, does also allow for a spatial resolution of under 50 nm and is live-cell compatible, but requires high laser powers which often induces cell death and phototoxicity during the imaging experiments. SIM is well suitable for live-cell imaging, but its spatial resolution cannot compete with SMLM or STED. Therefore, it would be best if researchers in the life sciences could have access to a wide variety of fluorescence microscopy techniques.

A large number of commercial systems for fluorescence microscopy that also incorporate super-resolution techniques exist, but for a single research group or small facilities even the cost of installing and operating just one advanced imaging system is often too much, not to mention the cost of several systems. Thus, various concepts were developed to *democratize* fluorescence microscopy. Here, cost-efficient and easy to replicate solutions [16] are designed so that a wide range of scientists can have access to techniques such as dSTORM [17, 18] or advanced wide-field microscopy [19, 20] in order to perform their experiments. Today, the importance of having access to high-performance and super-resolution imaging methods is widely recognized in the scientific community [21].

While most approaches to super-resolution fluorescence microscopy aim to provide a higher spatial resolution, this work focuses on constructing and providing compact and cost-efficient solutions to advanced fluorescence microscopy. By designing such systems, there is the potential that more scientists will have access to these advanced fluorescence microscopy techniques. To this end, the microscopes constructed in the course of this work are user-friendly and to some extend easy to replicate.

For the first system, a conventional fluorescence microscope was built that could be shipped to our collaborators in Benjamin K. Chen's laboratory at the Icahn School of Medicine at Mount Sinai (ISMMS) in New York City. At ISMMS the infection pathway of HIV-1 (human immunodeficiency virus) is being investigated

and visualized. Therefore, the main aspect of this project was to create a compact microscope which is portable and robust. This requires a high-speed 3D fluorescence imaging system, which the group did not have access to. Several studies showcased that conventional wide-field microscopy is sufficient to image the virus particles during their transfer from infected to uninfected cells [22, 23]. With further image processing, namely image deconvolution, the quality of the recorded images can be improved. If, however, single virus particles are supposed to be resolved, super-resolution imaging is required [24]. Therefore, fixed, HIV-1 infected samples were analyzed at the Biomolecular Photonics group in Bielefeld using 3D-SIM in order to confirm the results obtained by live-cell imaging at ISMMS.

For the compact fluorescence microscope, industry-grade cameras are employed in order to reduce the overall system costs. These cameras proved to be sufficient for dSTORM imaging [18] and now, for the second project, these cameras were also tested to evaluate their performance in super-resolution optical fluctuation imaging (SOFI) [12]. First, the direct comparison to scientific-grade cameras was needed in order to quantify and evaluate imaging results obtained by the industry-grade camera. The direct comparison was carried out on a dedicated scientific microscope. To further reduce the overall costs, our custom-built conventional fluorescence microscope was also tested to perform SOFI experiments with the industry-grade camera.

For the final project, a compact and cost-efficient SIM system was constructed. In this system a digital micromirror device (DMD) was utilized to generate the sinusoidal pattern in the sample. DMDs are not straightforward to use for SIM, and therefore, their physical properties were first investigated in order to perform SIM imaging. Again, an industry-grade camera was utilized for image acquisition and a low-cost laser, which is usually used for light show applications, was employed as a light source. The construction contains no complicated components and even the control software is freely available [25] so that the system could be reproduced by microscopists all over the world. To demonstrate that the system is fully functional, quantitative analysis of calibration samples was performed. Further, fixed and live cell samples were imaged and even samples from chemistry were analyzed.

The structure of this thesis is as follows: First, an introduction to the relevant theoretical background is given in chapter 2 that includes all the super-resolution methods used in this work. In chapter 3 the conventional fluorescence microscope is described in detail and the visualization results of HIV-1 are presented. The further development of the compact system in order to perform SOFI is portrayed in chapter 4. The design and construction of the compact and cost-efficient SIM

microscope with subsequent imaging is presented in chapter 5. Most of the results shown in chapters 3 to 5 have already been published in peer-reviewed articles and the corresponding articles are referenced at the beginning of each chapter. Lastly, an overall conclusion and outlook is given in chapter 6.

# 2. Theoretical background

The main area application for fluorescence microscopy is to image structures that are precisely labeled with fluorescent dyes. There is a wide range of applications, such as in biology, medicine and chemistry, and therefore fluorescence microscopy has become a standard method. The fluorescent dyes operate as probes, so that information about structures and dynamics can be gained [1].

## 2.1. Basics of fluorescence

The physical process of fluorescence is the absorption and emission of a photon with the specific energy $E$,

$$E = h\nu = \frac{hc}{\lambda}, \tag{2.1}$$

where $h$ is Planck's constant, $c$ the speed of light, $\nu$ the frequency and $\lambda$ the wavelength of the photon. If eq. (2.1) matches with the energy difference between the singlet ground-state $S_0$ and one of the excited states $S_1$ or $S_2$, the energy of the photon $E_A$ will be absorbed and the atom or molecule is in a higher electronic state (fig. 2.1a) [26]. In case it is a molecule, the vibrational and rotational state might also change to a higher one. Due to internal conversion, as described by the Born-Oppenheimer approximation, the electron loses energy in a non-radiant way and relaxes to the vibrational ground state [27, 28]. Within the time scale of a few nanoseconds, the electron then returns to the ground state under the emission of a photon with the energy $E_F$. This process is called fluorescence. Since $E_F < E_A$, the wavelength of the emitted photon is red-shifted, also known as the Stokes shift [29].

In contrast to fluorescence, the process of phosphorescence has a longer lifetime. Here, the electron changes from $S_1$ to the triplet state $T_1$ which is called intersystem crossing. The change of the spin is forbidden due to the Pauli principle but may occur because of spin-orbit coupling. Additionally, the return to the singlet ground state $S_0$ also exhibits a change of the spin, and therefore the typical timescale of phosphorescence is in the order of milliseconds [27–29].

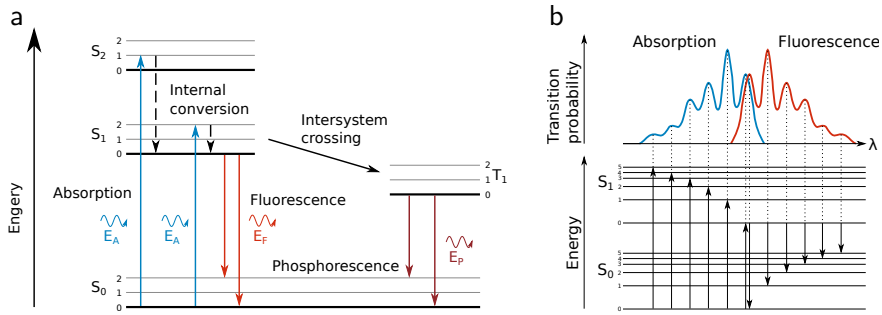


**Figure 2.1.:** Jablonski diagram and absorption and fluorescence spectra. (a) The electrons of the ground state $S_0$ absorb photons with the energy $E_A$ and get either to the excited state $S_1$ or $S_2$. Afterwards, they drop down to the vibrational ground-state due to internal conversion. The subsequent transition to the ground state under emission of a photon, where $E_F < E_A$, is called fluorescence. In case of phosphorescence, the electron first switches to $T_1$ before it relaxes to $S_0$ because of intersystem crossing [26, 30]. (b) Various transitions with their corresponding probability between different vibrational states lead to the typical shape of the absorption and fluorescence spectra [29]. Additionally, the spectra are broadened since the temperature is $T \gg 0$K. Otherwise the peaks would be narrower.

The typical shape of the absorbance and fluorescence spectra originates from transitions between various vibrational states (fig. 2.1b). According to the Franck-Condon principle, the probability for a change of the vibrational state can be calculated. Some changes are more compatible than others, because their wave functions are more alike. This leads to a higher transition probability, and therefore a greater impact on the spectra. Since the absorbance and fluorescence process between the same vibrational states involve the same wave functions, these spectra are mirrored [26, 29].

Fluorescent dyes are either synthesized chemically or genetically encoded. Although chemical dyes normally have the better properties for fluorescence microscopy such as photostability and brightness, they often lack the compatibility for live-cell imaging and specific binding. Other properties such as switching and blinking are principle functions which are required for several advanced fluorescence microscopy techniques. Biological fluorescent dyes such as the green fluorescent protein (GFP) are most suitable for live-cell imaging. Several GFP derivatives were developed recently to cover a wide range of the visible spectrum [31].

## 2.2. Conventional microscopy

### 2.2.1. Definitions of resolution limits

The resolution limit of an optical microscope was first described by Ernst Abbe in 1873 [2]. Here, a fine period grating was placed in the object plane of a transmitted microscope and illuminated with light. If the distance $d$ between the lines of the grating is too small, the spacing would not be visible in the image plane anymore. Taken this as the basis, Abbe defined the resolution limit of a microscope as

$$d = \frac{\lambda}{2n \sin \theta}, \tag{2.2}$$

where $\lambda$ is the wavelength of the used illumination light, $n$ is the refractive index of the medium between the object and the objective lens and $\theta$ is the half opening angle of the objective lens. Thus, $d$ is the minimum distance between two objects that can be still resolved by the microscope.

However, since individual fluorescent dyes are single point emitters, the Abbe criterion can also be seen from a different aspect. Point emitters are detected as Airy disc if they are situated in the focus of the imaging system and observed through a circular aperture with limited size. The corresponding two dimensional description is the so-called point spread function (PSF). Here, the Abbe criterion

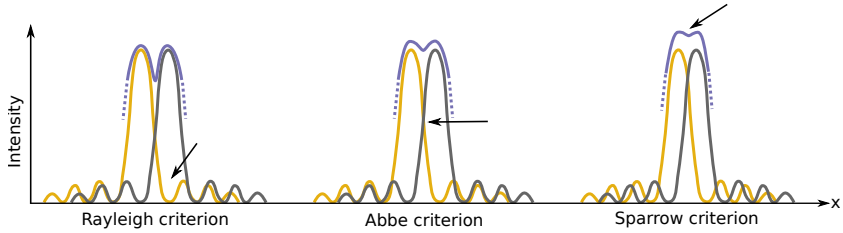


**Figure 2.2.:** Definitions of resolution limits. Schemes of the most prominent resolution criteria, where the sum (purple) of the two point emitters (yellow and gray PSF) still display a dip. According to the Rayleigh criterion the main maximum of the gray PSF has to be at the first minimum of the yellow PSF. In case of the Abbe criterion, both PSF overlap at the half-width at half-maximum. The Sparrow criterion defines the point of the minimal distance where the dip between the PSFs is visible for the first time [32].

can be interpreted as the limit where the PSFs of two point emitters overlap at the half-width at the half-maximum [32] (fig. 2.2).

Other resolution limits are defined by the intensity distribution of the PSF $I_{\mathrm{PSF}}$ which can be described as

$$I_{\mathrm{PSF}} = I_0 \left[ \frac{2J_1\left(\frac{2\pi r}{\lambda}\sin\theta\right)}{\frac{2\pi r}{\lambda}\sin\theta} \right]^2 \tag{2.3}$$

where $I_0$ is the peak intensity, $J_1$ expresses the first kind Bessel function of the first order, and $r$ is the radius of the Airy disc. According to the Rayleigh criterion two point emitters are still distinguishable if the main peak of one emitter is at the same spot as the first minimum of the second emitter (fig. 2.2). Therefore, a calculation of the first minimum of eq. (2.3) leads to

$$d = \frac{0.61\lambda}{n\sin\theta}, \tag{2.4}$$

which was stated as the resolution limit by Rayleigh [27, 33, 34]. Nonetheless, the distance between the two point emitter can be decreased further. The minimal distance, where the sum of the PSFs still displays a dip, is determined by

$$d = \frac{0.47\lambda}{n\sin\theta}, \tag{2.5}$$

which is called the Sparrow limit (fig. 2.2) [35].

The resolution limit can also be expressed in Fourier space which is more usual and helpful for a couple of microscope techniques [36]. In general, the PSF is the blurred image of a point source observed by a microscope. Mathematically speaking, the emitted fluorescence results to an image $D$ which is the convolution $\otimes$ of the emission of the fluorescent sample $E$ with the microscopes PSF $H$ in real space:

$$D(x) = E(x) \otimes H(x) \tag{2.6}$$

A transformation to the Fourier space is more convenient because the convolution operator becomes a multiplication. Thus, eq. (2.6) results to

$$\tilde{D}(k) = \tilde{E}(k) \cdot \tilde{O}(k), \tag{2.7}$$

where $k$ is the corresponding frequency of $x$ in Fourier space and $O(k)$ the Fourier transform of the PSF, the so-called optical transfer function (OTF). The OTF of a microscope determines the frequencies which can be detected by the system. Higher frequencies beyond the cutoff spatial frequency $k_0$ cannot be resolved and the OTF can be seen as a low pass filter (see also fig. 2.9). Remarkable is, that $k_0 = 2n \sin\theta/\lambda$ is the corresponding frequency to the Abbe limit. Furthermore, the OTF decreases with higher frequencies which can be interpreted as a decrease in the transfer strength. Thus, higher frequencies are transmitted inferior to smaller frequencies in the optical system which leads to reduced contrast transmission [37, 38].

### 2.2.2. Resolution determination concepts

There are different approaches to experimentally determine the resolution of an optical system. Most concepts are suitable for various imaging techniques. However, the experimentally determined resolution depends highly on the imaging method because the data acquisition has a high impact on the image formation. Nevertheless, there are standard determination methods which are most suitable for optical microscopy [39].

#### Line profile measurement

According to the Sparrow limit, a very simple way to estimate the achieved resolution is a line profile measurement by applying an intensity plot over two individual structures, like single dyes or filaments in cells. If the distance between the structures is below the achievable resolution, there will be no dip in the intensity plot.

Otherwise, if there is a dip, the maximum intensity of each structure can be identified. The corresponding distance between the maxima is stated as the achieved resolution [35, 40].

### Gaussian fit

The main peak of a detected PSF of a single point emitter is approximately a Gaussian function [41]. By fitting a two dimensional (2D) Gaussian to the intensity profile, the full width at half maximum (FWHM) can be determined [42, 43]. Here, the FWHM is considered as the resolution power of the optical system. Moreover, the 2D Gaussian fit can also be applied to estimate the central position of a single dye. Now, analogous to the line profile measurement, the intensity plots of two close dyes are fitted and the distance between their peak positions is considered as the achieved resolution [44]. However, this method neglects the dipole orientation of the fluorescent sample which results in a misleading resolution. Therefore, suitable dyes and objectives should be used to minimize this effect [45].

### FRC analysis

Fourier ring correlation (FRC) is one of the newest resolution determination concepts. Basically, FRC takes the whole detected image into account and estimates the highest resolvable frequency [39].

The workflow used for the determination of the resolution starts with splitting the original data set into two subimages (fig. 2.3). These subimages must show the same structure, but feature different, independent noise realizations. This can be done by recording two data sets of the same region-of-interest in series. Some microscopy methods, typically SMLM, require subsequent image reconstruction of thousands of single frames. Here, the first half of the data set and then the second half of the data set needs to be reconstructed to obtain the two independent data sets. To evaluate the resolution of imaging methods such as SOFI via FRC, a more complex blocking scheme is required (see appendix A.1.2). Now, both sets are transferred to Fourier space and then multiplied to obtain the correlated image. For the FRC, the Fourier transformed image is then divided into bins which are concentric rings of increasing radius centered around the origin of the spatial frequency coordinate system. To get the characteristic FRC curve, a correlation value for each bin is calculated and summed up to

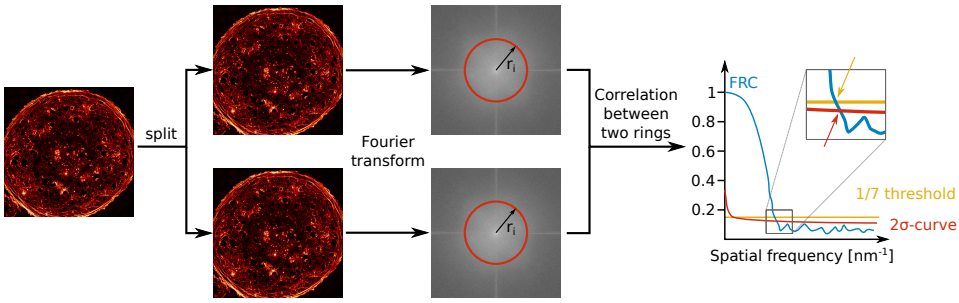


**Figure 2.3.:** Principle of FRC calculation. First, the image is split into two subimages, which consist of half the data set. These images represent the same structure, but feature different, independent noise realizations. Both subimages are then Fourier transformed and a correlation between bins of radius $r_i$ is determined and the FRC curve is the summed up correlation values of the bin. The calculated resolution is the frequency where either the 1/7 threshold (yellow arrow) [46] or the $2\sigma$ curve (red arrow) [47] crosses the FRC curve.

$$FRC\left(r_i\right) = \frac{\sum_{r\in r_i} \tilde{f}_1\left(r\right) \cdot \tilde{f}_2\left(r\right)^*}{\sqrt{\sum_{r\in r_i} \left|\tilde{f}_1\left(r\right)\right|^2 \cdot \sum_{r\in r_i} \left|\tilde{f}_2\left(r\right)\right|^2}} \tag{2.8}$$

Here, $\tilde{f}_1\left(r\right)$ and $\tilde{f}_2\left(r\right)$ are the Fourier transforms of the two subimages and $r_i$ the $i$th frequency bin [39, 46, 47].

There are two definitions for the achieved resolution estimation of the $FRC\left(r_i\right)$ calculation. On the one hand, a $2\sigma$ curve

$$F_{2\sigma}\left(r_i\right) \frac{2}{\sqrt{N_P\left(r_i\right)/2}} \tag{2.9}$$

with $N_P\left(r_i\right)$ as the number of pixels in the ring $r_i$, and its crossing with eq. (2.8) is calculated (fig. 2.3, red curve). This spot was found as the first crossing level point with negative slope of the difference curve. The corresponding frequency at this crossing is then quoted as the resolution [47]. On the other hand, a fixed threshold equal to 1/7 can be set to get the corresponding resolution distance (fig. 2.3, yellow curve) [46]. Several open-source plugins for ImageJ [48, 49] exist to calculate the FRC, which makes it a convenient tool for many users [50, 51].

### 2.2.3. Wide-field microscopy

A standard fluorescence microscope is realized in the wide-field configuration. The main components are an excitation source, an objective and a camera. Other optics like lenses and mirrors are utilized for a proper beam shaping and adjustment of the beam path [52].

#### Excitation and detection path

The beam path of a fluorescence microscope starts with the excitation source (fig. 2.4a). Often a laser is used if coherent and monochromatic light is required. Otherwise, a light-emitting diode (LED) can be utilized which has been proven to be sufficient enough for a couple of applications [19, 53, 54]. At the microscope, the laser beam is focused into the back-focal plane of the objective. High-end fluorescence microscopes utilize immersion oil objectives to achieve the best resolution because such objectives have a high numerical aperture (NA). The NA is directly related to

$$\mathrm{NA} = n \sin \theta, \tag{2.10}$$

and thus determines the resolution (compare to eq. (2.2)). Nevertheless, the effective NA of the system can be reduced to some extent by the refractive index of the sample itself. Therefore, suitable embedding media with a certain refractive index are required to match with the NA. Note, that for live-cell imaging the cells are often embedded in water, which results in a lower effective NA due to the low refractive index of water.

For the detection, the same objective is used to collect the emission light of the sample. Due to the Stokes shift the fluorescence signal is red-shifted, so that a dichroic mirror can split the signal from the excitation laser. Here, the laser beam is typically reflected and the emission transmitted of the dichroic mirror. However, to suppress or even block unwanted signals in the detection path a dichroic mirror is not sufficient enough and additional emission filters are placed in front of the camera. The filtered fluorescence is then collected and focused on the camera chip with a tube lens [51, 55].

#### Illumination schemes

The most used configuration to excite a fluorescent sample is the Epi illumination (fig. 2.4b). Here, the laser beam path enters at the center of the objective

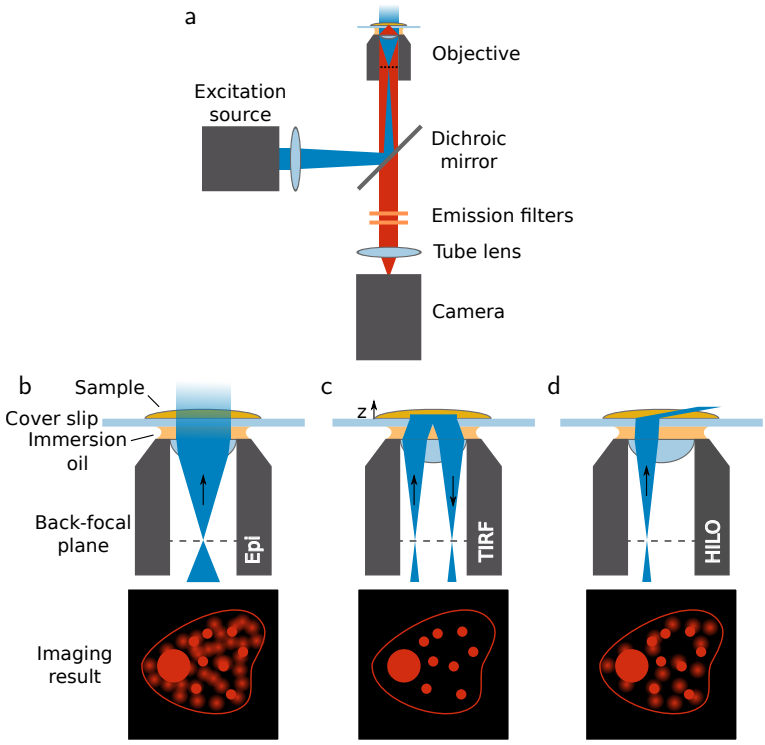


**Figure 2.4.:** Scheme of a typical wide-field fluorescence microscope and sketches of different excitation concepts with their resulting detected image. (a) A laser (blue) is normally used as a coherent excitation source, which is then focused into the back-focal plane of the objective. The same objective is utilized to collect the fluorescence emission (red) from the sample. A dichroic mirror splits the excitation light from the fluorescence signal. Emission filters are used to block unwanted signals. With a tube lens the emission is focused on the camera where the image is formed. (b) In Epi illumination a collimated beam is used and the whole sample is excited. (c) In TIRF illumination the incoming beam is shifted towards the edge of the objective, so that total internal reflection at the cover slip occurs. Only fluorescent dyes in close proximity to the glass surface are excited, and therefore imaged. (d) In HILO configuration a small light sheet is generated by shifting the incoming beam to a proper position [51, 56, 57].

and is then collimated. Therefore, the whole sample along the optical axis is illuminated. Fluorescence emission of out-of-focus will be detected, which leads to a worse signal-to-noise ratio and subsequent loss in the imaging contrast. Additionally, the unwanted excitation of out of focus dyes results in photobleaching in regions which are not supposed to be imaged [51].

Total internal reflection fluorescence (TIRF) microscopy has been developed to circumvent unwanted excitement and to only illuminate the sample at the surface of the cover glass (fig. 2.4c). Here, the laser beam is shifted from the center of the objective to the edge of the opening. For TIRF, the laser beam has to be totally reflected at the cover glass which is achieved by setting up the excitation angle to the critical angle $\theta_c$,

$$\theta_c = \arcsin\left(\frac{n_2}{n_1}\right), \tag{2.11}$$

where $n_1$ is the refractive index of the coverslip and $n_2$ the refractive index of the sample or the used embedded medium. Now, an evanescent field is generated at the surface of the sample with a penetration depth of a few hundred nanometers. Thus, only a small sheet is illuminated and almost no fluorescent dyes are excited outside of the focal plane [58].

The small excitation volume of TIRF is useful for many application, but is insufficient if a larger volume or imaging of structures not in close proximity to the cover glass is required. A compromise between Epi and TIRF illumination is HILO (highly inclined and laminated optical sheet, fig. 2.4d). By shifting the illumination beam back in the direction to the center of the objective, a light sheet will be generated in the sample. Thus, a better signal-to-noise ratio compared to Epi illumination is accomplished and dyes inside the sample, not only the surface, can be detected [57].

### Camera detectors

The image recording process needs to be adapted to the microscopy technique. For wide-field imaging typically a camera is used as a detector, by projecting the image of a certain sample area directly on the chip. The chip consists of a 2D array of pixels which collects the photons of the fluorescence signal. These photons are then converted into an electric charge via the photoelectric effect. The intensity of the fluorescence signal in each pixel is thus directly proportional to the number of collected electrons. The most common architectures for those chips are CCD

(charged-coupled device) and CMOS (complementary metal-oxide semiconductor) detectors [51, 59].

**CCD** Typically each pixel is arranged in three registers. To read out the charge of each pixel at the end of the exposure time, the charge of a line is first transferred from the light sensitive register to its neighbor in a shielded region, which is not light sensitive. Next, the charge is shifted to the last register where it is converted from analog to digital signal. Since this process is repeated for each row, the sensor is read-out line-wise [60, 61].

The so-called emCCD (electron multiplying charged coupled device) sensors have an additional register, in comparison to normal CCD chips, to further amplify the stored charge. Here, the originally detected signal is multiplied by a high-voltage, and therefore even single photons can be detected. Nevertheless, the noise introduced by the analog-to-digital converter step is also amplified which leads to excess noise [62].

(em)CCD image sensors are most suitable for imaging at very low photon signal levels (one to five photons) due to their low spatial noise and low dark current. Furthermore, they have a high linearity and an excellent image quality. However, due to the line-wise read-out process the frame rate is low, which makes the sensor insufficient for imaging fast dynamics [63].

**CMOS** In contrast to CCD image sensors, each pixel is read out and amplified individually in a CMOS sensor which leads to potentially higher frame rates. In detail, these pixels are *active pixel sensors* consisting of a photodiode and three transistors. At the beginning of the exposure, the voltage at the photodiode is reset via the first transistor. The incoming light changes the capacity of the photodiode proportional to time and intensity by generating electrons due to the photoelectric effect. After the exposure time, a second transistor is turned on to connect the third amplifier transistor with a column bus to transfer the voltage to an analog-to-digital converter. This signal is then readout for every pixel in order to produce an image [60].

Additionally, processing directly on the chip is possible and the chip is typically larger than a CCD chip, so that a bigger field of view can be imaged. Nonetheless, the simultaneous read-out causes larger spatial inhomogeneity over the chip and higher dark current. Scientific CMOS sensors (sCMOS) are specifically designed and calibrated to alleviate these effects, so that the advantages for CMOS chips can be used in a setting where precise, quantitative imaging is required [63, 64].

**Nyquist-Shannon criterion** To avoid undersampling of the camera chip, the Nyquist-Shannon criterion has to be considered. According to this theorem, the sampling has to be at least twice the resolution $d$ (compare eq. (2.2)). Therefore, the projected pixel width $a$ should be at most one half of $d$. Additionally, the squared structure of the pixels has be to weighed which leads in total to

$$a = \frac{d}{2\sqrt{2}} \tag{2.12}$$

An adjustment to this optimal projected pixel size is done by implementing a suitable tube lens in front of the camera [51, 65, 66].

### 2.2.4. Deconvolution methods

As already described in section 2.2.1, the image formation is a convolution of the sample emission and the PSF of the microscope (compare eq. (2.6)). With computational *deconvolution* methods the process of convolution can be reversed to a certain point and a high-resolution image with an improved contrast can be obtained (fig. 2.5) [67]. Several applications in biology and medicine [3, 68], and even in astronomy [69], benefit from this method since it is straightforward to perform.

The causes of image degradation in an optical microscope can be classified in four independent groups, namely *noise*, *scatter*, *glare*, and *blur*. Scatter and glare are random disturbances of light due to the refractive index of the specimen and the optics of the microscope. Therefore, there is no complete prediction or mathematical modeling. Noise is also a random component, but its distribution can be mathematically modeled as a signal-dependent Poisson distribution which is termed as shot noise. Due to the discrete nature of photon detection, a sensor can only collect a discrete number of photons $N$. The signal follows a Poisson distribution whereas the uncertainty scales with $\sqrt{N}$ [51, 55]. The imaging sensor itself additionally introduces low Gaussian distributed noise which arises in amplifiers and detectors due to thermal vibrations of atoms and the discrete nature of radiation in warm objects [70]. Noise can be reduced by suitable filters which is done in some deconvolution methods.

Since higher spatial frequencies are attenuated by the imaging system, the resulting image is blurred. The process of deconvolution itself mainly aims to remove or reverse the blur [67]. The main approaches to deconvolute an image can be grouped in two parts: *deblurring* and *restoration* algorithms [71].

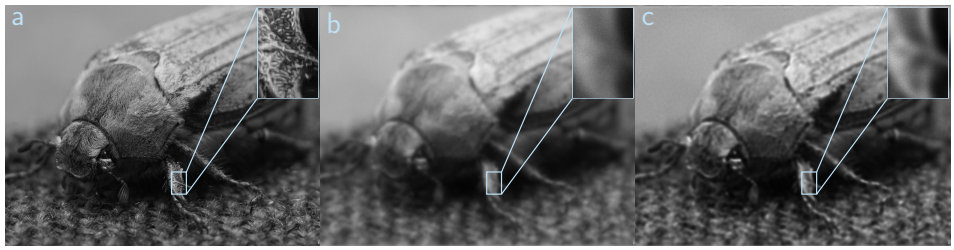


**Figure 2.5.:** Demonstration of deconvolution. (a) Ground truth image of the object/sample cockchafer. (b) Simulated image representing a microscopy recording. The ground truth has been convoluted with a simulated PSF (fig. 2.6) and Gaussian and Poisson noise has been added to provide realistic imaging conditions. (c) Deconvoluted image of (b) by applying the Richardson-Lucy algorithm (20 iterations). The contrast enhancement is clearly visible while the resolution cannot be increased compared to the simulated image.

### Deblurring process

Biological samples, such as cells and tissue, usually have an intrinsic thickness of a few micrometer. Therefore, fluorescence signal will additionally be detected from the out-of-focus region. Deblurring methods, also called "nearest-neighbor" algorithm, consider this unwanted signal and remove it from the in-focus plane [67, 71].

Here, each section slice $n$ of a three dimensional image stack is treated as a sum of the $n+1$ and $n-1$ slice of the stack. Thus, with eq. (2.6), the image plane $D_n$ can be expressed as

$$D_n = E_n \otimes H_n + E_{n+1} \otimes H_{n+1} + E_{n-1} \otimes H_{n-1}, \tag{2.13}$$

where $E$ denotes the sample emission and $H$ the PSF of the microscope. Although only the fluorescence signal of the nearest slices is taken into account, this is a good approximation [71]. Now, the original images $D_{n+1}$ and $D_{n-1}$ are blurred by digital blurring filters according to their respective PSF to generate an approximation of the $E_{n\pm1} \otimes H_{n\pm1}$ terms since $E_{n\pm1}$ is unknown. Thus, eq. (2.13) is modified to

$$D_n = E_n \otimes H_n + D_{n+1} \otimes H_{n+1} + D_{n-1} \otimes H_{n-1}, \tag{2.14}$$

so that it is basically still the addition of the blur of the lower and above slice to the slice $D_n$. As the final step, the estimated blur $D_{n\pm1} \otimes H_{n\pm1}$ is subtracted from the original image $D_n$ which results in an improved contrast [67, 71].

This method is computationally economical due to the rapid and relatively simple calculations. However, this algorithm is improper for quantitative analysis because it introduces artificial changes in the intensities of the pixels. Additionally, all structures in the image, whether real objects or noise, will be enhanced which results in a worse signal-to-noise ratio and might introduce structural artifacts. Nevertheless, the deblurring process is suitable for a first attempt if a quick contrast enhancement is needed and the computational power is limited [67, 71].

### Restoration algorithms

In contrast to the deblurring process, restoration algorithms differ in two major points. On the one hand, these calculations take eq. (2.7) into account, and on the other hand, the method considers the noise. The main structure of these kind of algorithms is mostly an iterative process. As the first step $n$ the sample emission $E^{(n)}$ is guessed, and then convoluted with the PSF to get a predicted image $D^{(n)}$. Usually, the original data is used for $E^{(n)}$. Now, the assumed $D^{(n)}$ is compared to the original data. The information gained from the comparison is used to make a new approximation for $E^{(n+1)}$. The exact update to a new $E^{(n+1)}$ is the major difference between various restoration algorithms [71, 72].

**PSF estimation** For all algorithms a PSF (or OTF in Fourier space) is required, which can be either measured or estimated. To measure the PSF of a microscope, a 3D stack of a fluorescent point source is imaged. However, an estimated PSF is sufficient for most applications [67].

Various PSF models exist and one of the most common is the Born-Wolf model [74]. It describes the scalar-based diffraction that occurs in the microscope when the particle is in focus. In case a wide-field microscope is used for imaging, the model in real space $H(x, y, z)$ is defined as

$$H(x,y,z) = \left| C \int_0^1 J_0 \left[ k \frac{NA}{n_i} \sqrt{x^2+y^2}\rho \right] \exp\left( -\frac{1}{2} i k \rho^2 z \left( \frac{NA}{n_i} \right)^2 \right) \rho d\rho \right|^2 \quad (2.15)$$

where $C$ is a normalization constant, $\rho$ is the distance of the point source to a certain point in space, $J_0$ is the Bessel function of the first kind of order zero and the wave number $k = 2\pi/\lambda$ of the emitted light. All the other parameters like the

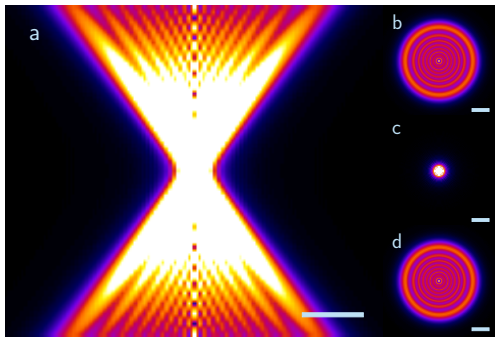


**Figure 2.6.:** Idealized 3D PSF according to the Born-Wolf model. The PSF was simulated with [73] by setting the emission wavelength $\lambda = 610\,\text{nm}$, the refractive index of the oil $n_i = 1.5$, the objective $NA = 1.4$ and the $z$-stepsize to 250 nm. (a) $xz$ view of the PSF with the typical hourglass shape, symmetrical in both directions. $xy$ view of the PSF above the focus point (b), at the focus (c) and lower the focus (d), with the Airy disc pattern. Scale bar $3\,\mu\text{m}$ (for all images).

wavelength $\lambda$ of the emitted light, the numerical aperture of the objective NA, and $n_i$ the refractive index of the immersion layer, are individual for each experiment [73]. With the Born and Wolf model a perfect 3D PSF can be generated (fig. 2.6). The concentric rings above and under the focus, and the typical shape along the optical axis, are clearly visible [73]. A generalized version of this approximation is the Gibson and Lanni model. Here, the refractive index mismatch between the immersion oil, the cover-slip and the sample layers is taken into account [75].

Coming back to the restoration algorithms, the generated PSF is crucial for the following methods, which are the most common approaches to obtain a deconvoluted image.

**Wiener filtering** This method is one of the most simple ways to deconvolve a recorded image. Basically, the deconvoluted image is estimated from an updated version of eq. (2.7) because the noise needs to be considered. For this, eq. (2.6) is rewritten to

$$D(x) = E(x) \otimes H(x) + n \tag{2.16}$$

with $n$ as the additive noise component. Now, eq. (2.16) can be used to determine

a deconvoluted image by

$$E(k) = \frac{D(k)}{O(k)} - \frac{n}{O(k)} \tag{2.17}$$

However, according to eq. (2.17) noise in the detected image is a serious problem if the OTF is very small or even zero at that point. To circumvent this issue, high frequencies, which primarily contain noise due to the spatial frequency attenuation of the OTF, are suppressed. Unfortunately, the sharpness of the image is also reduced by this suppression. Nonetheless, if the signal-to-noise ratio of the recorded image is high, less high frequencies needs to be eliminated, and therefore the Wiener filter can be a good method to deconvolve an image [72, 76, 77].

**Richardson-Lucy algorithm** The Richardson-Lucy process is a maximum likelihood approach, where the noise is considered to be Poisson distributed [78, 79]. This algorithm follows an iterative process where the difference between the deconvoluted image and the real image is supposed to be minimized. The model for the noise is valuable if the fluorescence signal is weak and the noise is a significant component in the image. Additionally, this method exhibits the strength to recover certain information (fig. 2.5) [72, 76].

## 2.3. Super-resolution microscopy

In the year 2014 the Nobel Prize in Chemistry has been awarded for breaking the diffraction limit defined by Abbe with optical fluorescence microscopy. Such microscopy methods are referred to super-resolution microscopy (or technique). Optical nanoscopy is also a common term, since a resolution down to a few nanometers can be achieved [1, 6].

The path to optical nanoscopy has begun with the first successful observation of a single fluorescent dye by Moerner et al. [80]. The first theoretical concept to break the diffraction limit by Abbe was reported by Hell et al. [7, 81] and experimentally realized a couple of years later [82]. The observation by Moerner, the approach by Hell and the concept for super-resolution imaging by Betzig et al. [8] were awarded with the Nobel Prize.

Since then, several nanoscopy techniques have been developed and further improvement is still ongoing [15]. The key for all super-resolution methods is to narrow the shape of the PSF because this results in a wider OTF, and therefore higher frequencies can be transmitted through the microscope [1, 15, 83]. However,

each super-resolution method has its own limitations concerning speed, resolution enhancement and live-cell compatibility [83, 84]. Thus, the nanoscopy technique needs to be chosen according to the application [1]. In this section, the most prominent super-resolution techniques are introduced and those which are used for this thesis are described in more details.

### 2.3.1. Stimulated emission depletion microscopy

In contrast to conventional wide-field microscopy, the stimulated emission depletion microscope (STED) utilizes a point scanner and photon detector like a photodiode to image the sample. This concept is an extension of a standard *confocal microscope* [30]. Like in conventional microscopy a laser is used to excite the fluorescent dyes. A second, red-shifted laser, the so-called STED beam, overlays the first one. The doughnut-shaped STED beam has one local minimum in the center to deplete fluorescence emission apart from the center intensity minimum. Therefore, the scanning spot and the effective PSF are narrowed to sub-diffraction scales and a super-resolved image can be obtained [7, 82]. Similar to STED, the RESOLFT approach (reversible saturable/switchable optical linear fluorescence transitions) achieves such a fluorescence inhibition by employing reversibly photoswitchable fluorescent dyes [85].

With high-end scientific STED microscopes a resolution down to 30 nm - 80 nm can be achieved, whereas commercially available systems reach a resolution of 60 nm - 120 nm [1]. However, the resolution $d$ can be determined and adjusted by

$$d \approx \frac{\lambda}{2NA\sqrt{1 + \frac{I}{I_{\text{sat}}}}} \tag{2.18}$$

with $I$ the maximal focal intensity applied for STED and $I_{\text{sat}}$ as a characteristic value at which the fluorescence signal probability is reduced to $\frac{1}{e}$ [86]. By increasing the laser power a better resolution can be achieved, which, on the other hand, leads to higher phototoxicity, and therefore is less live-cell compatible [87]. On artificial samples optimized for high $I_{\text{sat}}$ intensities, resolutions down to 30 nm have been demonstrated on biological samples [88] and down to 2.4 nm in imaging nitrogen vacancies in diamonds [89].

Nevertheless, STED has been proven a powerful tool when it comes to image biological and medical samples. Starting from the very first applications [82, 86], various research studies utilize STED to image for instance cancer tissue [90], dynamics and structures in neurons [91, 92], or to analyze proteins in mice [93].

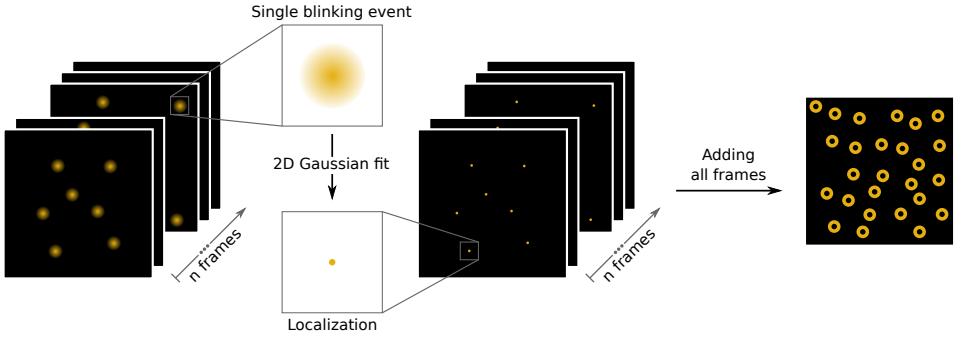


**Figure 2.7.:** Basic principle of SMLM. A wide-field image stack of $n$ frames will be recorded with $n$ typically greater than ten thousand. The blinking events of each single frame are fitted by a 2D Gaussian function to estimate the center, and therefore the localization position. By rendering all localization, a super-resolved image can be obtained. Here, a ring-shaped structure becomes visible which would have been a filled spherical object in conventional wide-field microscopy.

Additionally, STED can be combined with other techniques such as fluorescence correlation spectroscopy (FCS) [94, 95] or fluorescence recovery after photobleaching (FRAP) [96].

### 2.3.2. Single molecule localization microscopy

In single molecule localization microscopy (SMLM) the basic principle of molecule *blinking* is employed [43]. Mainly, the fluorescent molecule needs to switch, meaning it transitives from an on-state to an off-state and backwards [97]. Therefore, not all emitters send a fluorescent signal at the same time and single blinking events can be separated. SMLM experiments are mostly carried out on a conventional wide-field setup, so that the intensity distribution of a single emitter can be fitted by a 2D Gaussian function whose center is defined as the localization position of the molecule [41]. Several thousands of frames are recorded and each single blinking event is fitted. By combining all the localization positions in a single image by computational reconstruction, a super-resolved image with a resolution of down to a few tens of nanometers can be achieved (fig. 2.7) [43].

The switching can be induced by photoactivation, which is a stochastic process. The most prominent methods are PALM (photoactivation localization microscopy

[8, 98]) and STORM (stochastic optical reconstruction microscopy [9]) where the rapid switching of lasers is used for the blinking process of the molecules. A modification of the imaging buffer can manage to induce an intrinsic switching of the fluorescent dyes. Thus, turning the laser source on and off is unnecessary since the molecules are intrinsically in the blinking regime (dSTROM - direct STORM [10, 99]). Another approach is PAINT (points accumulation for imaging in nanoscale topography [11, 100]) where the blinking is introduced by binding kinetics of the fluorescent molecule to the target structures. By attaching to the target structure the dye is turned on and otherwise there is no fluorescent signal.

The localization precision $\sigma_x$, and therefore also indirectly the achieved resolution, depends on the number of detected photons $N$,

$$\sigma_x \approx \frac{s}{\sqrt{N}} \tag{2.19}$$

with $s$ as the standard deviation of the Gaussian fit [43]. If more photons are measured, the localization precision is higher and parameters such as background noise have an impact on $\sigma_x$. To reconstruct a SMLM image and to estimate $\sigma_x$, several software packages are available [101–103] with their own set of options and drawbacks [104]. SMLM is also possible in 3D [105] or dual color [106], and there is an ongoing progress of the software packages and algorithms.

The biggest advantages of SMLM is the high spatial resolution, which however comes at the cost of the temporal resolution. The sample needs to be fixed in most cases for the imaging process due to the long acquisition time. Several biological and medical specimens were studied such as nuclear core complexes [107, 108], the inner structure of actin filaments in neurons and dendrites [109], synapses in the brain [110], and protein complexes in mitochondria [111].

### 2.3.3. Super-resolution optical fluctuation imaging

Like SMLM techniques, super-resolution optical fluctuation imaging (SOFI) relies on the stochastical intensity variation of the fluorescence signal. However, a different, correlation based reconstruction approach is used, and therefore a much higher label density is still sufficient. Further, in comparison to SMLM less recorded frames are needed since several nearby emitters can be active. SOFI also requires less photons, which makes it well suitable for fluorescent proteins. By analyzing the correlation of the time trace of the intensity fluctuation of each pixel, a super-resolved image can be computationally reconstructed with significant contrast enhancement (fig. 2.8) [12, 112].

### Correlation and cumulant analysis of signal fluctuations

Like SMLM, SOFI can be utilized on any microscope setup which provides a time-lapse acquisition mode [113]. Nevertheless, three conditions must be met for a proper correlation analysis [12]:

1. Each emitter needs to have at least two different emissive states such as an on- and off-state.
2. The blinking has to be stochastic and one emitter must not affect the other one in its blinking behavior.
3. The projected pixel size must be smaller than the PSF size.

For the exact reconstruction of the SOFI image, the underlying theory is mainly the calculation of correlations and cumulants of each pixel, whereas photobleaching is detrimental. First, the fluorescence source distribution, essentially the ground truth (compare eq. (2.6)), is modeled by

$$\sum_{k=1}^{N} \delta\left(\vec{r} - \vec{r}_k\right) \cdot \epsilon_k \cdot s_k\left(t\right) \tag{2.20}$$

with $k$ as the counting variable for each emitter, $N$ as the total number of emitters and where $\vec{r}_k$ is the position of each emitter. $\epsilon_k$ is the constant molecular brightness and $s_k\left(t\right)$ is the time-dependent fluctuation and their product $\epsilon_k \cdot s_k\left(t\right)$ can be seen as the time-dependent molecular brightness [12]. Since the measured fluorescent image is a convolution of the sample distribution eq. (2.20) and the PSF $H\left(\vec{r}\right)$, the fluorescence signal $F\left(\vec{r}, t\right)$ at the position $\vec{r}$ and time point $t$ is given by

$$F\left(\vec{r}, t\right) = \sum_{k=1}^{N} H\left(\vec{r} - \vec{r}_k\right) \cdot \epsilon_k \cdot s_k\left(t\right), \tag{2.21}$$

where a few assumptions were made. On one side, the sample is assumed to be in a stationary equilibrium during the acquisition, and therefore only the blinking leads to temporal change. On the other side, the PSF does not vary locally. The fluctuation in the fluorescence signal $\delta F\left(\vec{r}, t\right)$ is defined as the difference to the original signal $F\left(\vec{r}, t\right)$ and the signal's time average $\left\langle F\left(\vec{r}, t\right)\right\rangle_t$ which results to

$$\delta F\left(\vec{r}, t\right) = \sum_{k=1}^{N} H\left(\vec{r} - \vec{r}_k\right) \cdot \epsilon_k \cdot \delta s_k\left(t\right) \tag{2.22}$$

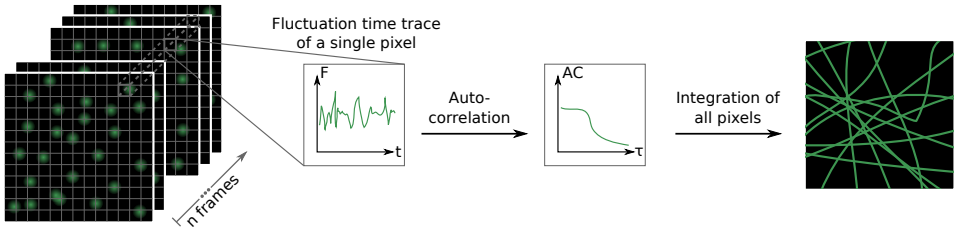


**Figure 2.8.:** Basic principle of SOFI. Several hundred frames of stochastically blinking emitters are recorded. For each pixel the fluctuation of the fluorescence signal $\delta F(\vec{r}, t)$ is determined and analyzed via auto-correlation $AC$ or cumulant calculation for high-order correlations. The $AC$ function of each pixel is reassigned to a pixel value. Highly correlated fluorescent signal such as blinking fluorescent dyes will have a greater correlation value than uncorrelated noise. Therefore, the resulting image has a significant background reduction and additionally super-resolution quality is obtained [12].

by considering eq. (2.21). The mean value of eq. (2.22) would result to zero due to signal values lower and higher than the average. Now there is an expression for the fluctuation for each pixel. In case the fluctuation originates from an emitter, the signal is highly correlated to itself. Intensity variations like noise are not correlated at all. Thus, an analysis of the correlation of the fluctuation results in background reduction and an increased resolution (fig. 2.8) [12].

For simplicity, the autocorrelation function of the second-order $G_2(\vec{r}, \tau_1, \tau_2)$ with the lag time $\tau$ will be determined first. Thus, a pixel $i$ of the frame $m$ will only be correlated with the same pixel $i$ of the subsequent frame $m+1$. Nevertheless, $G_2(\vec{r}, \tau_1, \tau_2)$ can be reduced to $G_2(\vec{r}, \tau)$, because $\delta F(\vec{r}, t)$ was assumed to be a zero-mean stationary random process, which is valid for all $n^{\text{th}}$ order correlations. Therefore, the $n^{\text{th}}$ order correlation function is only a function of the $n-1$ lag times $\tau_1, ..., \tau_{n-1}$ [114]. For the calculation of $G_2(\vec{r}, \tau)$, it is additionally assumed that all cross-correlation terms vanish since the emission of different fluorescent dyes does not correlate. Thus, one gets

$$\begin{aligned} G_2(\vec{r}, \tau) &= \langle \delta F(\vec{r}, t+\tau) \cdot \delta F(\vec{r}, t) \rangle_t \\ &= \sum_k H^2(\vec{r} - \vec{r}_k) \cdot \epsilon_k^2 \cdot \langle \delta s_k(t+\tau)\, s_k(t) \rangle \end{aligned} \tag{2.23}$$

which appears to be a simple sum of the squared PSF $H$, multiplied by each

emitter's squared brightness and molecular correlation function [12]. Therefore, a SOFI image is obtained by brightness and its degree of correlation. Due to the squared $H$ resulting in narrowing the PSF shape, the resolution is improved by the factor $\sqrt{2}$ which can be generalized to a resolution enhancement of $\sqrt{n}$ for a $n^{\text{th}}$ order correlation function [12, 113].

Although the calculation of correlation functions is convenient, it has its limitations when it comes to higher-order correlations. Now, cumulants are introduced which are quantities related to correlation functions and also originate from probability theory and statistics. Higher-order cumulants are needed because they do not contain cross-terms of lower-order correlations. For example, if the fourth-order correlation is determined, four photons in one pixel need to be correlated. These might originate from the same emitter, but it is also possible that two photons were emitted from two independent fluorescent dyes. If autocorrelation would be utilized, these two-photon cross-terms also contribute to the fourth-order correlation with the resolution enhancement of second-order correlation. By applying cumulants these cross-terms are eliminated and only highly correlated fluctuations are left [12].

The simplest way to calculate cumulants are auto-cumulants $AC$ which are equivalent to autocorrelation functions. However, second- and third-order cumulants are identical to their second- and third-order correlation counterparts, and thus the earlier calculations are still valid [113]. The generalized form to determine a $n^{\text{th}}$-order auto-cumulant is given by

$$AC_n\left(\tau_1, ..., \tau_n\right) = \sum_k H^n\left(\vec{r} - \vec{r}_k\right) \cdot \epsilon_k^n \cdot w_k\left(\tau_1, ..., \tau_n\right) \tag{2.24}$$

where $w_k\left(\tau_1, ..., \tau_n\right)$ is a correlation-based weighted function depending on the specific fluctuation properties [12, 112]. Note that a non-fluctuating emitter over time yields to no correlation, and thus its weighting contribution $w_k\left(\tau_1, ..., \tau_n\right)$ will be zero. Otherwise, blinking emitters correlate over time and contribute to the auto-cumulant and the exact value is determined by the specific switching behavior from the on- to off-state [12].

By applying cross-cumulants $CC$, additional virtual pixels are introduced resulting in a finer grid, and therefore the resolution enhancement of higher-order cumulants can be fully exploit [112, 113, 115]. Otherwise, the resolution improvement of higher-orders cumulants would yield to values which could not be represented by the projected pixel size. Cross-cumulants also take the neighboring pixels into account. In general, cross-cumulants can be determined by

$$CC_n\left(\vec{r}_1,...,\vec{r}_n,\tau_1,...,\tau_n\right) = \prod_{j<l}^{n} H\left(\frac{\vec{r}_j - \vec{r}_l}{\sqrt{n}}\right) \cdot \sum_{k=1}^{N} H^N\left(\vec{r}_k - \frac{\sum_i^n \vec{r}_i}{n}\right) \cdot \epsilon_k^n \cdot w_k\left(\tau_1,...,\tau_n\right) \tag{2.25}$$

where $i$, $j$ and $l$ are indices for the nearby contributing pixels and $k$ is the index of the current position. According to eq. (2.25) the cross-correlation pixel is weighted by a PSF-shaped weight factor which depends on the distance of the pixels, and thus virtual pixels can be created. The subsequent grid size growths by a factor of $n^2$ in accordance to the $n^{\text{th}}$-order cross-cumulant [112, 113]. However, when applying the zero time lag $\tau = 0$, even the shot noise and the camera read-out noise can be eliminated [112]. A nice byproduct from the cross-cumulant calculation, due the PSF-shaped distance factor, is an estimated PSF which scales like the original optical PSF. Therefore, Fourier reweighting on either $n^{\text{th}}$-order auto- and cross-cumulants can be utilized which results in a resolution improvement of a factor of $n$ [112, 113, 115].

#### Further development and applications

Several developments concerning the underlying theory of SOFI and the improvement of software packages were progressed in the recent years [116, 117]. For instance, since SOFI respond non-linear to brightness and blinking heterogeneities in the sample, further progress concerning this issue was made. Here, estimated blinking statistics are utilized to circumvent the non-linearity resulting in a balanced image contrast [118]. The effect of sample diffusion on SOFI accuracy [119] or the considering of photodestruction [120] were also investigated and yield to a more detailed model for SOFI. Moreover, with SOFI it is possible to unmix identical fluorescent dyes by their blinking kinetics, so that simultaneously two structures in living cells can be imaged [121].

Another key to obtain SOFI images of high quality is the switching rate and statistics of the used fluorescent dyes. Hence, specific dyes were created or tested in order to evaluate their practical function. Most common are switching fluorescent proteins such as Dronpa [122], but recent progress in this field generated various new suitable organic dyes [123, 124]. Naturally, fluorescent proteins are most compatible with fixed or live-cell imaging, but chemical dyes such as SERS (surface-enhanced Raman scattering) particles [113] for fixed samples, dual-color

nanodots [125] or even semiconducting polymer dots [126] verified their performance for SOFI.

Since the introduction of SOFI to the scientific community, it has proven its usefulness for many applications such as 3D imaging of tubulin structures [127] or live-cell multiplane imaging of mitochondria [128]. Furthermore, it is compatible with PALM studies which results in a spatial resolution less than 100 nm and a temporal resolution of approximately 10 s [129].

### 2.3.4. Structured illumination microscopy

Another essential class of super-resolution microscopy techniques is structured illumination microscopy (SIM) which employs an interference pattern in the sample to gain information about frequencies beyond the diffraction limit [1]. This method was first introduced by Heintzmann et al. [130], Gustafsson et al. [13] and a PhD thesis by Frohn [131], and ever since SIM has become a successful and established super-resolution microscopy method and its development is till ongoing [1, 38, 132]. SIM provides, in its most common linear implementation, doubled resolution compared to conventional wide-field microscopy, which results in a lateral resolution of about 100 nm and 300 nm to 400 nm in axial direction [1]. Methods such as SMLM and STED yield a better resolution improvement. SIM, however, is more applicable for live cell experiments, and provides higher temporal resolution, introduces less phototoxicity and is compatibility with lots of dyes [38].

In practice, the sample is illuminated with a fine-striped sinusoidal pattern which leads to mixing of high-frequency information. In the original approach [13, 130], the stripes have a single spatial frequency and are generated by two interfering laser beams. The interference pattern is then shifted to three equidistant phases and rotated by three angles (60° for each angle shift), resulting in a total number of nine raw image frames that have to be recorded. For three-dimensional SIM, an additional beam is utilized, which generates an axial pattern, and therefore also provides axial resolution improvement. Now, the phase has to be shifted five times, so that in total 15 frames needs to be recorded for 3D-SIM [14]. By applying a reconstruction algorithm, all frames can be merged to a super-resolved image [133]. To understand the mathematical principle of SIM and gain insight in the reconstruction algorithm, a short introduction is given in this section.

### Imaging reconstruction theory of SIM and reconstruction tools

For SIM, the image formation in real space, eq. (2.6), needs to be updated in order to consider the underlying sample structure [14, 134, 135]. Thus, eq. (2.6) can be now expressed by

$$D\left(\vec{r}\right) = \left[S\left(\vec{r}\right) \cdot I\left(\vec{r}\right)\right] \otimes H\left(\vec{r}\right) \tag{2.26}$$

where the emission is the product of the sample information $S\left(\vec{r}\right)$ and the illumination intensity $I\left(\vec{r}\right)$. The linear relation, where fluorophores are assumed to not blink, switch or saturate, is referred to as *linear SIM*. A multiplication in real space becomes a convolution in Fourier space and vice versa, so that $\tilde{D}(\vec{k}) = \left[\tilde{S}(\vec{k}) \otimes \tilde{I}(\vec{k})\right] \cdot \tilde{H}(\vec{k})$. A few conditions are satisfied that allow to simplify $\tilde{D}(\vec{k})$.

First, $I\left(\vec{r}\right)$ can be separated in a lateral $J_m\left(\vec{r}_{xy}\right)$ and axial part $I_m\left(z\right)$ and then summed over a finite number $m$

$$I\left(\vec{r}\right) = \sum_{m=0}^{M} I_m\left(z\right) \cdot J_m\left(\vec{r}_{xy}\right), \tag{2.27}$$

with $M$ as the number of harmonics in a periodic pattern $J_m(\vec{r}_{xy})$. The lateral pattern distribution $J_m\left(\vec{r}_{xy}\right)$ should be a sinusoidal wave, containing only a single spatial frequency $\vec{p}_m$,

$$J_m\left(\vec{r}_{xy}\right) = \cos\left(2\pi\vec{p}_m \cdot \vec{r}_{xy} + \phi_m\right) \tag{2.28}$$

with $\phi_m$ as the phase of the $m^{\text{th}}$ component. Furthermore, the nature of the illumination pattern leads to $\vec{p}_m = m\vec{p}$ and since the SIM pattern is symmetrical and rigid under translations between the images, the phase shifts also yield to $\phi_m = m\phi$ [134]. Thus, eq. (2.28) can be rewritten as

$$J_{m,n}\left(\vec{r}_{xy}\right) = \cos\left(m\left(2\pi\vec{p} \cdot \vec{r}_{xy} + \phi_n\right)\right) \tag{2.29}$$

where $\phi_n$ denotes the phase shift required for SIM.

For the last condition, the axial part of the illumination light distribution remains fixed in relation to the focal plane of the microscope objective. Therefore, $I_m\left(z\right)$ depends on the same coordinates as $H\left(\vec{r}\right)$ and not on the sample structure $S\left(\vec{r}\right)$, so that only a multiplication of the axial structure with the PSF is sufficient [14, 134].

Taken all these conditions (also eq. (2.27) and eq. (2.29)) into account, eq. (2.26) can be updated to

$$D\left(\vec{r}\right) = \sum_{m=0}^{M} \left\{ \left[ S\left(\vec{r}\right) J_{m,n}\left(\vec{r}_{xy}\right) \right] \otimes \left[ H\left(\vec{r}\right) I_m\left(z\right) \right] \right\} \tag{2.30}$$

which is the acquired SIM data in real space. For the transformation of eq. (2.30) into Fourier space, it is convenient that eq. (2.29) turns into

$$\tilde{J}_{\pm m,n}\left(\vec{k}_{xy}\right) = \delta\left(\vec{k}_{xy} \mp m\vec{p}\right) \cdot \exp\left(\pm im\phi_n\right) \tag{2.31}$$

by expressing the convolution of a $\delta$-function as a shift. Now, the observed SIM data in Fourier space can be written as

$$\begin{aligned} \tilde{D}\left(\vec{k}\right) &= \sum_{m=-M}^{M} \left\{ \left[ \tilde{S}\left(\vec{k}\right) \otimes \tilde{J}_m\left(\vec{k}_{xy}\right) \right] \cdot \left[ \tilde{H}\left(\vec{k}\right) \otimes \tilde{I}_m\left(k\right) \right] \right\} \\ &= \sum_{m=-M}^{M} \exp\left(im\phi\right) \tilde{O}_m\left(\vec{k}\right) \tilde{S}\left(\vec{k} - m\vec{p}\right) \end{aligned} \tag{2.32}$$

with $\tilde{O}_m(\vec{k})$ as the Fourier transform of $\tilde{H}\tilde{I}_m$. At this point, two key facts for the principle of SIM can be extracted: On the one hand, in eq. (2.32) the $\tilde{O}_m$ function is extended axially, and therefore more frequencies can be detected. On the other hand, the $m\vec{p}$ term shifts high frequencies in the detectable region (before $O_m$ at $\pm k_0$ cuts of signal). For the reconstruction, it is necessary to computationally move back the known terms $O_m$ and $m\vec{p}$ to their true positions in Fourier space for each SIM frame. A recombination into a single super-resolution data set follows, which will be retransformed into real space (fig. 2.9) [14].

In particular, for 2-beam SIM ($M = 1$) typically $n = 9$ frames are recorded and $n = 15$ frames for 3-beam SIM ($M = 2$) which provides the axial resolution improvement for 3D imaging. This is needed for the reconstruction in order to fully cover all spatial directions and to separate the components $\tilde{S}(\vec{k} - m\vec{p})$ for $m = ..., -1, 0, +1, ....$ The $n^{\text{th}}$ frame $\tilde{D}_n(\vec{k})$, with the phase $\phi_n$, can be written in Fourier space as

$$\tilde{D}_n\left(\vec{k}\right) = \sum_{m=-M}^{M} a_m \exp\left(im\phi_n\right) \underbrace{\tilde{O}_m\left(\vec{k}\right) \tilde{S}\left(\vec{k} - m\vec{p}\right)}_{\tilde{C}_m\left(\vec{k}\right)} \tag{2.33}$$

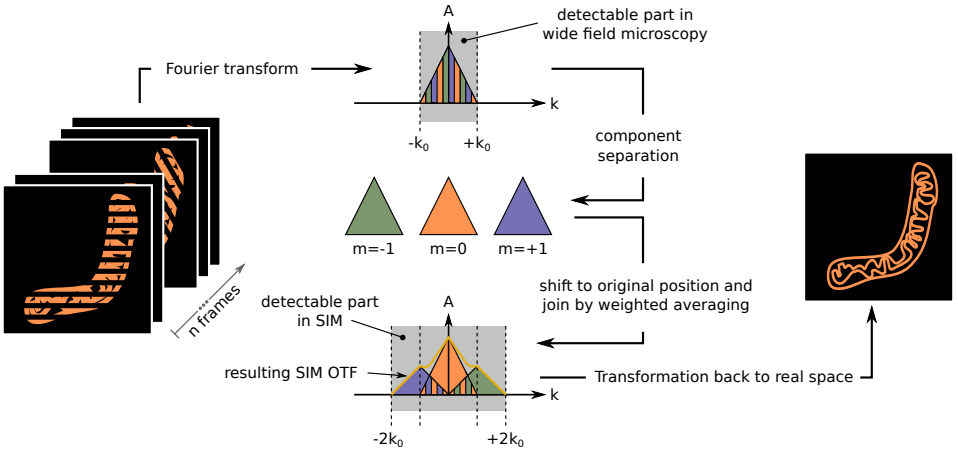


**Figure 2.9.:** Basic principle of SIM. A sequence of $n$ raw frames illuminated with the typical striped pattern for SIM is recorded. For 2D imaging the phase is shifted three times and the pattern is rotated also three time which results in a total stack of $n = 9$ raw frames. Two additional phases are needed for 3D recording if also axial resolution enhancement should be achieved, and therefore $n = 15$ raw frames are imaged. The middle column illustrates the reconstruction along one dimension/angle shift in the frequency domain. Due to the recording of different phases $m$, the mix of overlapping components $\mathbf{C}$ (orange, green, purple) in the wide-field detectable part (cutoff spatial frequency $k_0$) can be disentangled. The single components are now separated and can be shifted back to their original position in the Fourier space, whereas weighted averaging is required. Thus, the detectable part in SIM doubles in Fourier space which corresponds to a super-resolved image [132, 136].

with the Fourier component $\tilde{C}_m(\vec{k})$, which is extended by a factor $a_m$ to introduce the strength of the $m^{\text{th}}$ harmonic, and therefore a determination of the pattern contrast [137]. For the reconstruction, the individual Fourier components $\tilde{C}_m(\vec{k})$ for each SIM raw frame need to be extracted and can be written as components of the vector $\mathbf{C} = \{..., \tilde{C}_{-1}, \tilde{C}_0, \tilde{C}_{+1}, ...\}$. It is convenient to switch to a matrix notation to include all frames and to simplify the calculations. Thus, eq. (2.33) is updated to a vector $\mathbf{D}(\vec{k}) = \{\tilde{D}_1, \tilde{D}_2, ..., \tilde{D}_n\}$ as

$$\mathbf{D}\left(\vec{k}\right) = \mathbf{M}\mathbf{C}\left(\vec{k}\right) \quad \text{with} \quad \mathbf{M}_{nm} = a_m \exp\left(im\phi_n\right) \tag{2.34}$$

where $\mathbf{M}$ denotes the mixing matrix of the various pattern phases $m\phi_n$ for different illumination order $m$ and images $n$. In other words, by using multiple phases $\phi_n$, the sum of differently shifted components can be separated. Because all phases are known and vary from each other, $\mathbf{M}$ can be inverted and the Fourier components can be retrieved from the raw images by a simple inversion of eq. (2.34):

$$\mathbf{C}\left(\vec{k}\right) = \mathbf{M}^{-1}\mathbf{D}\left(\vec{k}\right) \tag{2.35}$$

To achieve an isotropic resolution enhancement, the component separation and data acquisition has to be repeated for $q$ pattern orientation, where the pattern wave vector $\vec{p}_q$ indicates the orientation. Thus, separated components $\tilde{C}_{q,m}$ are introduced which are shifted back to their correct position in Fourier space. For the last step, the recombination of $\tilde{C}_{q,m}$, further processing such as weighted-averaging, generalized Wiener filtering and frequency apodization is carried out. The Wiener filter is adjusted empirically by setting a constant parameter $w$. To avoid hard edges in the effective OTF, which might appear due to the Wiener filtering step, the apodization function $\tilde{A}(\vec{k})$ is introduced. Thus, ringing artifacts in the reconstructed PSF are reduced [134, 137]. A combination of all mentioned process steps for the recombination yields to

$$S'\left(\vec{k}\right) = \frac{\sum_{q,m}\left[\tilde{O}_m^*\left(\vec{k}+m\vec{p}_q\right)\tilde{C}_{q,m}\left(\vec{k}+m\vec{p}_q\right)\right]}{\sum_{q',m'}\left[\left|\tilde{O}_{m'}\left(\vec{k}+m'\vec{p}_{q'}\right)\right|^2\right]+w}\tilde{A}\left(\vec{k}\right) \tag{2.36}$$

where $S'(\vec{k})$ is the sample estimation with higher frequency components and results in a super-resolved image in real space (fig. 2.9) [14, 134]. The pattern orientation $q$ is typically the angle shift ($q = 3$ for 2D and 3D) [14].

The SIM image reconstruction algorithm is realized in several freely available plugins [138–141], so that SIM can be used by large numbers of scientists. However,

artifacts might appear in the reconstructed image due to noise or poor labeling strategies, and therefore the algorithm and theory behind SIM have evolved over the last years. Although eq. (2.36) already considers further image processing, the effect of noise (e.g. Hessian filtering [142]) and other influences are investigated and implemented in several reconstruction algorithm [143, 144]. To evaluate the quality of the SIM reconstructed image and to identify the origin of certain artifacts, an ImageJ/Fiji plugin was published to support the user [145].

#### Experimental realization and applications

One of the most crucial parts of a SIM microscope is the generating of the interference pattern in the sample [146]. First, SIM has been realized on a conventional wide-field setup by integrating an optical grating [13] which is then shifted and rotated mechanically to induce the angle and phase shift. However, this implementation lacks in speed and limits the temporal resolution, so that spatial light modulators (SLM) [135] such as ferroelectric SLM [147, 148] or digital micromirror devices (DMD) [149] are more common and became the standard grating generator. Since SLMs can change their displayed pattern very fast, they are suitable for the recording of fast dynamics [25, 150, 151].

To obtain a raw frame set with sufficient image quality for the SIM acquisition, it is necessary to achieve a high modulation depth which is highly dependent on the polarization settings of the excitation beams and the signal-to-noise ratio of the recorded data [37, 152]. Therefore, a key element of a SIM microscope are polarization optics, which set up and maintain linear polarization of the light. This results in the best interference contrast, and thus, high-quality data reconstruction [153].

Several improvements of SIM made this technique a common tool for various applications [132]. Not only wide-field illumination is possible, also TIRF [154] and HILO-like excitation [155], and even a combination with light sheet microscopy [156] has been developed. Further, in a couple of approaches, SIM has been fused with SMLM which results in a double localization precision [157–159]. The resolution of SIM can be even more improved by optimizing the fluorescence response. Likewise, reaching the region of non-linear dye response also improves the resolution gain by generating higher dynamics in eq. (2.32). Through this, a lateral resolution of 50 nm can be achieved [160]. Additional, SIM can be extended with parallel, multi-planar detection, which enables faster imaging of volumetric samples [161, 162]. Putting all these various applications together, SIM proved to be a very useful method for imaging and analyzing biological and medical samples [1].

## 2.4. Fundamentals of biotechnology

Fluorescence microscopy and nanoscopy is mostly used in applications of biology and medicine due to the opportunity of specific labeling. Samples can be either live or fixed, whereas live-cell imaging is more challenging. Because of potential movement or dynamics, also the temporal resolution has to match [163]. Typically, single cells are exploited because a suitable medium can be chosen according to the applied imaging technique. Tissue, on the other hand, has a certain thickness which causes artifacts if an insufficient method is chosen [1]. However, to gain a better insight and understanding of basic organelles and processes in single cells, this section gives a short introduction.

### 2.4.1. Central dogma of protein biosynthesis

The construction plan of a protein is encoded in the desoxyribonucleic acid (DNA) which is organized as a double helix [164]. The DNA is composed of four nucleotides, namely guanine, adenine, thymine and cytosine and the sequence of these nucleotides encodes the protein (fig. 2.10a). A combination of three nucleotides conceals one of 20 proteinogenic amino acids which are the components of proteins. In case of eukaryotic cells, the DNA is organized as chromosomes inside the nucleus, while in bacteria, the DNA exists in form of ring-shaped plasmids [165, 166].

However, the protein biosynthesis can be separated into two main steps: *transcription* and *translation*. During transcription, the DNA strand is copied to a messenger ribonucleic acid (mRNA) strand which is initiated by the specific enzyme complex RNA-polymerase (RNA pol II in eukaryotic cells) and other transcription factors. The mRNA is a strand of four nucleotides with a few differences compared to the DNA. Further modifications and processing such as splicing of the mRNA strand in some eukaryotes are part of the synthesis process. For the translation, transfer RNA (tRNA) and ribosomes are needed to correlate three nucleotides into one amino acid. This process creates a chain of amino acids which then folds into the protein [167].

The fluorescent labeling of proteins inside single cells can be done in different ways, with the addition of chemical dyes being the simplest. Here, the dye binds to the already existing protein but also false binding might occur. Another possibility is to label molecules of interest with the construction of genetic fusions [168]. The gene coding for a fluorescent protein such as the Green Fluorescent Protein (GFP [169, 170]) or its derivatives [171] is introduced genetically into cells and synthesized [31].

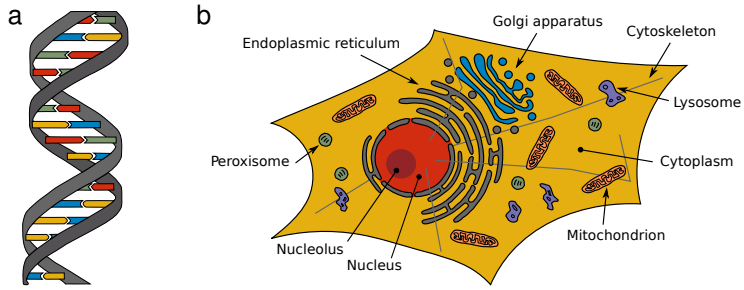


**Figure 2.10.:** Scheme of the DNA structure and an eukaryotic cell. (a) The DNA has a double helix structure with the nucleotides (indicated by the red, yellow, green and blue blocks) organized in the inner part. The sequence of the nucleotides encodes proteins [167]. (b) The displayed organelles (expect the cytoskeleton) are separated from the cytoplasm by a double-layer lipid membrane. Most of these cell compartments are standard counterstains and objects to demonstrate fluorescence microscopy and even nanoscopy [15, 166].

## 2.4.2. Organelles of the eukaryotic cell

Various biological cells have different tasks in order to guarantee a fully functional organism. Nevertheless, the main cell compartments can be found in every cell, separated from the cytoplasm by a double-layer lipid membrane (fig. 2.10b). The nucleus shows several specific functional sub-organizations such as the nucleolus and Cajal bodies. The labeling of the nucleus is a typical counterstain to identify single cells. To transfer and interact with other organelles, nuclear pore complexes (NPC) penetrate the nucleus membrane. NPCs are commonly used to demonstrate super-resolution due to their structure which only can be visualized with nanoscopy. The cytoskeleton stabilizes and moves the cell, and functions as street for transport proteins. Although the filaments of the cytoskeleton such as actin and microtubules are resolvable with conventional wide-field microscopy, the differentiation between single filaments often requires super-resolution imaging. Another big organelle is the endoplasmic reticulum which is most important when it comes to metabolism since the synthesis of proteins (translation steps) occurs at this compartment. Therefore, various dynamics can be observed which makes the endoplasmic reticulum a popular candidate for temporal resolution and counterstaining. Directly attached to the endoplasmic reticulum is the Golgi apparatus,

which further processes some proteins if required. The inner membrane structure of smaller organelles such as mitochondria (energy production), lysosomes (waste handling) or peroxisomes (suppress toxic processes) are only visible with super-resolution techniques. Additionally, these organelles are fairly dynamic so that their imaging is quite challenging [15, 166, 172].

# 3. Live-cell imaging of HIV-1 particle dynamics at the virological synapse with a compact 3D fluorescence microscope

Parts of this chapter have been published in the invited article

Alice Wilking, Lili Wang, Benjamin K. Chen, Thomas Huser, Wolfgang Hübner. Imaging HIV Particles at the Virological Synapse. *G.I.T. Imaging & Microscopy*, 2017.

Fluorescence microscopy has become one of the standard methods for visualizing live-cell dynamics, since it is capable of precise labeling and tracking particles of interest. Research fields in medicine such as virology, however, require certain safety standards to ensure that the scientist performing the research and environment are protected from a potential infection with the investigated virus. Therefore, often collaborations between virologists and microscospists are essential since one provides the suitable laboratory and the other the optical system. Here, the dynamics of HIV-1 at the virological synapse are imaged because that is the scenery where the virus transfer occurs from an infected cell to an uninfected one. For this, a dual-color 3D fluorescence wide-field microscope was utilized, and subsequent deconvolution processing is used to enhance the contrast to better identify virus particles at the virological synapse. In order to confirm the results, fixed, and thus inherently save, samples were analyzed with super-resolution microscopy.

## 3.1. Introduction

The Acquired Immune Deficiency Syndrome (AIDS) is caused by the Human Immunodeficiency Virus (HIV) and currently infected over 78 million people worldwide. Since the start of the pandemic, it causes over 35 million deaths [173]. The heterogeneity of HIV and the exact mechanism behind the capacity of the virus to evade the human immune system, and therefore not induce an effective immune response are poorly understood. It is known that HIV is a retrovirus containing RNA copies of the viral genome. If these copies are transferred into a target cell, reverse transcription occurs. Here, the viral genome is integrated into the DNA of the target cell and the viral proteins replicates through the next protein biosynthesis [174, 175]. The virus can be classified in two groups, HIV-1 and HIV-2, whereas HIV-1 is the principal cause of the pandemic [176]. To gain fundamental knowledge of the disease and its infectiousness, the dissemination pathway of HIV is still under investigation [177].

The virus itself was first isolated in 1983 by Barre-Sinoussi et al. and efforts towards a cure of AIDS began shortly thereafter [178]. One key aspect to gain a basic understanding of the infection process of HIV is the formation of the virological synapse (VS), which is an adhesive structure between an infected HIV cell and a target cell, and thus transfers the virus directly into the target cell [177]. Due to the spherical shape of the virus with a diameter of approximately 120 nm [179] (fig. 3.3a), electron microscopy is one of the standard techniques to image and to analyze the internal structure of the virus [180, 181]. However, the transfer itself can be observed with conventional fluorescence microscopy [182], and the recent development of super-resolution methods such as SIM [183] and STED [184] proved their utility for HIV research.

For this study, the transfer of HIV-1 at the VS was imaged via conventional fluorescence microscopy. Live-cell experiments with such a highly infectious virus requires certain safety standards. Hence, the decision was made to ship a fluorescence microscope to a HIV-1 laboratory [21]. Certain requirements, such as portability and compactness of the optical system needed to be satisfied because the collaborators for this project are located at Icahn School of Medicine at Mount Sinai (ISMMS) in New York City in USA. Such system can be designed by utilizing small industry-grade cameras which additionally reduce the overall costs. Likewise, the operation of the system is required to be user-friendly since the colleagues at ISMMS are not trained imaging specialists. The compact fluorescence microscope remained at ISMMS for several months, and thus a certain stability without technical maintenance had to be guaranteed.

The samples for the experiments were prepared at ISMMS (appendix A.2.2). Here, the viral proteins Gag and Env were chosen to serve as indicators for the transmission of HIV-1. The main purposes of Gag is the initiation of the assembly of the virus particles at the VS and the maturation of the virus after its infection of the target cell [185]. Env on the other side mediates the fusion between host and target cell, so that it is highly required for binding and entry into target cells [186, 187]. In several studies, the two viral proteins Gag [182, 188] and Env [189, 190] were used to investigate and track the VS. Here, the compact fluorescence microscope was utilized for live-cell imaging and the data was further processed by deconvolution to enhance the contrast [67]. Since single virus particles can only be revealed by super-resolution microscopy, fixed and thus inert samples were shipped to the Biomolecular Photonics group in Bielefeld to confirm the results with the super-resolution technique 3D-SIM [14]. Therefore, this study aims at two goals: On the one side, to prove the functionality of the compact fluorescence microscope, and on the other side, to image the transfer of HIV-1 at the VS.

## 3.2. Fluorescence wide-field microscope for 3D deconvolution

The customized microscope was built at the Biomolecular Photonics group in Bielefeld, and therefore a compact design was needed to ship it to ISMMS in New York City, where the HIV experiments were carried out (fig. 3.1a). Basically, the microscope consists of two stacked bread boards, where one holds all the optics for laser fiber coupling and the other is mainly utilized for the detection (fig. 3.1b and c). A detailed list of all used components can be found in appendix A.1. In order to allow for prolonged live-cell imaging, a heating chamber was designed for the microscope. Additionally, a suitable synchronization mechanism was integrated to enable a direct communication between all devices, which allows for high imaging speeds.

### 3.2.1. Construction of the optical setup

The compact fluorescence microscope is a conventional wide-field setup which is specifically optimized to enable fast 3D imaging (compare fig. 2.4). A $z$-scan through the sample is obtained by moving the objective along the optical axis via a piezo. Additionally, an acousto optical tunable filter (AOTF) is integrated for fast switching of the two utilized solid state lasers. With their corresponding

wavelengths, 473 nm and 561 nm, the fluorescent proteins GFP and mCherry can be selectively excited.

In detail, both lasers are filtered (F1 and F2) to suppress unwanted excitation wavelengths and their laser power can be decreased by setting up a neutral density filter (ND). In order to have the same coupling efficiency in the optical fiber for both lasers, it is necessary to overlay the lines and to equalize their beam diameter. Since the beam diameter of the 473 nm laser has a smaller size, it is expanded by a telescope by the factor of two with the lenses L1 ($f_1 = 40\,\text{mm}$) and L2 ($f_2 = 80\,\text{mm}$). By introducing the dichroic mirror D1, with the reflection of the 473 nm laser and transmission of the 561 nm laser, both laser beams can be overlaid. Fast switching rates cannot be obtained by a direct control of the laser, and therefore an AOTF is set up. An AOTF contains a crystal which functions as an optical grating. If the crystal oscillates with a certain frequency, the corresponding wavelength can pass the AOTF. Since the switching between the frequencies can be done in the order of microseconds, a fast switching rate is achieved.

Before both lasers are coupled in the single mode fiber, an expansion of the beam diameter with a telescope (L3, $f_3 = 30\,\text{mm}$ and L4, $f_4 = 200\,\text{mm}$) by approximately 7x is required to guarantee a full illumination of the back-focal plane of the coupling objective. This yields a highly focused spot and thus high coupling efficiency. Approximately 60 % of the incoming laser power is maintained and the optical fiber ensures a Gaussian beam profile. Furthermore, it simplifies the transfer of the laser beams from the excitation board to the detection board.

On the detection board, the beams are first collimated (L5, $f_5 = 20\,\text{mm}$) and then focused (L6, $f_6 = 200\,\text{mm}$) into the back-focal plane of the immersion oil objective (NA = 1.35, 60x magnification) to generate wide-field Epi illumination. Moreover, a white-light LED is mounted on top of the sample to facilitate bright-light illumination. The objective itself is mounted on a $z$-piezo which can move the objective along the optical axis in order to obtain 3D image stacks. The sample itself is placed on a custom-made heated stage to keep the cells alive during the measurements because living cells need a temperature of 37°C. Two resistors are fixed on and thermally coupled to the stage and responsible for the heating process. Additionally, a plexiglas lid can be placed on the stage for isolation. This lid also contains a copper piece with two attached resistors in order to heat the lid, and therefore avoid condensed water which could fall on the sample. All resistors and a temperature sensor are connected to a micro-controller (Arduino Uno), with an additional power supply and a MOSFET (metal-oxide-semiconductor field-effect transistor) switch on an Arduino shield to provide the current used for heating.

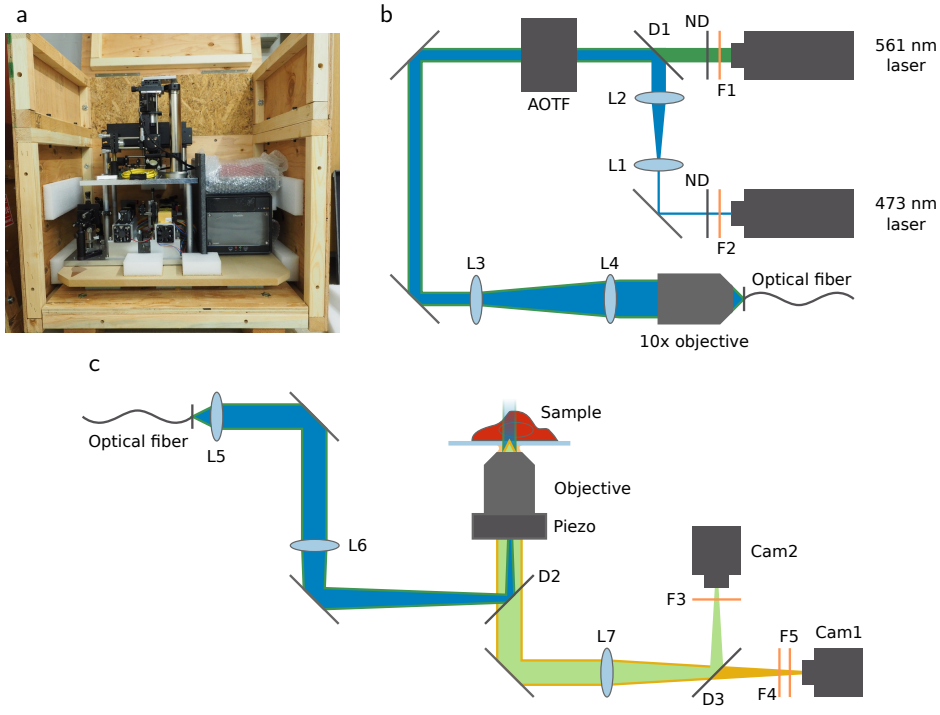


**Figure 3.1.:** Compact fluorescence wide-field microscope for live-cell imaging. (a) The microscope and the corresponding imaging computer are packed in a wooden box (760 mm x 635 mm x 785 mm) to be shipped from Bielefeld to New York City. In this configuration, the excitation board (b) is situated under the detection board (c). (b) Scheme of the illumination pathway on the excitation board. The laser beams are overlaid by the dichroic mirror D1 and selectively pass the AOTF. By coupling both beams in a single mode fiber, the transfer to the detection board is simplified and a Gaussian beam profile is obtained. (c) Scheme of the fluorescence detection board. The laser beams are illuminating the sample via Epi configuration and the objective can be moved along the optical axis via a piezo. The same objective is utilized to collect the fluorescence signal, which is separated from the laser light via D2. One tube lens L7 focuses the mixed fluorescence, which is separated by D3 onto the cameras Cam1 and Cam2. A detailed description of all components can be found in appendix A.1.

On the micro-controller itself, a simple feed-back program is set up to keep the temperature at 37°C.

For the detection of the fluorescence signal and the bright-light image, the same immersion oil objective is used. With a second dichroic mirror (D2) the excitation light is separated from the fluorescence signal by reflecting the laser light and transmitting the detection signal. A tube lens (L7) is utilized to focus the transmitted detection light on the industry-grade cameras (Cam1 and Cam2) which are very small in size and cost-efficient. Thus, the detection breadboard size decreases and additionally, the overall costs were minimized. The fluorescence signal of the two colors is split by a third dichroic mirror (D3). To enable a more compact design, the tube lens is positioned in front of D3. In theory, this placement is suboptimal for image quality, but no adverse effects where observed in the experiments. With the focal length of the used tube lens, a projected pixel size of 97 nm is achieved. Suitable filter sets (F3, F4 and F5) are placed in front of the cameras to block unwanted emission wavelengths and laser light.

### 3.2.2. Communication flowchart between the devices

In order to guarantee fast 3D dual-color imaging, a suitable synchronization mechanism between the components is needed (fig. 3.2a and b). The implementation has to be a customized solution since all components were produced by different manufacturers and no commercial software with corresponding hardware is available. For the control of the data acquisition, the free open-source software $\mu$Manager [191, 192] was used and a synchronization box was build to hold all the required electronics for direct communication (fig. 3.2c and d). For the data acquisition two modes can be used, either the *slow* mode (fig. 3.2a) or the *wavetable* mode (fig. 3.2b). In the slow mode all devices are controlled with $\mu$Manager. However, latency in the software and USB bus system prohibit this mode to reach the required speed. Thus, direct communication through TTL-style (transistor-transistor logic) trigger pulses are utilized for the wavetable mode.

In the slow mode, the user starts the experiment by setting parameters for the data acquisition with $\mu$Manager (fig. 3.2a). The program sends a trigger signal to the connected pifoc-controller which is the control device of the $z$-piezo. Now, the $z$-piezo receives a voltage and moves to the set position. Thus, the objective is placed to the required location along the optical axis and an image can be recorded. By a capacitance feedback the pifoc-controller gets response on whether the $z$-piezo reached the position. Now the cameras are triggered, so that the chip can detect photons. Nearly simultaneously, the cameras forward the trigger signal to the

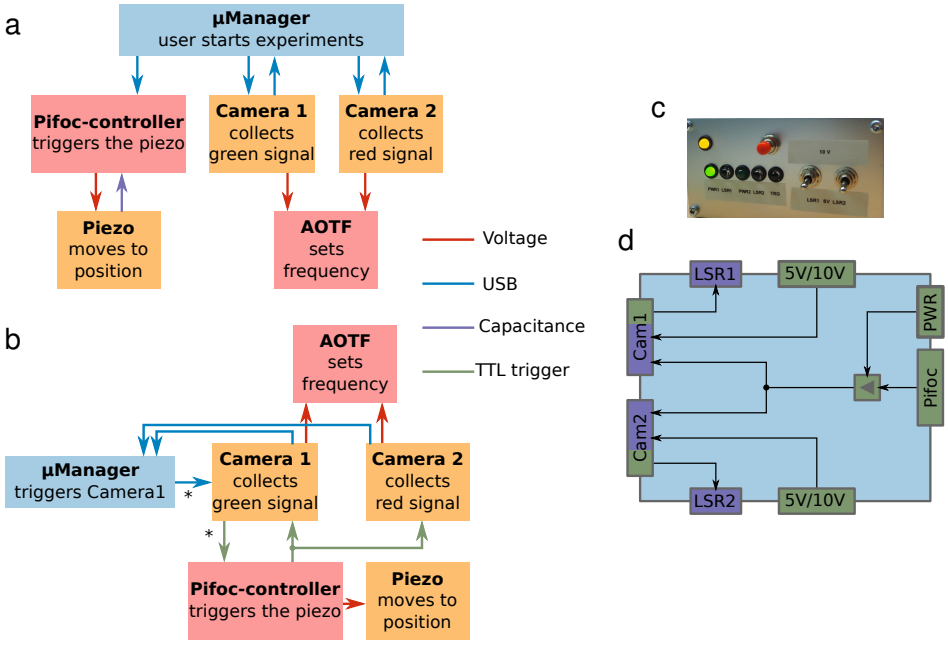


**Figure 3.2.:** Schemes of the communication between the devices and the synchronization box. (a and b) Simplified flowcharts to document the trigger sequence between the devices, where a blue box indicates the direct access by the user, red boxes the hardware control equipment, and yellow boxes illustrate the imaging tools for recording 3D stacks. (a) In the *slow mode*, the user starts the experiment and $\mu$Manager directly controls the pifoc-controller and the cameras through their USB interface. (b) In the *wavetable mode*, $\mu$Manager initiates Camera1 which sends a trigger signal to the pifoc-controller. This happens only during initiation indicated by *. Afterwards, everything is automated by the prestored wavetable on the pifoc-controller. (c) Photograph of the front of the synchronization box. Control LEDs and switches support the full supervision of the data acquisition. (d) Flowchart of the inside of the synchronization box. Here, green indicates outgoing voltages and purple boxes receive the voltage. The output voltage of the pifoc-controller is amplified by a power supply (PWR) and a level shifter, and then triggering the cameras (Cam1 and Cam2). The subsequent signal cascade sets the AOTF to let the lasers (LSR1 and LSR2) pass. A 5 V/10 V switch allows to attenuate the laser power.

AOTF which sets the required frequencies, so that the lasers can illuminate the sample and the cameras are collecting the fluorescent signal.

In the wavetable mode, the achieved frame rate of 11 fps can be further increased to 100 fps by a direct communication between the pifoc-controller and the cameras instead of waiting for the feedback of the $z$-piezo (fig. 3.2b). Here, the $z$-piezo is controlled by its own software and a so-called wavetable, which holds all the position and trigger signals, is implemented and started on the pifoc-controller. Therefore, no feedback of the $z$-piezo, on whether it reached its destination is required. Only the cameras are controlled by $\mu$Manager. In detail, when the user initiates a loop, $\mu$Manager sends a trigger, which is forwarded by Camera1 to the pifoc-controller. Now, the prestored wavetable will be run, so that trigger signals directly reach the cameras and the $z$-piezo. Although high frame rates are achieved, the usage of this mode requires an experienced user since the operation is advanced and some frames might be lost during the acquisition. Thus, experiments that are not time-critical are done by only using $\mu$Manager to control all devices.

For the direct communication between the pifoc-controller, cameras and AOTF a synchronization box was designed to guarantee that all required voltages and trigger signals are send to their corresponding targets (fig. 3.2c and d). First, the signal of the pifoc-controller has to be level-shifted by an additional power supply and level shifter in order to trigger each optocoupler of the cameras. Optocouplers consist of two isolated electric circuits where a photodiode from the first loop sends photons to the phototransistor of the second loop. Thus, the electric signal can be transferred from one circuit to the other. Now, the second loop can send a signal to the AOTF to let the lasers pass and illuminate the sample. Further, a 5 V/10 V switch was integrated, which utilizes the output optocoupler provided by the camera and stabilized a 5 V or 10 V supply in the synchronization box. If the switch is set to 10 V, the full voltage is set at the AOTF and the whole laser power passes. Otherwise, if 5 V is applied, only half of the laser power reaches the sample.

### 3.2.3. Data acquisition and image processing

The data acquisition of 3D fluorescence image stacks with subsequent deconvolution processing starts by turning on the heating stage if live-cell experiments are carried out. After approximately ten minutes, the desired temperature of 37°C is reached, and immersion oil (Zeiss, n=1.518) and the sample are placed on the objective and heating stage. The heating stage itself is mounted on a $xy$-stage with manual micrometer-screws, so that the user can maneuver the sample in lateral direction. Another micrometer-screw is mounted at the pifoc to initially focus the sample.

With the $\mu$Manager software package, the cameras (exposure time and frame rate) and the $z$-piezo ($z$-stepsize and total scan volume) can be set. Furthermore, the $z$-piezo can be used to find the perfect focus since smaller steps in axial direction are available. To adjust the laser power, 10 % ND-filters can be placed in front of the lasers. Additionally, the power can be reduced by 50 % by turning the 5 V/10 V switch to the 5 V position. Of course, a combination of the ND-filters and the switch is possible. If all settings are adjusted, the image can be recorded.

For further deconvolution imaging processing, ImageJ/Fiji [48, 49] and additional plugins were used. First, a PSF according to the Born-Wolf model was generated by using the plugin *PSF Generator* [73] (see section 2.2.4). The recorded image stack needs to be split in the individual color channels for the deconvolution step which was done by utilizing the plugin *DeconvolutionLab2* [76]. The Richardson-Lucy algorithm was chosen as the reconstruction method and 20 iterations were chosen as sufficient. In order to register the color channels, a TetraSpeck (TS) 200 nm bead slide was recorded as calibration sample (appendix A.2.1).

## 3.3. Imaging HIV-1 particles at the virological synapse

The virus transfer was imaged with the compact fluorescence microscope in New York City (ISMMS, Benjamin Chen Laboratory) to get insight of the infection pathway and to demonstrate the functionality of the microscope. Afterwards, fixed HIV-1 samples were brought back to the Biomolecular Photonics group in Bielefeld to further image the virological synapse with super-resolution quality. Here, a commercial system, the Delta Vision OMX v4 from GE Healthcare was used to acquire 3D-SIM data sets.

### 3.3.1. Infection pathway and virological synapse

Research has focused on the infectious pathways of which HIV-1 makes effective use. On the one hand, the virus can enter the host cell when a cell-free virus particle binds to the CD4 and chemokine receptor molecules at the plasma membrane of a T cell [193]. However, in the recent years, it has become increasingly clear, that the virus can also be directly transferred from infected cells to uninfected cells via an adhesive structure dependent on viral proteins, called the virological synapse (VS) [194]. In case of T cell to T cell transfer, the VS is initiated through the interaction of the viral envelope glycoprotein (Env) at the surface of the infected cell and the CD4 receptor expressed by the target cell. The virus then assembles

specifically at the VS, buds and is endocytosed by the previously uninfected cell [179, 182]. The infection though occurs after maturation of the virus particles within the endocytic compartments [193, 195]. The direct transfer by cell to cell contact allows for multiple infection events of a single host cell, and is therefore much more efficient at transferring viral antigen to target cells than the free particle plasma membrane fusion mechanism [182, 196].

### 3.3.2. Labeling and imaging strategies

For the imaging of the transfer at the VS, the virus was labeled through fusions of proteins of interest with fluorescent proteins. The structural protein of HIV-1, Gag, can be labeled through internal insertion of a sequence coding for the fluorescent protein mCherry between the section corresponding to the Matrix and Capsid domain (fig. 3.3b) [198]. This results in an efficient way of fluorescent labeling assembly sites and immature as well as mature viral particles without impairing much of the infectivity rates of such constructs. Double labeling is possible with the use of other fluorescent proteins fused to other viral components. An insertion of sequences coding for super-folding GFP (sfGFP) in the gp120 subdomain of Env at variable loop four was used as the second fluorescent protein (fig. 3.3c) [199]. Different sample sets were prepared, so that either individual proteins were labeled or Gag and Env were stained at the same time.

Jurkat-T cells were chosen as the HIV-1 expressing cell line. After the transfection of the different full replication competent viral genomes containing the fusion of sfGFP-Env and mCherry-Gag, the cells were mixed with a double amount of primary CD4+ T cells (fig. 3.3d). These cells were isolated from HIV-1 negative donors previously. While a majority has dismissed in forming a VS, 10 % to 20 % will show a strong adhesion between HIV+ Jurkat-T cells and one or more primary CD4+ T cells [182]. For the live-cell imaging with the compact 3D fluorescence microscopy, the mixture is now ready to be recorded and the HIV-1 transfer can be visualized. The transfer of HIV at the VS was imaged by recording 3D-stacks (250 nm $z$-stepsize) of the event since the cells have a certain thickness and transfers might occur at several focal levels. However, in order to find a HIV+ Jurkat-T cell, a low laser power was chosen due to potential photobleaching. Furthermore, the heating stage was utilized to get a cell-friendly environment.

In order to image the VS with 3D-SIM, the cells of the mixture were chemically fixed three hours after co-incubation and shipped from ISMMS, Benjamin Chen Laboratory to Bielefeld. The cell mixture represents most of the stages of the viral transfer at the VS. In contrast to the compact fluorescence microscope, the

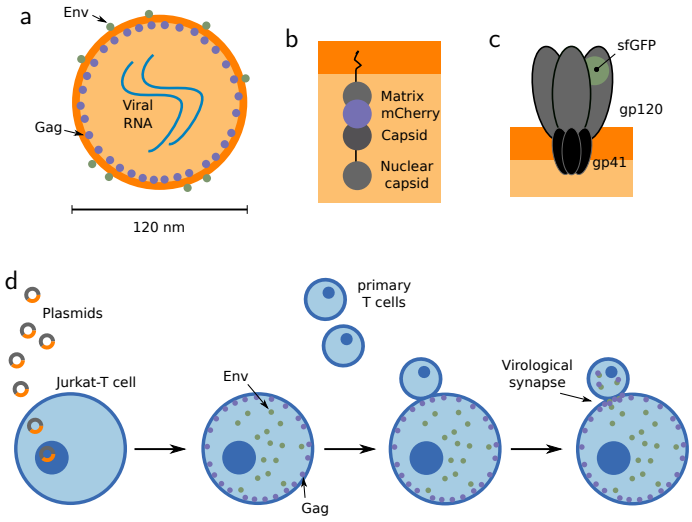


**Figure 3.3.:** Scheme of the labeling and experimental strategy for imaging the HIV-1 infection pathway. (a) Single HIV particle. The protein Env is situated at the outer membrane, whereas the structural protein Gag is prominent at the inner membrane and outnumbers Env. The viral genome will be integrated in the host cell genome after reverse transcription [197]. (b) Structure of Gag with integrated mCherry. (c) Structure of Env with integrated sfGFP. (d) Experimental outline to investigate the HIV transfer at the VS. First, plasmids encoding HIV with the fusions of mCherry-Gag and sfGFP-Env are introduced in the host Jurkat-T cells by gene transfection. The host cell expresses the HIV proteins and Gag will attach to the plasma membrane, whereas Env is most prominent in the cytoplasma. Next, primary T cells were added which attach to the Jurkat-T cell. By an interaction of Env with the CD4+ receptors of the target cells, the VS is formed and the virus assembles at the VS. Subsequent budding leads to a transfer into the target cell.

commercial SIM setup allows for imaging with up to four different stains. Therefore, the plasma membrane was labeled in order to clearly identify the cells and their adhesive connection (appendix A.2.2).

As membrane dyes, FastDiO and WGA-A647 (Wheat Germ Agglutinin bound to AlexaFluor-647) were chosen since both of them have specific affinities for membranes on fixed samples, most importantly including the plasma membrane of the cells. If FastDiO is selected, sfGFP cannot be imaged at the same time because both fluorophores are excited with the same laser. Additionally, DAPI (4',6-diamidino-2-phenyllindole) is utilized as a counterstain for the nucleus.

For the imaging process, the stained cells are mounted in Vectashield which has a higher refractive index as water. Thus, artifacts, which might be introduced by the SIM reconstruction, can be suppressed. 3D-SIM stacks were recorded and then reconstructed with the manufacturer supplied software to obtain super-resolved images. Further image processing such as maximum intensity $z$-projections were also carried out with the commercial software.

### 3.3.3. Visualizing the dynamics of the HIV-1 transfer at the VS

The contrast enhancement by applying the deconvolution methods on the raw data leads to a reduced background so that more details became visible in comparison to the unprocessed wide-field data although the resolution is not enhanced (fig. 3.4a,b,d and e). The data was processed by using DeconvolutionLab2 [76] and by applying a maximum intensity $z$-projection (for more details see section 3.2.3). Since both laser lines are already utilized to excite the two fluorescent proteins for imaging the HIV interaction, there is no channel available to use a fluorescent counterstain in order to visualize the cell itself. However, it is possible to record a bright-light image with a white-light LED at the end of the imaging process, so that a mapping of the host and target cells can be done (fig. 3.4c and f). There is a delay of a few seconds between the last fluorescence image and the bright-light image due to the manual switch at the LED. Thus, the merge of these images does not result to a sufficient overlay which can be easily improved if the LED would be controlled via software. Nevertheless, the fluorescent cells can be correlated to those of the bright-light image.

The modification of Env and Gag by inserting sfGFP and mCherry does not affect the infectivity of the virus which is also reflected in the images (fig. 3.4) [198, 199]. Here, as expected, Env is mainly situated in the cytoplasm while Gag attaches to the plasma membrane and low intensities are diffuse in the cytoplasm. Fluorescent signal from mCherry can be detected from the top and/or the bottom

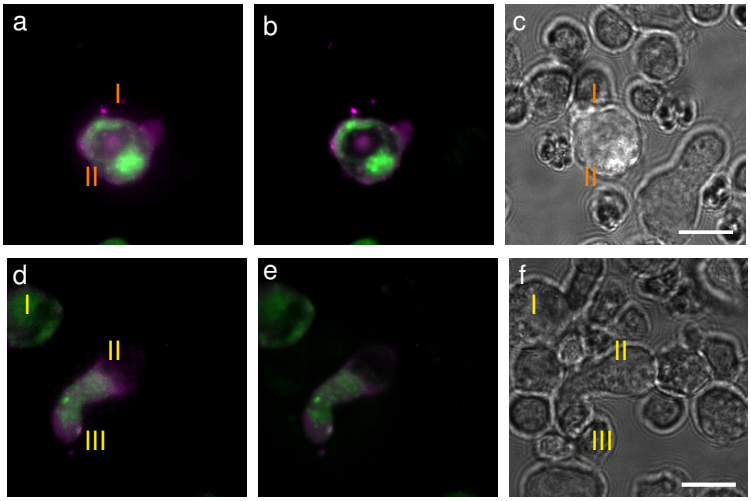


**Figure 3.4.:** Jurkat-T cells expressing HIV particles. mCherry-Gag (purple) is mostly prominent at the plasma membrane, whereas sfGFP-Env (green) is located in the cytoplasm. The deconvoluted images (b and e) show an enhanced contrast in comparison to the wide-field data (a and d). Both data sets are maximum intensity $z$-projections. The corresponding bright-light images (c and f) were recorded several seconds afterwards. First row: A few target cells are bound to the Jurkat-T cell II, whereas only T cell I seems to form a VS with the host cell which is indicated by the detected virus particles. The previous initiation of the VS and subsequent budding is visible in fig. 3.5. Second row: High expression of Gag and Env in cell II, whereas cell I indicates almost no Gag. The primary T cell III is attached to cell II via a VS at the uropod. The previous transfer of the virus is represent in fig. 3.6. Both data sets: 20 ms exposure time per raw frame, 20 $\mu$m $z$-stack, Scale bar 10 $\mu$m.

of the nucleus (fig. 3.4a and b). Nevertheless, the most interesting part is the formation of the VS and the subsequent transfer of the virus particles. The first row of fig. 3.4 displays the end of the time lapse video of fig. 3.6 and the second row is the end of fig. 3.5. Therefore, fig. 3.4 helps to identify the target cells of fig. 3.6 and fig. 3.5.

The transfer of HIV-1 particles at the VS can clearly be seen in fig. 3.5. According to fig. 3.4c, several target cells might attach to the Jurkat-T cell, whereas only one T cell shows a VS to the host cell. Here, a higher intensity of sfGFP-Env and mCherry-Gag is detected at the connecting localization which can be identified as the VS (fig. 3.5d). The subsequent budding and endocytosis of virus particles are clearly visible through the time lapse images recording (fig. 3.5e-g). Moreover, the transfer of several other sfGFP-Env and mCherry-Gag fusions were imaged.

T cells are highly directional and adopt a polarized morphology which means these cells form two ends, namely a leading edge at the front and a swelling at the end which is called uropod. Research found that Gag mostly accumulates at the uropod, and thus uninfected T cells preferentially form a VS at the HIV-1 Gag-containing uropod rather at the leading edge [200–202]. In this study, a high signal of mCherry-Gag was found at the uropod of a Jurkat-T cell (fig. 3.6b and d) and with the subsequent comparison to the bright-light data, a T cell was confirmed at the connecting spot (fig. 3.4f). Hence, it was definitely a VS formation since a high signal of sfGFP-Env was also recorded at the same accumulation spot (fig. 3.6a and c). According to the time points 6.48 s, 14.58 s and 21.06 s, there might be even two VS. Due to the lack of a counterstain, it is unclear whether two target T cells are bound to the Jurkat-T cell. However, the endocytosis of the virus particles into the target cell seems to transfer different amounts of virus particles. According to fig. 3.6d, various signal intensities were detected. On the one hand, a strong sfGFP-Env intensity in combination with mCherry-Gag can be found at time point 6.48 s, which is quite prominent over the whole time lapse. Smaller amounts of both fluorescent protein intensities were also detected, suggesting that only a few virus particles were transferred. Therefore, to distinguish between single virus particles, super-resolution microscopy is required due to the small size of the virus.

### 3.3.4. Using 3D-SIM to resolve the transfer of HIV-1

For the 3D-SIM measurements, different stages of the T cell to T cell HIV-1 transfer at the VS of fixed samples were imaged (compare fig. 3.3d). In contrast to the recording with the compact fluorescence microscope, the plasma membrane and the nucleus were stained to directly image all contributing cells in the fluorescence

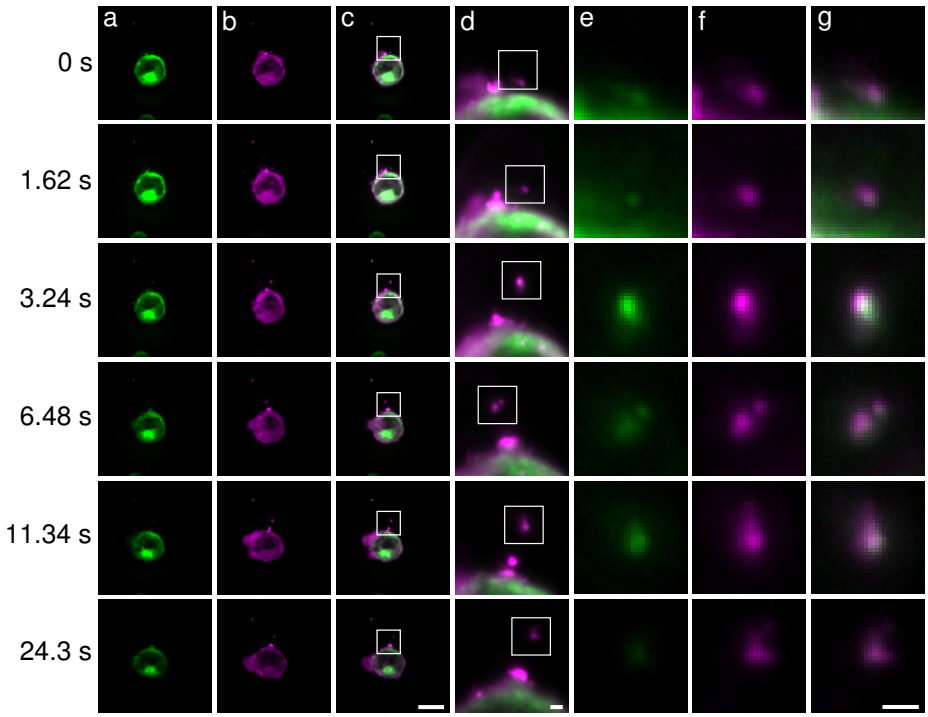


**Figure 3.5.:** HIV-1 particle transfer at the VS. The deconvoluted images are a maximum intensity $z$-projection of a time lapse movie (20 ms exposure time per raw frame, 20 $\mu$m $z$-stack). In (a) the sfGFP-Env channel is displayed and in (b) the mCherry-Gag channel can be seen. The inset (d) of merge (c) shows the transfer of the virus particles. Other insets (e-g) present in (d), demonstrate the merge (g) of the channels (e-sfGFP and f-mCherry) and the matching of the fluorescent signals is visible. Various transfers of HIV-1 particles can be observed. Scale bar 10 $\mu$m(a-d) and 1 $\mu$m(d-g).

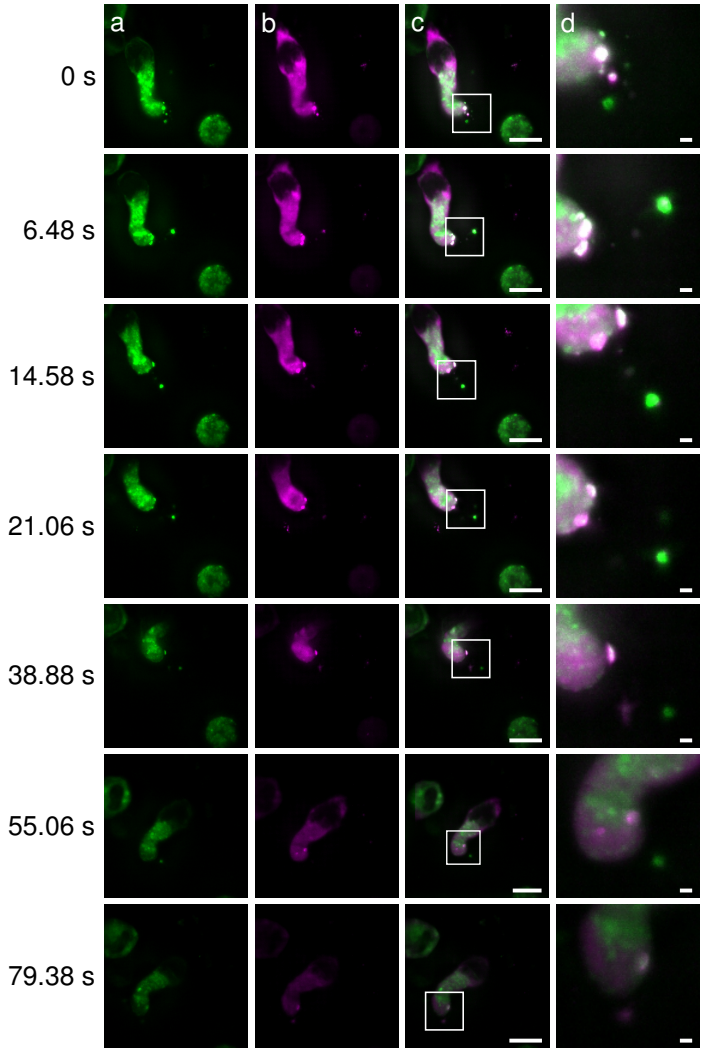


**Figure 3.6.:** Virus transfer at the VS with clear accumulation at the uropod. The deconvoluted images are a maximum intensity $z$-projection of a time lapse movie (20 ms exposure time per raw frame, 20 $\mu$m $z$-stack). The merge (c) of the channels sfGFP-Env (a) and mCherry-Gag (b), with the corresponding inset (d) visualizes strong accumulation of the proteins Env and Gag at the VS and the budding with several subsequent endocytosis by the target cell. Scale bar 10 $\mu$m(a-c) and 1 $\mu$m(d).

image. First, the previous results of the live-cell dynamics need to be confirmed in order to guarantee no deformation is introduced by the fixation.

As already demonstrated in fig. 3.4, the sfGFP-Env fusion appeared mainly in the cytoplasm while the mCherry-Gag complex was predominantly present as an intracellular binding at the plasma membrane where the virus assembles. By additional staining of the plasma membrane, these results can be confirmed and even better visualized (fig. 3.7a). Moreover, as expected, the occurrence of sfGFP-Env at the plasma membrane appears very rare, yet no VS is formed.

After mixing the Jurkat-T cell culture with the target cells, a fraction of cell conjugates can be observed. The virus dependent cell to cell adhesion increases the localization and assembly of mCherry-Gag at the contact area, where the transfer of the virus could be possibly recorded. However, the attachment is only one step of the formation of the VS and if the sample was fixed in that moment, no virus particles might transfer to the target cells. As seen in fig. 3.7b, there are three primary T cells which form this adhesive structure with one Jurkat-T cell. Gag seems to strongly accumulate and assemble at the connecting spot, but there is no visible viral fluorescence signal at the target cells. Therefore, the bounding might just have happened in the fixation moment.

Nevertheless, transferred HIV-1 particles were imaged in target cells (fig. 3.7c and d). Here, the VS is clearly defined by the bright fluorescence intensity of mCherry-Gag at the adhesive structure. For this experiment, only a mCherry-Gag construct was utilized, and thus the usage of the membrane stain FastDiO was possible. This dye proved its better staining process and efficiency (fig. 3.7c and d). Additionally, according to the deconvolution images, a transfer of mCherry-Gag most probably also indicates a transmission of sfGFP-Env. Furthermore, as already seen from the deconvolution data, an attachment of target cells to an infected Jurkat-T cell does not necessarily lead to a transmission of the virus. In fig. 3.7d, three primary T cells are connected to one host cells, but only one target cell is infected. Even single virus particles can be seen at the plasma membrane.

## 3.4. Discussion and conclusion

In this chapter, the functionality of the compact fluorescence microscope was demonstrated by live-cell imaging of the HIV-1 transfer at the VS. By staining two prominent viral proteins, Env and Gag, the transmission of virus particles at the direct cell to cell contact was imaged. Additionally, 3D-SIM image stacks were recorded for further resolution improvement of the different stages of the infection

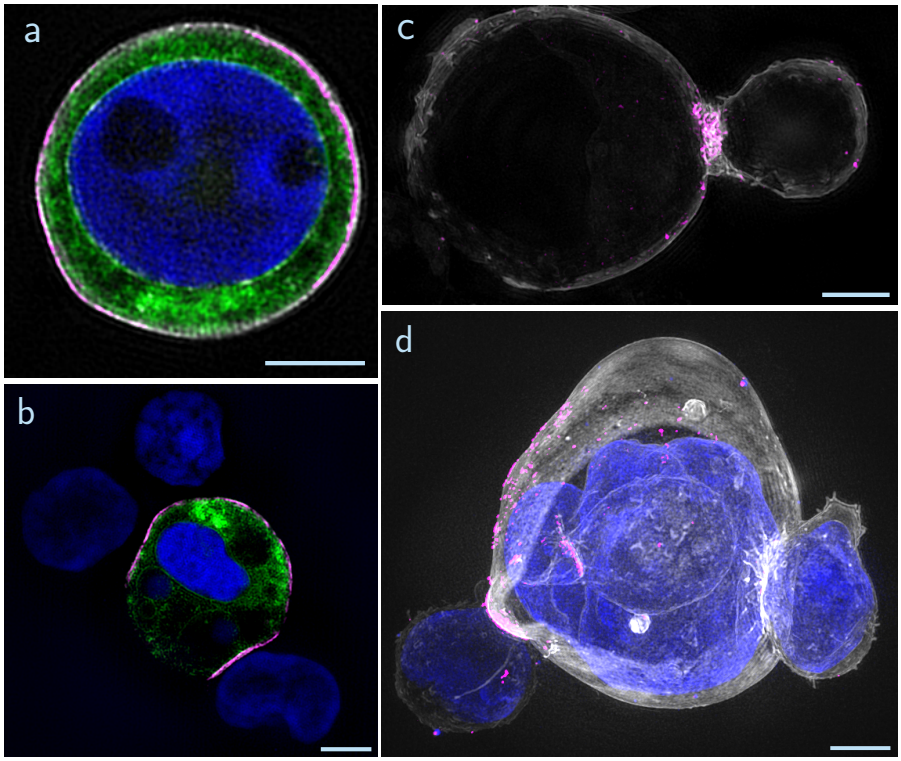


**Figure 3.7.:** 3D-SIM images of the different stages of the HIV-1 VS transfer process (green - sfGFP-Env, purple - mCherry-Gag, blue - nucleus, white - plasma membrane). (a) Fluorescent labeled HIV-1 expressing Jurkat-T cell where Gag can be predominantly localized at the plasma membrane and Env is mostly accumulating in the cytoplasm. (b) Three primary CD4+ T cells are attached to the HIV+ Jurkat-T cell, but no HIV-1 particles were transferred in the target cells. Again, the distribution of Env and Gag is as expected. (c) Transferred virus particles as purple spots are observed in the primary T cell on the right side of the cell. The accumulation and assembly at the VS adhesive structure is clearly visible. (d) Transmission of the virus at only one primary T cell, although three target cells are attached to the Jurkat-T cell (one is in the back). All shown images are maximum $z$-projections of $z$-stacks, 2.5 $\mu$m (a), 2.75 $\mu$m (b), 3.75 $\mu$m (c), 15 $\mu$m (d). Scale bar 3 $\mu$m.

process and to utilize even more fluorescent dyes for locating and identifying the virus particles in the target cells.

The compact fluorescence microscope was successfully shipped from Bielefeld to New York City, set up within a day and aligned to guarantee full performance. Hence, the system proved one of its main purposes, namely the compactness along with the possibility of shipping. On the technical side, all devices maintained their function such as the customized heating stage since live-cell experiments could be carried out on that microscope for several hours. Furthermore, the industry-grade cameras facilitated sufficient image quality and even reduced the overall costs to less than 30k€. Likewise, the synchronization system worked out very well because it is possible to record automated fast 3D-stacks using one software program without disruptions in the communication flow. Thus, the system is user-friendly and indeed the post-doctoral researcher at ISMMS was well trained to operate the system for several months on her own. During this time period, there was no need to maintain the microscope from the technical point of view, so that the optical system can be stated as stable and reliable. To circumvent the absence of multi-color detection, a bright-light source was implemented to the system which was sufficient to identify and map the involved cells of the infection process. The image processing by DeconvolutionLab2 [76] with a determined PSF to deconvolve the recorded 3D $z$-stacks was very convenient and produced adequate images for studying the HIV-1 transmission.

The HIV-1 measurements performed with the compact fluorescence microscope revealed the transmission of virus particles at the VS. By employing fast 3D image stacks, such events were recorded and by applying the deconvolution algorithm the dynamics were visualized with enhanced clarity. The staining of the viral proteins Env and Gag by fluorescent proteins was sufficient, since it clearly showcased the transmission at the adhesive structure. As expected, Gag seemed to be a beneficial indicator for the formation of the VS, since this protein is most prominent at the cell to cell contact. Moreover, the accumulation of Gag at the uropod of a Jurkat-T cell was visualized and the dynamics of possibly endocytosed virus particles were detected. Indeed, the live-cell imaging was agreeable but lacks in terms of resolution and number of available fluorescent stains. Although a subsequent bright-light image was helpful to identify the participating cells, a simultaneous recording would have been more convenient to directly demonstrate the attachment of the plasma membranes of the host and target cells.

HIV-1 samples were also imaged with a 3D-SIM microscope with four color channels in order to improve the experimental settings. As first attempt, fixed

samples were used since the virus is highly infectious and the SIM system was not located in a corresponding safety lab. Nevertheless, the different stages of T cell to T cell HIV-1 transfer at the VS can be imaged by 3D-SIM with significant resolution gain. This makes it possible to resolve single virus particles with a diameter of about 120 nm. Although super-resolution techniques such as dSTORM and STED provide a better resolution gain, the biggest advantage of SIM is its live-cell compatibility with low photodamage. Therefore, a SIM approach has definite advantages for further studies.

# 4. Cost-efficient solution for SOFI with direct camera comparison

This chapter is based in major parts on the peer-reviewed publication

Robin Van den Eynde*, Alice Sandmeyer*, Wim Vandenberg, Sam Duwé, Wolfgang Hübner, Thomas Huser, Peter Dedecker, Marcel Müller. Quantitative comparison of camera technologies for cost-effective super-resolution optical fluctuation imaging (SOFI). *J. Phys. Photonics*, **1** (4), 2019.

and the published preprint

Robin Van den Eynde*, Alice Sandmeyer*, Wim Vandenberg, Sam Duwé, Wolfgang Hübner, Thomas Huser, Peter Dedecker, Marcel Müller. A cost-effective approach to Super-resolution Optical Fluctuation (SOFI) microscopy using an industry-grade CMOS camera. *bioRxiv*, 2018.
(*equal contribution)

Super-resolution (SR) fluorescence microscopy is typically carried out on research microscopes equipped with high-NA TIRF objectives and powerful laser light sources. Super-resolution optical fluctuation imaging (SOFI) is a fast SR technique capable of live-cell imaging, that is compatible with many wide-field microscope systems. However, especially when employing fluorescent proteins, a key part of the imaging system is a very sensitive and well calibrated camera sensor. The substantial costs of such systems preclude many research groups from employing SR imaging techniques. Here, SOFI was examined to what extend it can be performed using a range of imaging hardware comprising different technologies and costs. In particular, the performance of an industry-grade CMOS camera to both state-of-the-art emCCD and sCMOS detectors, with SOFI specific metrics were quantitatively compared. SOFI data can be obtained using a cost-efficient industry-grade sensor, both on commercial and home-built microscope systems, though the analysis also readily exposes the merits of the per-pixel corrections performed in scientific cameras. Additionally, a biplane configuration at the home-built microscope was integrated for multi-focal SOFI.

## 4.1. Introduction

In the life sciences, fluorescence microscopy is an essential tool due to its ability to quantitatively and specifically image biological structures of interest. However, its spatial resolution is limited in a conventional imaging system due to the diffraction of light. To overcome this limitation, a range of super-resolution (SR) techniques were developed and enhanced over the last two decades [1, 203]. These techniques offer a tremendous improvement in spatial resolution, though they typically have at least one trade-off: methods like stimulated emission depletion (STED) or variants of structured illumination microscopy (SIM) maintain high temporal resolution, but require highly complex additions to the microscopes illumination system. Techniques in the group of single molecule localization microscopy (SMLM), on the other hand, require thousands of images to be recorded, and thus yield very low temporal resolution. They also typically require high-end imaging systems, with powerful laser light sources and high-NA objectives, limiting their use to those scientists who have access to such equipment. Driven by this observation, several initiatives were started over the past years to 'democratize' fluorescence microscopy. These aim for a careful trade-off between performance and cost, instead of maximizing system performance. This goal can be achieved by a combination of open-source/open-access software and hardware blueprints, as well as repurposing commodity industrial or consumer hardware [18, 204–209].

Highly sensitive cameras often pose a substantial portion of a microscope's cost. A high-end sCMOS camera, for example, can exceed 10k€ at the time of writing this thesis. In comparison to conventional industry-grade cameras, priced under 1k€, the value of these scientific-grade cameras lies in their higher performance in terms of signal-to-noise ratio (SNR), increased acquisition speed, higher detection sensitivity and extensive manufacturer-provided calibration. Nevertheless, recent work showed that even within the demanding realm of SR microscopy, acceptable to good performance can be obtained with industry-grade components. For example, an industry-grade camera is sufficient for SR techniques based on SMLM such as dSTORM and fPALM, which was confirmed by extensive analysis and characterization of these camera systems [17, 18]. A key reason for this success is the fact that most organic fluorophores are very bright, emitting many photons before photo-destruction occurs, which reduces the overall sensitivity requirements for the camera. Furthermore, the magnification in these systems is typically tuned so that the point-spread function (PSF) is sampled by multiple detector pixels at once, which can reduce the impact of imperfect pixelwise calibration. While localization microscopy provides a very high spatial resolution it does so at a cost to tempo-

ral resolution, with the labeling strategies leading to the highest resolutions even requiring fixation of the sample. However, a vast amount of biological questions requires the use of SR live-cell imaging techniques. Therefore, it is important to question to what extent the inexpensive detectors can also be employed for this purpose.

Super-resolution optical fluctuation imaging (SOFI) [12] is an established SR microscopy method, working not only with quantum dots and organic dyes [123], but also with genetically-encoded fluorescent proteins [210, 211], which is a great asset for biological research. This technique combines an isotropic increase in spatial resolution with a good temporal resolution, rendering it especially useful for living biological samples [210–214]. Like other diffraction unlimited techniques, such as SMLM, the key ingredient for SOFI microscopy is the use of dynamic fluorescent labels. SOFI relies on the statistical analysis of multiple images acquired from the same sample, labeled with fluorophores that show independent and transient non-emissive intermittencies, or 'blinking' behavior (compare section 2.3.3). Probes that display these dynamics, such as photochromic fluorescent proteins, showed to result in a two- to three-fold spatial resolution improvement over the classical diffraction-limited resolution [210, 211]. The SOFI framework even allows for multiplexing of several emitters, with highly similar steady-state fluorescence characteristics, using differences in their blinking behavior [121]. In addition to the conventional visualization of fluorophore distributions, SOFI was used to visualize biosensor activities with similar spatial resolution enhancements [215, 216]. However, in contrast to SMLM, the key of SOFI-based analysis is its reliance on spatio-temporal correlations in the signal. To avoid artifacts, this places rather unusual demands on the image sensor, as the acquisition system itself should not introduce correlations (stemming i.e. from read-out electronics) into the raw images.

In this work, different camera architectures, such as industry-grade CMOS and high-end scientific emCCD and CMOS, were tested and characterized in order to evaluate their functionality for SOFI. The focus was set on the use of genetically-encoded fluorescent proteins, whose overall brightness is considerably lower than those of organic dyes. Further, the home-built, free-standing fluorescence microscope from chapter 3 was utilized to demonstrate SOFI imaging, whereas the implemented components are cost-effective, so that the overall costs could be reduced. Lastly, biplane SOFI recordings were tested with the home-built microscope.

## 4.2. Direct comparison of camera sensors on a scientific microscope

For the direct comparison between three different cameras, a pairwise evaluation through a 50/50 beamsplitter cube was done (table 4.1 and fig. 4.1). This approach allows the same signal (frame by frame image of the sample) to be detected by two cameras, and thus the quantitative analysis is not influenced by sample variation. Two high-end cameras were chosen, which are commonly employed for SR imaging, with two different architectures: the Hamamatsu Fusion (sCMOS) and the Andor Ixon-ultra-897 (emCCD). As third and cost-effective camera, the IDS $\mu$Eye UI-3060CP-M-GL Rev.2 industry-grade CMOS camera (list price around 650€) was utilized (see table 4.1 for characteristics). This latter camera was represented, with a similar purpose, as a viable alternative for dSTORM imaging [18].

### 4.2.1. Microscope setting and data acquisition

The microscope systems and corresponding hardware used for the measurements are described below. For all data acquisition the open-source and freely available Micro-Manager software [191, 192] and a custom device adapter providing full speed for the IDS CMOS camera were utilized [18].

A Nikon Eclipse TI2 motorized microscope was used for the direct camera comparison. Excitation light was provided by an Oxxius L6Cc Laser combiner box coupled to a Nikon Ti2-LA-BF laser illumination unit, providing up to 200 mW excitation light at 488 nm (fig. 4.1). The sample is imaged through an immersion oil objective (1.49 NA, 100x) via Epi illumination, excitation light and fluorescence signal is separated via an imaging-quality dichroic mirror (D1) and matching emission filter (F1) were used. The emission light forms a 100x magnified intermediate image through the tube lens, present in the microscope. A $f_2 = 125$ mm lens (L2) is used to recollimate the light, which then passes the 50/50 beamsplitter cube. It is reimaged onto the cameras through a second lens, which focal length is varied depending on the camera's physical pixel size ($f_{3,4} = 80$ mm, 75 mm, and 200 mm for the sCMOS, CMOS and emCCD, respectively; L3 and L4). In this way, the projected pixel sizes of all three cameras are closely matched to 100 nm (see table 4.1 and table A.2 for more details).

The split ratio of the beamsplitter cube was tested experimentally, to ensure that any imbalance was small enough to not impact the experiments (fig. 4.2a). For this test, three SOFI data sets were analyzed for which the sCMOS camera was mounted on the transmission arm of the beamsplitter, and the CMOS camera

**Table 4.1.:** Technical comparison of the three cameras tested, and focal length used in the 50/50 beamsplitter experiment. The lenses were selected such that the overall magnification for each camera (using a 100x objective, and re-magnifying in the relay telescope) yields closely matching projected pixel sizes in the range of 100 nm. Their exact position can be seen in fig. 4.1 as L2, L3 and/or L4. The pixel sizes quoted are directly calculated from the given focal lengths.

| | Hamamatsu Fusion | Andor Ixon-Ultra 897 | IDS $\mu$Eye UI-3060CP-M-GL Rev.2 |
|---|---|---|---|
| Chip type | Front-illu. sCMOS | Back-illu. emCCD | Back-illu. CMOS (Sony IMX174) |
| Sensor size (pixel) | 2048x2048 | 512x512 | 1920x1200 |
| Pixel size $\mu$m | 6.5 | 16 | 5.86 |
| Quantum eff. (at 518 nm) | 0.79 | 0.95 (0.48 eff.) | 0.77 |
| Read noise | 0.7e$^-$ | <1e$^-$ | 7e$^-$ |
| Readout mode | Rolling shutter | Frame transfer option | Global shutter |
| Telescope lenses (nm) | 125/80 | 125/200 | 125/75 |
| Proj. pixel size (nm) | 101.5 | 100.0 | 97.6 |

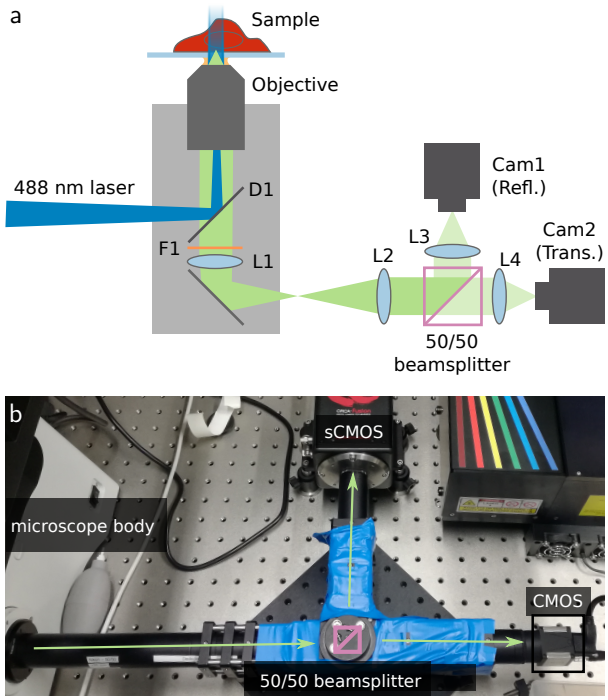


**Figure 4.1.:** Experimental setting to directly compare different cameras for SOFI. A sketch (a) and photograph (b) of the beamsplitter arrangement illustrate the setup in use. The dichroic mirror D1 and the emission filter F1 are parts of the commercial microscope body (gray box). L1 is also part of the microscope body and is normally used to focus the fluorescence image onto a camera. Here, first L2 ($f_2 = 125\,\mathrm{mm}$) is utilized to parallelize the detection beam which is needed to avoid aberrations with the 50/50 beamsplitter. Then, the lenses L3 and L4 focus the beams back onto the camera chips. Varying their respective focal length allows to adjust the projected pixel size of each camera (see table 4.1). The blue tape is used to make the construction fully light-tight. A detailed list of the components used can be found in table A.2.

on the reflective arm, and three data sets where these positions were switched. For each data set, the average frame brightness (in raw counts) was calculated for both cameras, and added to a scatter plot. A linear fit was performed, and the slopes were compared. Any imbalance between the transmission and the reflection arm would show up in a difference in slope between these configurations. From the data it can be verified that the imbalance of the beamsplitter is not more than 1%.

An electronic triggering and light source gating system was used to enable frame-by-frame comparison. The exposure time and frame rate of the industry-grade CMOS camera can be set independently (introducing non-active delays if the frame rate is lower than the exposure time would allow). This camera was used as a 'master clock', as its exposure output was used as a trigger of either the sCMOS or emCCD camera. As the sCMOS device uses a rolling shutter readout, its global reset feature was turned 'on' to enable this mode. The excitation laser was gated through its modulation input and was only activated when both cameras were light sensitive. A microcontroller (ATMEL328, Arduino Uno) was used for this signal processing, and the timing scheme was continuously monitored using a digital storage oscilloscope.

To enable a critical assessment of the camera SNRs and their sensitivity, Cos-7 cells with fluorescently stained microtubules were used. These fiber-like, three-dimensional cytoskeletal structures show a wide variety of thicknesses and exhibit branching, which makes them excellent structures to demonstrate SR imaging. As label, the photo-switching protein, photochromic ffDronpa [220] was linked to microtubule-associated protein 4 (MAP4) (details in appendix A.2.3). The emission spectrum of ffDronpa peaks at about 515 nm (fig. 4.2c), which coincides well with the region of highest detection efficiency of all three cameras (fig. 4.2b). In all cases, the excitation intensity was adjusted in order to obtain an emitter $\tau$-value [121] (decorrelation time) of around one exposure time (fig. 4.2d). This value offers the highest signal for reconstruction using conventional second-order SOFI imaging without lag time.

### 4.2.2. Metric comparison of SOFI reconstructions from the different camera chips

The Localizer [116] package was utilized to reconstruct second-order SOFI data sets which comes with a user interface and analysis framework in the Igor Pro software package (Wavemetrics, Portland, USA). An image stack of 250 frames proved sufficient to clearly showcase the resolution improvement achieved by SOFI and to compare the camera systems both in terms of visual image quality and

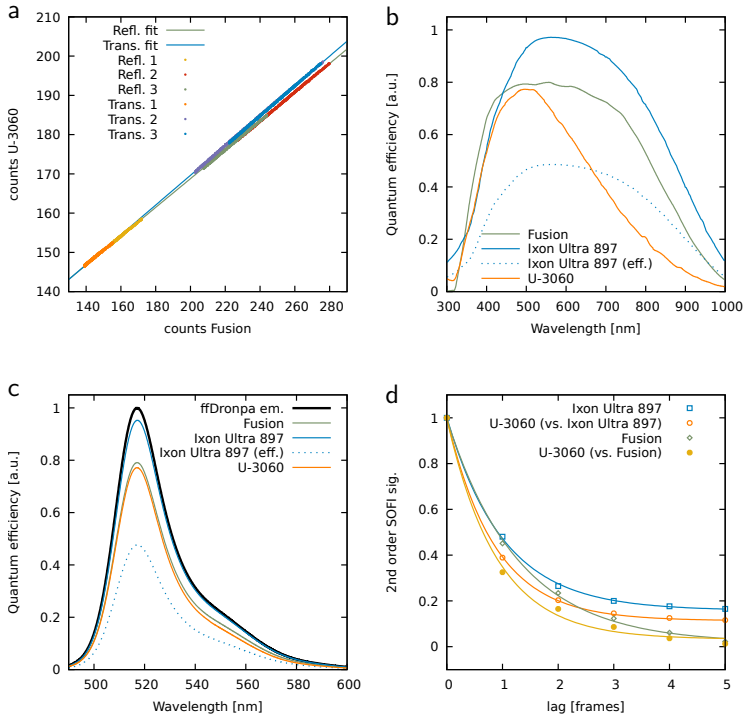


**Figure 4.2.:** Quantum efficiency and calibration of the SOFI experiments. (a) The splitting ratio was tested by swapping cameras between the reflective and transmissive configuration for three samples each and comparing their count slopes. Slope fitting yields an effective splitting ratio of 49 % - 51 % in the beamsplitter cube, which is well within expectation and tolerance for the experiments. (b) The raw quantum efficiency curves provided by the manufacturers show a high sensitivity for green light. (c) To obtain the detection efficiency for ffDronpa, these curves were weighted with its emission spectrum [217, 218] and it becomes obvious all cameras should be well suited to detect ffDronpa. For the emCCD, an effective QE, weighted with a factor of two, is also displayed to account for its readout process [219]. (d) Excitation light levels were tuned so that a $\tau$ of around one was reached for the 40 ms exposure times used in the experiments.

quantitatively. The wide-field images were generated by averaging the 250 analyzed SOFI frames.

In order to evaluate the direct comparison of camera performances for SOFI, three metrics were chosen. First, FRC is used (see also section 2.2.2) which is an established image analysis technique [46, 50, 221] to determine the resolution of an image. Further, SNR calculations were utilized to quantify the image quality. Lastly, spurious correlations introduced by the camera were investigated because SOFI is basically the determination of correlative values, and therefore correlation induced by the camera would result in artifacts (for more details see appendix A.1.2).

### sCMOS vs CMOS

The generated wide-field image (fig. 4.3c) shows in its upper left region lots of out-of-focus light as blur, whereas the lower right part features structures of interest. The SOFI reconstruction of the sCMOS camera (fig. 4.3a) both removes the out-of-focus contribution, and enhances resolution so fibers can be separated much more clearly. The SOFI reconstruction of the CMOS camera yields comparable results (fig. 4.3b), whilst also showing higher noise levels, which is in line with expectations as the camera read noise is approximately 10x higher (table 4.1).

According to the FRC resolution, the current-generation sCMOS camera slightly outperforms the CMOS camera (fig. 4.3d). In brief, the corresponding FRC graph shows the correlation between two independent measurements of the same sample structure with respect to their spatial frequency, and thus feature size. The higher this correlation is, the more contrast or SNR is to be expected for a certain structure size. By its correlative nature, FRC incorporates a frequency-dependent estimation of SNR, and is in general a popular technique to provide model-free resolution estimates. However, its application to arbitrary datasets and especially as a tool for camera comparison is not without hurdles (see discussion section fig. 4.7).

Thus, a direct estimation of the image SNR value, by fitting a model accounting for background, out-of-focus contribution and the desired in-focus signal component to the data is a more robust comparison (fig. 4.3e). In detail, 18 data sets were analyzed in terms of their SNR value (fig. A.1 and fig. A.2). From these, it can be concluded that the sCMOS system consistently provide a higher SNR than the CMOS system with a range of typically 1.5x to 2.4x higher SNR on the sCMOS system (table 4.2). Additionally, the position of the cameras did not influence the SNR analysis which was already confirmed by fig. 4.2a since both cameras detect basically the same amount of photons.

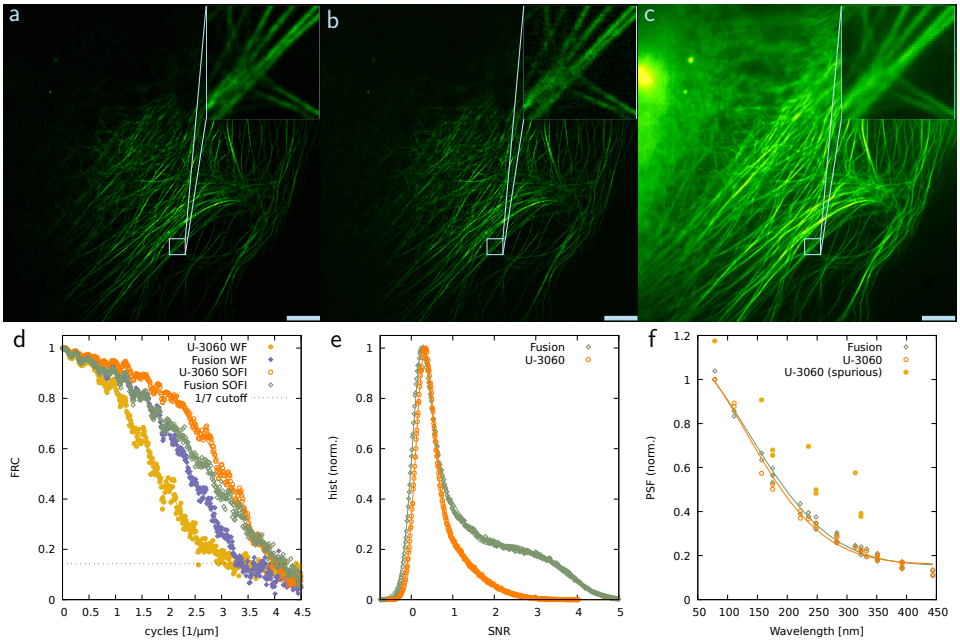


**Figure 4.3.:** SOFI imaging comparing the sCMOS to the CMOS camera. The microtubules of the Cos-7 cells were stained with ffDronpa. Visually, the SOFI reconstructions (a-sCMOS and b-CMOS) obtained with both cameras provide a clear resolution improvement and background reduction over the wide-field image (a), while the CMOS data arguably appears somewhat noisier and grainier. (d) The resolution, measured via FRC, reflect this, where the CMOS camera picks up more noise both in the wide-field and in the SOFI analysis. (e) Similarly, the SNR ratio is higher for the sCMOS camera. (f) The determination of the PSF had to be modified in order to avoid wrong conclusions due to spurious correlations. Importantly, cross-pixel correlations, which are a typical artifact of CMOS technology, are unsurprisingly present in the CMOS datasets, but seem heavily reduced in the current-generation sCMOS chips tested here. Scale bar 10 $\mu$m, inset 5 $\mu$m x 5 $\mu$m.

**Table 4.2.:** SNR results for each dataset shown in figs. A.1 and A.2. The raw SNR values for each camera type are provided in rows two and three, as well as their quotients (SNR Hamamatsu Fusion / SNR IDS U-3060) in row four. This allows to easily assess that IDS U-3060 CMOS camera system consistently produces consistently lower SNRs than the Hamamatsu Fusion sCMOS system. *HrIt* indicates that the Hamamatsu camera was situated on the reflective path of the beamsplitter, whereas the IDS camera was placed at the transmission path. *HtIr* describes the opposite situation.

| Data set | sCMOS | CMOS | Quotient |
|---|---|---|---|
| D17-HrIt-C1 | 2.180 | 1.005 | 2.171 |
| D17-HrIt-C2 | 2.797 | 1.179 | 2.371 |
| D17-HrIt-C3 | 1.890 | 1.116 | 1.694 |
| D17-HrIt-C6 | 2.649 | 1.520 | 1.743 |
| D17-HrIt-C7 | 2.415 | 1.304 | 1.852 |
| D17-HrIt-C8 | 2.084 | 1.322 | 1.577 |
| D17-HrIt-C10 | 1.969 | 1.216 | 1.618 |
| D17-HrIt-C11 | 2.315 | 0.957 | 2.420 |
| D17-HrIt-C12 | 2.414 | 1.162 | 2.078 |
| D17-HtIr-C1 | 1.726 | 1.123 | 1.538 |
| D17-HtIr-C2 | 2.204 | 1.198 | 1.840 |
| D17-HtIr-C4 | 3.786 | 1.764 | 2.146 |
| D17-HtIr-C6 | 2.470 | 1.383 | 1.786 |
| D18-HtIr-C3 | 2.299 | 1.601 | 1.436 |
| D18-HtIr-C4 | 2.280 | 1.437 | 1.587 |
| D18-HtIr-C5 | 2.225 | 1.324 | 1.680 |
| D18-HtIr-C6 | 1.486 | 0.961 | 1.546 |
| D18-HtIr-C8 | 2.460 | 0.524 | 4.693 |

Another quality criteria is the introduction of spurious correlations (the signal in a given pixel influencing its neighbors) by the camera (fig. 4.3f). For a SOFI analysis, these correlations appear when extracting the PSF shape from the SOFI raw data, a processing step initially developed and typically employed to cross-check instrument alignment. Here, no additional correlations stemming from the camera are detected in the sCMOS camera, while clear spurious correlations are observed in the CMOS which will serve as a (limited) source of bias in the SOFI imaging. This might also explain unphysically high correlations in the uncorrected FRC signals which will be discussed later in detail.

### emCCD vs CMOS

Comparing the emCCD and the CMOS sensors, surprisingly, both cameras perform much more similar, and the CMOS camera slightly outperforms the emCCD system. Again, one representative data set was chosen for a full analysis (fig. 4.4) and further data sets to underline the results (table 4.3). The SOFI reconstruction of the emCCD camera (fig. 4.4a) enhances resolution, so that two fibers not distinguishable in wide-field (fig. 4.4c) can now be separated. The SOFI image obtained via the CMOS camera yields the same improvement, with arguable higher contrast in all areas within the sample (fig. 4.4b). To understand this performance difference, it is important to know that the pure photon counts reached in SOFI experiments heavily favors CMOS technology.

Likewise, the CMOS camera perform better for SOFI reconstructions than the emCCD according to the achieved FRC resolution (fig. 4.4d) and the SNR analysis (fig. 4.4e). Here, the FRC curve of the industry-grade camera clearly crosses the 1/7 threshold at a higher cycle rate, and therefore achieves a higher resolution. Also the SNR graph shows that the CMOS camera is shifted towards higher values in comparison to the sCMOS camera. To further confirm these results, six SNR data sets were evaluated, which consistently show the SNR of the CMOS camera to be 1.2x to 1.4x higher than on the emCCD camera (fig. A.3 and table 4.3). However, the emCCD system does not show spurious correlations in the extracted PSFs, which the CMOS system continues to introduce and will be discussed later (fig. 4.4f). The results might seem surprising, given that emCCD systems are typically viewed as very sensitive, but are explained by the average amount of photons observed per pixel, and the resulting read noise and shot noise statistics.

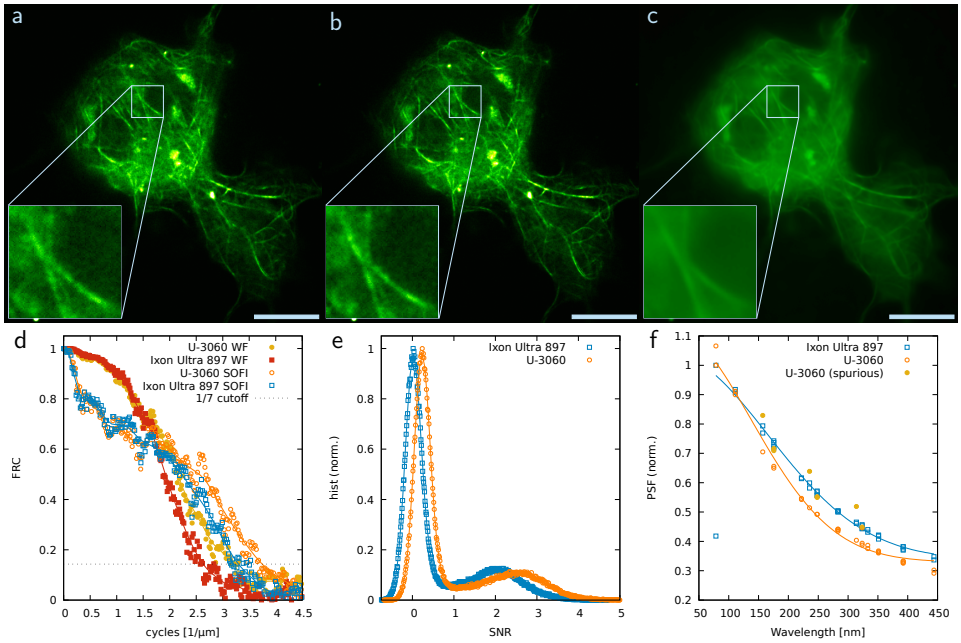


**Figure 4.4.:** SOFI imaging comparing the emCCD to the CMOS camera. The microtubules of the Cos-7 cells were stained with ffDronpa. Again, the background reduction in the SOFI reconstructions (a-emCCD and b-CMOS) are clearly visible in comparison to the generated wide-field image (c). The CMOS camera outperforms the emCCD in the achieved FRC resolution (d) as well in the SNR analysis (e). However, the emCCD does not show spurious pixel correlations in the PSF analysis typical for CMOS technology (f). Scale bar 10 $\mu$m, inset 5 $\mu$m x 5 $\mu$m.

**Table 4.3.:** SNR results for each dataset shown in fig. A.3. The raw SNR values for each camera type are provided in rows two and three, as well as their quotients (SNR Andor Ixon / SNR IDS U-3060) in row four. Here, the IDS U-3060 CMOS camera system consistently produces slightly higher SNRs than the Andor IXON emCCD camera system. *ArIt* indicates that the Andor camera was situated on the reflective path of the beamsplitter, whereas the IDS camera was placed at the transmission path.

| Data set | emCCD | CMOS | Quotient |
|---|---|---|---|
| D16-ArIt-C9 | 1.643 | 1.993 | 0.824 |
| D16-ArIt-C10 | 1.853 | 2.501 | 0.741 |
| D16-ArIt-C11 | 2.374 | 3.341 | 0.711 |
| D16-ArIt-C13 | 1.347 | 1.835 | 0.734 |
| D16-ArIt-C14 | 1.597 | 1.899 | 0.841 |
| D16-ArIt-C15 | 1.349 | 1.717 | 0.786 |

## 4.3. Setting up cost-effective SOFI on a home-built system

### 4.3.1. Verifying SOFI performance of the CMOS sensor

Home-built systems offer a combination of flexibility and lower cost compared to commercial systems, and therefore present attractive avenues for reducing the overall cost of SR imaging. Here, the compact fluorescence microscope introduced in chapter 3 was utilized and modified to perform SOFI measurements with the already implemented industry-grade CMOS cameras. In comparison to chapter 3, the stacked design was removed and the manual $xy$-stage to move the sample was replaced with a more robust sample holder. As a reminder, the system is comprised of a 50 mW, 473 nm diode laser and a 60x, 1.35NA oil immersion objective in Epi fluorescence configuration. The second laser attached to this system was not used for the experiments. Nevertheless, due to this second laser additional lenses were present in the excitation pathway of the 473 nm laser, which would not be necessary if only ffDronpa is used. An acousto-optic tunable filter (AOTF) was utilized to enable fast switching rates of the laser, only illuminating the sample during data acquisition, reducing photobleaching effects to a minimum.

In contrast to chapter 3, a 250 mm tube lens was used to obtain a projected pixel size of 70 nm (see fig. 3.1 and fig. 4.5a). At a given resolution limit of about 195 nm,

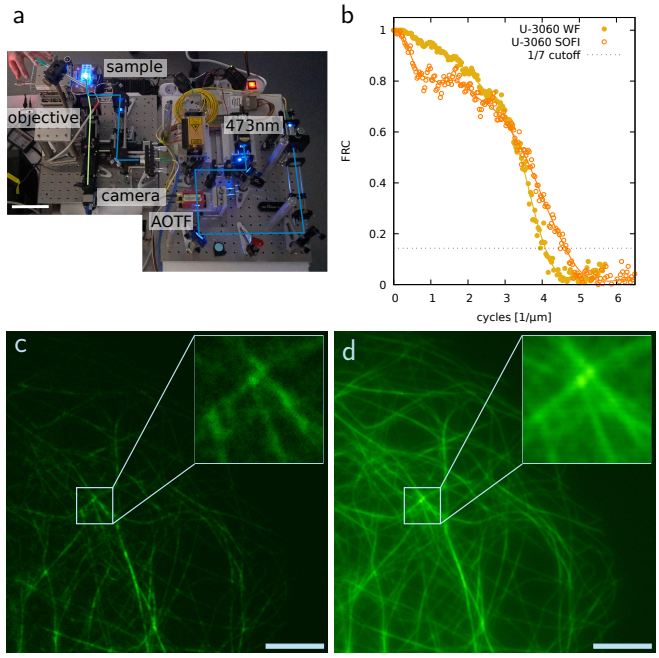


**Figure 4.5.:** SOFI imaging on the home-built microscope system (see also fig. 3.1) with the CMOS camera. (a) A photograph of the system during a measurement with the blue line representing the laser and the green one the detected fluorescence signal. Scale bar 10 cm. Again, microtubules of the Cos-7 cells were stained with ffDronpa. The achieved resolution improvement is verified by the FRC plot (b). Also visually, the SOFI reconstruction (c) exhibits more details and reduced background in comparison to the generated wide-field image (d). Scale bar 10 $\mu$m, inset 5 $\mu$m x 5 $\mu$m.

this slightly over samples the detection. However, since the field of view of the CMOS chip is very large, this configuration was preferred to allow for a telecentric 2f configuration. While more limited in operation (no motorized $xy$-stage) and flexibility (only two fixed laser excitation lines in the case of this system), the image quality is comparable to a research microscope (fig. 4.5b-d). Overall, the detection part of this system and optics needed for this SOFI experiments can be bought and self-assembled at a total cost of about 16.5k€, which is much lower than the cost of typical SR instruments.

The SOFI measurements performed on this system do not pass a beamsplitter arrangement, so all photons are collected on the same camera. This of course greatly improved the raw signal's SNR, and thus the achieved FRC resolution of the system (as it relies on an SNR cutoff). However, using a single camera is of course closer to a 'real world' application of the system, and showcases the quality one could reach in SOFI imaging when employing this type of cost-efficient hardware.

The visual results again show a clear reduction in background and an improvement in resolution when comparing wide-field (fig. 4.5d) and SOFI reconstruction (fig. 4.5c). This is mirrored by the FRC data obtained for those images (fig. 4.5b). Since a camera comparison was not performed on this system, a SNR analysis is not meaningful, as it is highly sample-dependent (changing with staining efficiency, expression levels and such) and thus requires a direct, frame-by-frame comparison.

### 4.3.2. Biplane SOFI approach

Now, the flexibility of this system was used to straightforwardly introduce an additional industry-grade camera via a 50/50 beamsplitter for biplane imaging (fig. 4.6). The experimental setting is analogous to fig. 4.1. Both cameras can be made to visualize a different depth within the sample by positioning them at different distances from the tube lens. Calibration measurements and analysis show that these two planes are 543 nm ± 15 nm apart.

In detail, a 200 nm diameter TetraSpeck bead slide was used to calibrate the biplane data. The beads were diluted in doubly distilled H2O with a 1 to 1000 concentration and then mounted in glycerol on a #1.5 glass cover slip. First, one of the CMOS cameras was adjusted, so that it was focusing into the sample. Then, the objective was moved with the $z$-piezo of the compact fluorescent microscope by 500 nm along the optical axis and the second CMOS camera was focused to this plane. For the correct analysis of the distance between the planes, a $z$-stack extending over 10 $\mu$m with 50 nm $z$-stepsize was recorded and analyzed.

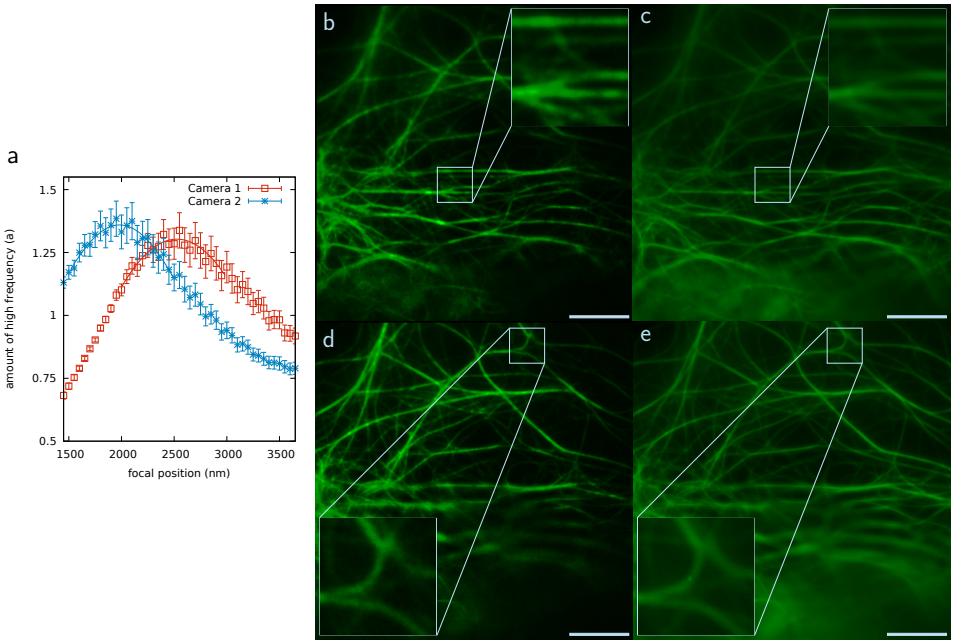


**Figure 4.6.:** SOFI imaging on the home-built micorscope system in biplane configuration. (a) Focus alignment for the biplane detection system. To obtain this alignment, a layer of fluorescent beads was imaged and analyzed. The distance between the two focal planes is 543 nm ± 15 nm. Also for the biplane imaging, microtubules of the Cos-7 cells were stained with ffDronpa. SOFI image (b) and wide-field image (c) of the first focal plane which was in the middle of the image. The second focal plane was at the upper part of the image indicated by the corresponding SOFI image (d) and wide-field image (e). In both cases, the background reduction in the non-focal region is clearly visible. Scale bar 5 $\mu$m, inset 3 $\mu$m x 3 $\mu$m.

Here, an exponential function $b \cdot \exp(-\frac{k_x}{a}) + c$ was fitted to the power spectrum of each recorded image plane to estimate their frequency distribution. The approach here is that when the beads come in focus, more high frequency signal is picked up by the microscope, and thus $a$ increases towards best focus. Empirically, this approach seems to work well and surpasses observing single beads in terms of noise and stability. By plotting the amount of high frequencies $a$ against the objective lens position for both cameras, and finding the maximum of both curves, the focus position is found for both cameras, with $f_{cam2} = 1982\,\text{nm} \pm 8\,\text{nm}$ and $f_{cam1} = 2525\,\text{nm} \pm 13\,\text{nm}$, which yields a focal plane distance of $543\,\text{nm} \pm 15\,\text{nm}$ between the cameras (fig. 4.6a). The determined value was consistently for different test datasets.

Since the emission light was splitted equally between the two cameras, each separate plane only has half of the photons available for SOFI analysis compared to single plane acquisition. The used laser power was similar to the power for the single plane data. However, due to splitting the signal between both cameras, the loss over time due to photobleaching of the fluorophores had a greater impact on the SOFI image reconstruction of the biplane data. Nonetheless, this biplane data still proved adequate in order to achieve clear SOFI reconstructions, using 350 raw frames, acquired at 20 ms per frame, and thus less then 8 s total experiment time (fig. 4.6b-e). The background reduction in the different focal planes of the SOFI reconstruction compared to the wide-field images are clearly visible.

## 4.4. Discussion and conclusion

The results of this chapter provide a quantitative comparison of both a state-of-the-art sCMOS and an established, high-end emCCD camera with a CMOS solution targeted at industrial applications, with metrics specific to SOFI imaging.

In detail, the industry-grade CMOS camera is clearly capable of acquiring SOFI data sets of sufficient quality on realistic day-to-day samples, even when using fluorescent proteins as labels. In a direct comparison, its image quality is not on par with a current-generation sCMOS system. The images are visually noisier, and the associated SNR and FRC metrics (which implicitly includes an SNR-style weighting) reflect this. This is to be expected, as both cameras share the same sensor technology, but the 'scientific' CMOS implementation is much more refined in terms of read-out noise and calibration.

In direct comparison of the emCCD and the CMOS systems, both the visual image quality and the SNR and FRC metrics are almost on par. The CMOS

camera even performs slightly better than the emCCD system, which might seem surprising, as the emCCD system is of course equally fine-tuned to scientific applications. However, the difference in sensor technology, especially the reliance on the electron-multiplication stage, puts the emCCD system at a disadvantage for the photon count levels used in SOFI imaging.

Looking at both these findings and the signal formation aspect of SOFI imaging, two technical characteristics seem to influence SOFI imaging quality the most: mainly the quantum efficiency of the sensor, and secondarily its read noise. The Sony sensor employed by the IDS U-3060 CMOS camera system provides a high quantum efficiency in the green, with a pronounced fall-off towards red and infrared light (fig. 4.2b). As the sensor is marketed for a broad range of applications, and is available in a variety of industry-grade camera systems, this is a sensible optimization by the manufacturer. For the application presented here, this aligns well with the green (peak at 515 nm) emission spectrum of ffDronpa (fig. 4.2c) and yields a detection efficiency almost identical to the sCMOS camera system (for red and far-red emitting dyes, as often used in dSTORM microscopy, there would be a significant difference in detection efficiency). The difference between the sensors manifests in their read noise characteristics, where the sCMOS camera yields $0.7e^-$ to $1.4e^-$ (depending on readout speed) compared to $7e^-$ for the Sony sensor. It is expected that a typical 'blink' of ffDronpa will yield a few hundred photons distributed over the pixels sampling its PSF, so this change in read noise is likely the main reason for the change in SOFI SNR.

The emCCD sensor provides an even higher quantum efficiency over the full spectral range, but at these typical SOFI photon count levels, the excess read-noise introduced by the electron multiplying stage cannot be compensated by the higher quantum efficiency (plots in fig. 4.2b and c include the typical [219] 2x weighted quantum efficiency plot for the emCCD chip to account for this effect). This effect is documented in comparisons of sCMOS and emCCD technologies, where emCCD systems for some time now are only recommended for the lowest photon count levels, and seems to hold even for current-generation, industry-grade CMOS technology.

Further, sensor readout uniformity, linearity and 'spurious correlation' influence the quality of a SOFI image. While uniformity and linearity are already well documented [18], the effect of inter-pixel correlations becomes very apparent in SOFI imaging: If a signal, typically of a high photon count, spatially or temporally influences the count rate in neighboring pixels, this effect shows up as an unreasonably high correlation in the PSF-estimate plots (fig. 4.3f and fig. 4.4f). Additionally,

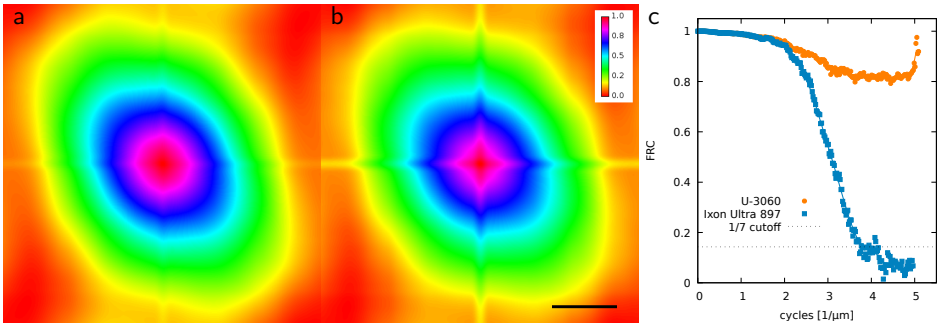


**Figure 4.7.:** Normalized Fourier correlation for 250 averaged images acquired with the emCCD (a) and CMOS (b) and corresponding FRC plot (c), based on the data set displayed in fig. 4.4. Correlation due to the cell sample structure and CMOS chip architecture introduce artifacts with yield to an unreasonably resolution estimate. Scale bar, 2 cycles/$\mu$m.

any fixed pattern signal inherent to the camera sensor will adversely affect FRC as a resolution metric, as it introduces (false) correlations into a signal not stemming from the band-limited microscope. In extreme cases (fig. 4.7) this effect yields FRC curves that are physically impossible and is thus easy to spot. The plots of fig. 4.7 highlight two stumbling blocks in applying FRC to the data sets. The sample structure is convoluted with the FRC analysis visible in the diagonal elongation of the correlation signal in both plots (fig. 4.7a and b). Typically, a round green/yellow spherical shape would be expected. Additionally, the CMOS chip introduces strong correlation along the $x$- and $y$-axis (strongly visible in fig. 4.7b), which leads to unphysically high resolution estimates in the FRC plot (fig. 4.7c) which are well beyond the instruments pass band. Thus, FRC should be applied with care in these situations, and the more robust SNR estimates should be chosen for a comparison of multiple data sets (figs. A.1 to A.3).

Causes for these correlations can be both non-uniform pixel cross-talk and latent effects in the read-out electronics. Here, both the emCCD and the sCMOS cameras seem to be highly calibrated and optimized, both showing no spurious correlations, while the industry-grade CMOS system shows a moderate amount of correlation not stemming from single molecule blinking. While these signals become apparent in an in-depth quantitative analysis, they still seem to be controlled enough to not have an adverse effect on image quality.

While the industry-grade camera itself already allows for significant cost saving,

moving from a commercially obtained microscope body to a completely home-built solution, further reduces the costs. This system, derived from the design in chapter 3, follows the design ideas proposed for cost-effective localization microscopy, which allows it to be constructed from readily available opto-mechanical components. The samples on this fully home-built microscope were recorded with the industry-grade CMOS camera, which resulted in super-resolved images with good SNR.

Lastly, this work went further by even implementing biplane imaging on the home-built imaging system. Due to the low price point of the industry-grade CMOS cameras, a second or even multiple cameras, can easily be coupled to this system while preserving the low-cost aspect. Due to the free-standing optics, the opto-mechanical changes are minimal, as only a beamsplitter and the second camera have to be added. It was possible to obtain usable biplane data with good SNR since the sensitivity of the industry-grade camera was well suited for capturing a sufficient number of photons.

In conclusion, successful live-cell SOFI imaging can be performed with an extremely cost-effective camera. This allows other researchers to implement SOFI imaging rather easily in Biology and Bio-Medical departments, by either attaching such a camera to an existing research microscope or by building a simple and robust system from readily available parts. Certainly this becomes more or more a viable research tool option with the amount of open-source / open-access software and hardware blueprints being made available to the scientific community.

# 5. DMD-based SIM visualizes live cell dynamics and reveals morphology of microgels

This chapter is based in major parts on the published preprint

Alice Sandmeyer*, Mario Lachetta*, Hauke Sandmeyer, Wolfgang Hübner, Thomas Huser, Marcel Müller. DMD-based super-resolution structured illumination microscopy visualizes live cell dynamics at high speed and low cost. *bioRxiv*, 2019.

Section 5.5 gives an outlook to the submitted manuscript

Pia Otto*, Stephan Bergmann*, Alice Sandmeyer, Maxim Dirksen, Oliver Wrede, Thomas Hellweg, Thomas Huser. Resolving the internal morphology of core-shell microgels with super-resolution fluorescence microscopy. *Nanoscale Advances*, submitted, 2019.
(*equal contribution)

Structured illumination microscopy (SIM) is a well-established super-resolution microscopy technique requiring minimal sample preparation and enabling the imaging of cells with approximately 100 nm spatial resolution. To acquire SIM data sets, samples are illuminated with a spatially varying, sinusoidal interference pattern that is precisely shifted and rotated. The generation of such suitable SIM patterns is typically established by employing spatial light modulators (SLMs). In this work, a digital micromirror device (DMD) was utilized for the pattern generation. However, due to the sawtooth arrangement of the micromirrors of the DMD, the blaze grating effect has to be taken into account. Here, the intensity distribution of the diffracted beams are highly dependent on the angle of the incoming light. For this study, the blazed grating effect was carefully studied by experiments and simulations. This was used as guidance to construct a compact, robust and cost-effective SIM microscope and demonstrate its capabilities in imaging fixed and live biological specimen with instant image reconstruction. Additionally, the internal morphology of microgels were revealed, so that the application range was extended towards chemical research.

## 5.1. Introduction

In the recent years, several so-called super-resolution methods were developed to circumvent the Abbe law which restricts the resolution of an optical system to about half the wavelength [2]. Structured illumination microscopy [13, 14, 130] (SIM) is an established technique for super-resolved imaging. Its particular strength is the capability to image at high frame rates and with low phototoxicity, which makes it a highly effective tool for live-cell imaging [1, 38, 222].

Ongoing research and modification of various SIM system resulted in different implementations of SIM that can extend an existing microscope. Opto-mechanic implementations use a diffraction grating that is either mechanically shifted and rotated [14] or steered by galvanometric mirrors to create interfering light beams, and thus the SIM pattern in the sample plane. These systems are complex to build, align and maintain, so with the advent of spatial light modulators, these devices were rapidly employed as electronically controlled gratings for SIM [135]. In contrast to the fixed mechanical grating, Ferro-electric light modulators (FLCOS devices) are a popular choice to construct especially fast SIM systems [25, 148, 150]. While these devices are successfully used by many groups, they are not without drawbacks. For example, their operating principle does not allow for the continuous display of a pattern, but requires constant switching between a positive and an inverted image. Also, currently only a single supplier offers a limited choice of FLCOS systems.

Digital micromirror devices (DMD) are also a promising option for structured illumination [149, 157, 223–227]. They are available in a variety of models, can provide even faster switching times than the FLCOS system, and can maintain a set pattern for extended duration without the need to switch or refresh the image. Additionally, they are slightly more cost-effective. Their working principle, however, leads to a different distribution of intensities in different diffraction orders when used in conjunction with a coherent laser light source. In detail, the surface of a DMD is formed by a lattice of micro-mechanically driven mirror elements. DMDs are binary in nature, where each element can independently be switched between two states, for example between tilt angles of +12° and -12°, respectively. Typically, these states are denoted as 'ON' and 'OFF', with those mirrors in the on-position reflecting light in a desired direction, and those in the off-position reflecting towards an absorbing element. In this way, DMDs are seen as amplitude-modulating devices, and for an incoherent illumination source [149], this yields a very effective model of the DMDs operation. However, when using a coherent laser light source an important aspect comes into play. Here, the sawtooth-like surface

formed by the tilted mirrors leads to a so-called *blazed grating*, which superimposes the regular SIM interference pattern generated by the pattern displayed by the device, with the underlying microscopic mirror structure [228, 229]. Thus, for coherent light, the device can be viewed as phase-modulating, because each point on the tilted mirror surfaces introduces a corresponding phase delay. Only if the blazed grating effect is modeled and properly taken into account, DMDs can be effectively employed for structured illumination microscopy.

In this work, the benefits of a DMD for SIM were explored by using it to create a rather compact (enabled by the small pixel size) and cost-effective (due to their low price point and overall advances in cost-effective microscopy) SIM system. In detail, the blazed grating was modeled, simulated and experimentally verified, even in conjunction with SIM patterns. This allows to employ DMD-devices effectively in coherent SIM applications. Lastly, the performance of such a system was employed for imaging fixed and live-cell imaging of biological samples and revealing the internal structure of microgels.

## 5.2. Analysis of blazed grating effect

### 5.2.1. Coherent illumination of DMDs

An optimal illumination pattern for SIM features high modulation contrast, which directly relates to the order strength $a_m$ (see eq. (2.33)) in the SIM reconstruction, and thus to the reconstruction quality [133, 144]. As the pattern is generated by interfering two beams of coherent light, these beams have to be of the same intensity and, ideally, the same polarization. Otherwise, the destructive interference is not complete and the modulation contrast is compromised.

This even intensity distribution is difficult to achieve with a DMD. The underlying mirror structure of the DMD results in a tilted reflection grating which leads to the previously mentioned blazed grating effect. Here, the positions of the non-zero diffraction orders relative to the main diffraction order depend on the angle of incidence, grating pitch and wavelength. The envelope of the diffraction pattern and its center also depend on the angle of incidence and tilt angle of the mirrors, whereas the positions of the minima are determined by the effective width of the mirrors and illumination wavelength. Thus, attempts to match one maximum diffraction order, or rather its position, with the envelope center of the overall intensity distribution are dependent on many parameters. In case a match is found, the so-called *blaze condition* is fulfilled and an even intensity distribution of the first diffraction

orders is established. If a DMD is used, most of the parameters (mirror dimension, tilt angle, etc.) are readily fixed by the device manufacturer, and therefore only the angle of incidence can be adjusted for any given wavelength to fulfill the blaze condition and to find the so-called *blaze angle* [230].

### 5.2.2. Effect of underlying blazed grating

First, the blazed grating effect of the DMD was investigated for the case where all mirrors are tilted in one direction and no SIM pattern is displayed by measuring the intensity pattern vs. the angle $\alpha$ of the incoming light beam (fig. 5.1). In order to easily reproduce the positioning of the angle of the incoming light, the laser is coupled into a high-power fiber and then collimated with a custom-made fiber collimator before illuminating the DMD (fig. 5.1a). Since the mirrors tilt along their diagonal axis, the DMD is also rotated by 45°. Thus, the tilt axis is perpendicular to the plane, which is formed by the incoming light and the diffracted light, so that the two-dimensional problem reduces to an one-dimensional problem. Now, the incoming light and the brightest diffraction order form a plane, which is parallel to the optical table, so that the subsequent alignment of the microscope system is simplified. A paper screen was used to identify the diffraction pattern and the angle $\beta$ of the maximum diffraction order of the reflected light, which is now referred to as main diffraction order. The intensity of the main diffraction order and the $\pm 1$ diffraction orders surrounding it, are measured with a conventional power meter (fig. 5.1b) to gain some initial insight into the intensity distribution of the envelope function of the diffraction pattern (i.e. its intensity distribution). Both possible flip directions of the mirrors were evaluated, the ON (+12°) and OFF (-12°) state and $\alpha$ from $\pm 17°$ to $\pm 30°$ was changed, respectively.

The measurement of the intensity in the main diffraction order revealed no dramatic difference between the lowest measured value and the highest one, which was about 13 % (ON) and 9 % (OFF) of the full laser power, respectively. Nevertheless, the intensity distribution in the first diffraction orders is highly dependent on the angle of incidence (fig. 5.1c and d). If the measured intensity of all first diffraction orders are as close to being equal as possible, the blaze condition was assumed to be fulfilled. In case of the OFF-state (fig. 5.1c) there was an area at roughly $\alpha = 24.5°$ $\pm 1°$ where the intensities were almost equal. However, if all mirrors were flipped to the ON-state (fig. 5.1d), the result was different from the one obtained for the OFF-state. In addition, it was more difficult to identify the blaze angle because the area where all first diffraction orders had the same intensity was significantly broadened compared to the OFF-state. The absolute value of the diffraction angle

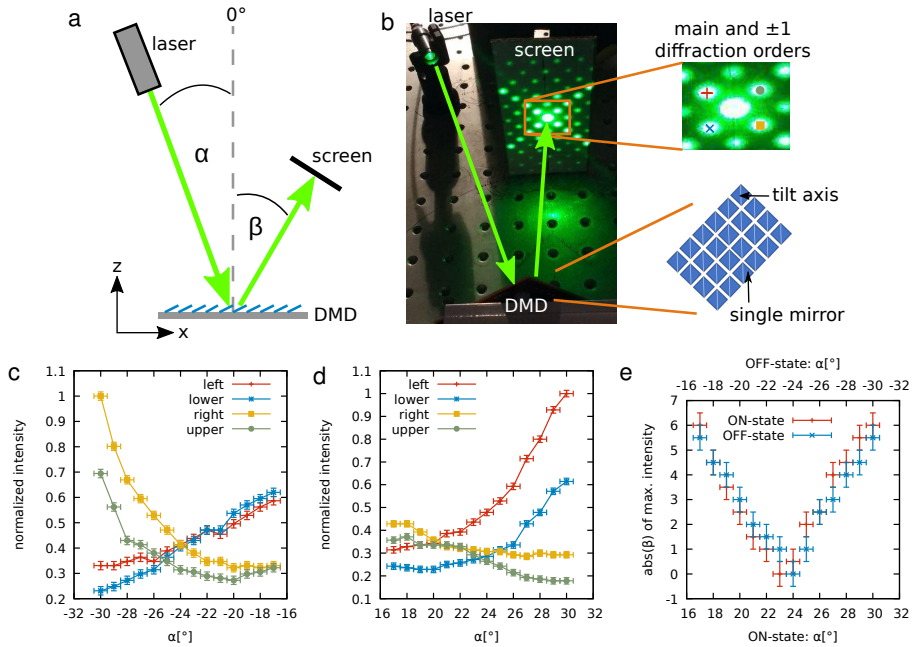


**Figure 5.1.:** Evaluation of the blazed grating effect underlying a DMD. (a) Schematic drawing of the experiment. All mirrors of the DMD are tilted in one direction, where a tilt angle of +12° represents the ON position and a tilt angle of -12° represents the OFF position. $\alpha$ is the incident angle, whereas $\beta$ is the diffraction angle of the main diffraction order. (b) Photograph of the experiment in the laboratory. Here, the entire DMD is rotated by 45°, so that the diffraction pattern is also rotated. The ±1 diffraction orders of the underlying structure are labeled with symbols and colors which are also represented in (c) and (d). Normalized intensity measured at the ±1 diffraction orders if all mirrors are switched to the OFF-state (c) or ON-state (d). (e) Absolute value of the diffraction angle $\beta$ of the main diffraction order depending on the angle of incidence $\alpha$.

of the main diffraction order $\beta$ also revealed no symmetric behavior in the ON- and OFF-states (fig. 5.1e). Neither the offset nor the slope were equal. Thus, the tilt angle is possibly not +12° (ON) and -12° (OFF). According to the manufacturer's data sheet of the DMD, the tilt angle error is precise to within ±1°, and therefore, a symmetric result cannot necessarily be expected.

Nonetheless, the OFF-state appeared to be more promising for SIM because based on the results above it will be easier to identify proper values for the blaze angle using this mirror position. This observation does, however, only concern the blazed grating effect of the underlying structure. Further measurements with the SIM pattern on the DMD are more complex if the same range of angles $\alpha$ is used. This will allow the use of the results of the underlying structure as start parameters for the search of the blaze angle. To obtain the exact values and then confirm these results, more calculations and simulations were needed as detailed below.

### 5.2.3. Simulation of the blazed grating effect

The DMD was modeled and simulated to better understand the results obtained by the measurements. For this, the diffraction pattern depending on the angle of incidence $\alpha$ was closer investigated [231]. To accomplish this, the DMD needed to be described mathematically, and the electric field reflected from its surface had to be calculated for different positions and states of the mirrors. Finally, the blaze angle had to be determined for the case, where a SIM grating pattern is displayed on the DMD.

Since the DMD is basically a two dimensional array of single mirrors, a single mirror was first modeled using a suitable coordinate system (fig. 5.2a). It was assumed that each non-tilted mirror is in the $xy$-plane of a Cartesian coordinate system. A point on a single mirror $\vec{c}$ is introduced by

$$\vec{c}(s,t) = (s,t,0) \quad \text{with} \quad 0 \leq s \leq w, 0 \leq t \leq w \tag{5.1}$$

where $w$ is the width of one mirror, $s$ and $t$ are the points in $x$- and $y$-direction, respectively. Now, the mirror was rotated along its diagonal axis $\vec{n} = 2^{-0.5}\,(1,1,0)$ with the rotation matrix

$$R_n(\gamma) = \begin{pmatrix} n_x^2(1-\cos\gamma)+\cos\gamma & n_x n_y(1-\cos\gamma)+n_z\sin\gamma & n_x n_z(1-\cos\gamma)-n_y\sin\gamma \\ n_x n_y(1-\cos\gamma)-n_z\sin\gamma & n_y^2(1-\cos\gamma)+\cos\gamma & n_y n_z(1-\cos\gamma)+n_x\sin\gamma \\ n_x n_z(1-\cos\gamma)+n_y\sin\gamma & n_y n_z(1-\cos\gamma)-n_x\sin\gamma & n_z^2(1-\cos\gamma)+\cos\gamma \end{pmatrix} \tag{5.2}$$

where $\gamma$ is the tilt angle along the diagonal. To describe a point $\vec{d}$ on the surface of the DMD, each mirror had to be addressed by introducing the grid $\vec{m} = m(m_x, m_y, 0)$, where $m_x \in \mathbb{N}_0$ and $m_y \in \mathbb{N}_0$, and the gap $g$ between the mirrors is considered in $m = w + g$. With eq. (5.1) and eq. (5.2), the surface was now parameterized by rotating a single mirror and placing it to its position

$$\vec{d}\left(\gamma_{m_x,m_y}, s, t, m, m_x, m_y\right) = R_n\left(\gamma_{m_x,m_y}\right) \cdot (s, t, 0) + m(m_x, m_y, 0) \tag{5.3}$$

Here, $\gamma$ is now expressed as $\gamma_{m_x,m_y}$ to address each mirror. The resulting surface of the DMD can then be modulated and visualized with the tilt of the mirrors (fig. 5.2b).

Next, the diffracted intensity distribution $I$ needed to be calculated which is the square of the absolute value of the reflected electric field $E$. Since monochromatic and coherent light was used, the time-independent electric field can be described as

$$E = (E_0, \phi) = E_0 \cdot e^{i\phi} \quad \text{with} \quad E_0 = E_{0_{m_x,m_y}} \quad \text{and} \quad \phi = l \cdot \frac{2\pi}{\lambda} \tag{5.4}$$

where $E_0$ is the amplitude and $\phi$ the phase shift. The Gaussian beam profile of the laser beam is approximately constant for a single mirror, and therefore $E_0$ depending on $m_x$ and $m_y$ needed to be introduced. The phase shift $\phi$ is determined by the path length $l$ and the wavelength $\lambda$.

However, since the case of Fraunhofer diffraction was used for this simulation, the diffracted light spreads out in all three spatial dimensions in a spherical way (fig. 5.2e), so that it was more convenient to change the Cartesian coordinate system to one where the unit vector $\vec{v}(x, y, z)$ was then associated with $\vec{v}(\varphi, \vartheta)$ (fig. 5.2f). The propagation vectors of the incoming light $\vec{a}$ and the diffracted light $\vec{b}$ were normalized and can be described as follows

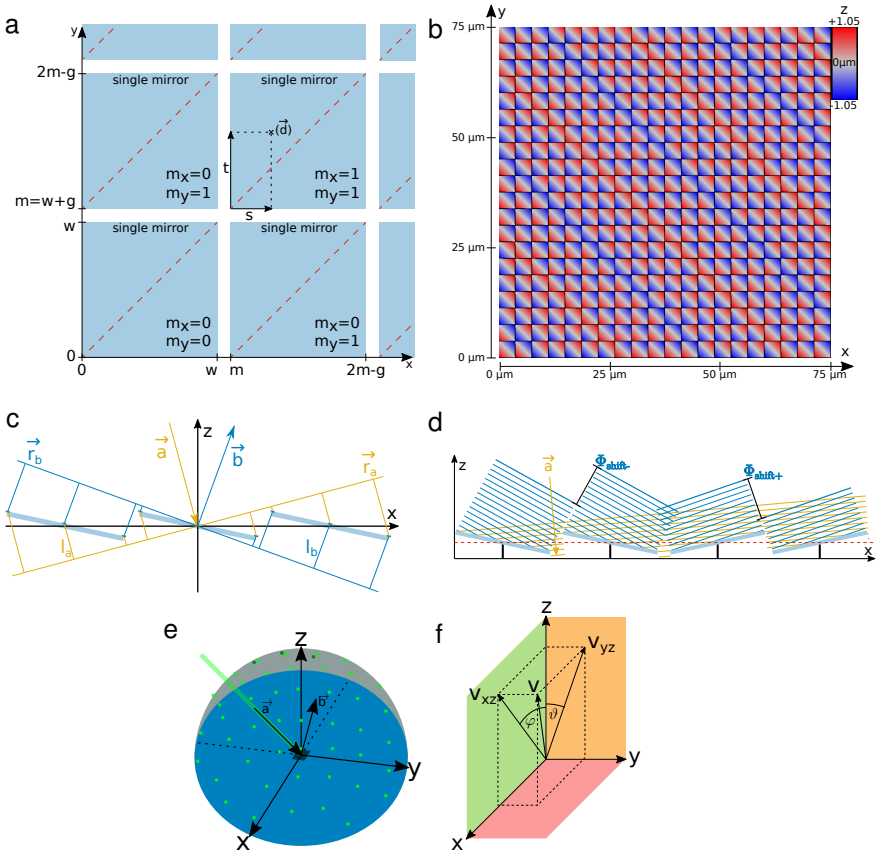


**Figure 5.2.:** Modeling (coherent) light propagation on a DMD surface. (a) Physical dimension and rotation axis of the micro-mirrors. (b) Resulting height profile of the DMD surface, which corresponds to phase delay. (c) Phase shift of different points in a planar wave-front, propagating towards the DMD in direction $\vec{a}$, or reflected from the DMD in direction $\vec{b}$, see eqs. (5.7) and (5.8). (d) Simplified modeling of light wave-fronts being reflected by the micro-mirrors, where a single, analytically known wave-front emanates from each mirror. This approach is correct in far-field / Frauenhofer approximation. (e) Visualization of light input and output vectors in the 3-dimensional space of the DMD. (f) Visualization of the tip/tilt angular coordinate system used to represent directionality of e.g. the directions $\vec{a}$ and $\vec{b}$.

$$\vec{a}\left(\varphi_a, \vartheta_a\right) = \begin{pmatrix} a_z \cdot \tan\left(\varphi_a\right) \\ a_z \cdot \tan\left(\vartheta_a\right) \\ a_z \end{pmatrix} \quad \text{with} \quad a_z = \sqrt{\frac{1}{\tan^2\left(\varphi_a\right) + \tan^2\left(\vartheta_a\right)}} \tag{5.5}$$

$$\vec{b}\left(\varphi_b, \vartheta_b\right) = \begin{pmatrix} b_z \cdot \tan\left(\varphi_b\right) \\ b_z \cdot \tan\left(\vartheta_b\right) \\ b_z \end{pmatrix} \quad \text{with} \quad b_z = \sqrt{\frac{1}{\tan^2\left(\varphi_b\right) + \tan^2\left(\vartheta_b\right)}} \tag{5.6}$$

The propagation vector of the electric field illuminating the DMD $\vec{a}$ is perpendicular to the wavefront plane $\vec{r_a}$, which is also true for the propagation vector of the diffracted electric field $\vec{b}$ and its wavefront plane $\vec{r_b}$ (fig. 5.2c). Now, the wavefront plane was set in the origin of the coordinate system, so that the Hesse normal form of the wavefront is

$$\vec{a} \cdot \vec{r_a} = 0 \qquad \text{and} \qquad \vec{b} \cdot \vec{r_b} = 0 \tag{5.7}$$

Due to the tilted mirrors, the planar wavefront, propagating along the direction $\vec{r_a}$, hits each point of the DMD with a different phase shift, which results in a different path length $l_a$. By calculating the distance of the fixed wavefront plane $\vec{r_a}$ to the DMD $\vec{d}$, $l_a$ was obtained, which can be seen as a distance from a point to a plane. Additionally, the diffracted light also contributes an extra path length $l_b$ (fig. 5.2c). Due to the mathematical determination of distance point-plane, $l_a$ and $l_b$ can be expressed as

$$l_a = \vec{d} \cdot \vec{a} \quad l_b = -\vec{d} \cdot \vec{b} \tag{5.8}$$

Thus, the total path length $l$ is the sum of $l_a$ and $l_b$, which can be inserted in eq. (5.4), and therefore the phase shift results to

$$\phi = \vec{d}\left(\vec{a} - \vec{b}\right) \frac{2\pi}{\lambda} \tag{5.9}$$

and an electric field of

$$\begin{aligned} E_{\text{one ray}}\left(\vec{a}, \vec{b}, \gamma, s, t, m, m_x, m_y, \lambda\right) = & E_{0_{m_x, m_y}} \cdot \exp\left(\frac{2\pi i}{\lambda}\right. \\ & \left. \cdot \vec{d}\left(\gamma_{m_x, m_y}, s, t, m, m_x, m_y\right) \cdot \left(\vec{a} - \vec{b}\right)\right) \end{aligned} \tag{5.10}$$

At this point, in this idealized model, the DMD acts almost purely as a phase modulator. For all wavefront components hitting a mirror, only the phase is affected by the tilt of these mirrors. The polarization of the light was not modified, while the amplitude is modulated in a binary fashion, with some components hitting the mirrors being unmodified, and some components missing a mirror element being absorbed entirely. Now, each point of a single mirror needs to be considered, so that an integration of $s$ and $t$ is necessary. Additionally, each mirror of the DMD contributes to the resulting electric field, so that a sum over each mirror was required. Thus, by modifying eq. (5.10), the equation results to

$$E_{\mathrm{DMD}} = \sum_{m_x=0,m_y=0}^{M_x,M_y} \int_0^w \int_0^w E_{0_{m_x,m_y}} \cdot \exp\left(\frac{2\pi i}{\lambda}\vec{d}\cdot\left(\vec{a}-\vec{b}\right)\right) dsdt \tag{5.11}$$

where $M_x$ and $M_y$ are the total numbers of mirrors in $x$- and $y$-direction, respectively.

However, several assumptions can be used to solve eq. (5.11). First, as already mentioned, $E_{0_{m_x,m_y}}$ was constant for a single mirror, and therefore it can be extracted from the integral $F$, which was defined as

$$F\left(\vec{a},\vec{b},\gamma_{m_x,m_y},w,m_x,m_y,\lambda\right) = \int_0^w \int_0^w \exp\left(\frac{2\pi i}{\lambda}\vec{d}\cdot\left(\vec{a}-\vec{b}\right)\right) dsdt \tag{5.12}$$

This integral can be solved analytically e.g. by using a computer algebra system. Nevertheless, eq. (5.12) can also be simplified to obtain more insight into the phase modulation effect. Each mirror tilts by either $-\gamma$ or $+\gamma$, which results in only two different phase shifts, namely $\phi_{shift-}$ and $\phi_{shift+}$ measured relative to a reference mirror (fig. 5.2d). Thus, only two integrals $F_+\left(\vec{a},\vec{b},+\gamma,w,0,0,\lambda\right)$ and $F_-\left(\vec{a},\vec{b},-\gamma,w,0,0,\lambda\right)$ needed to be calculated in the origin of the coordinate system and multiply a complex factor due to the mirror position which can be seen by inserting eq. (5.3) in eq. (5.12):

$$
\begin{aligned}
F_{\pm}(X) &= \int_0^w \int_0^w \exp\left(\frac{2\pi i}{\lambda}\left(R_n(\pm\gamma)\,\vec{c}(s,t) + \vec{m}(m_x, m_y)\right) \cdot \left(\vec{a} - \vec{b}\right)\right) dsdt \\
&= \underbrace{\int_0^w \int_0^w \exp\left(\frac{2\pi i}{\lambda} R_n \vec{c} \cdot \left(\vec{a} - \vec{b}\right)\right) dsdt}_{\text{phase shift of a single mirror at origin}} \cdot \underbrace{\exp\left(\frac{2\pi i}{\lambda}\vec{m} \cdot \left(\vec{a} - \vec{b}\right)\right)}_{\text{factor due to mirror position}} \\
&= F\left(\vec{a}, \vec{b}, \pm\gamma, w, 0, 0, \lambda\right) \cdot \exp\left(i \cdot \phi_{\text{position-shift}}(m_x, m_y)\right) \qquad (5.13)
\end{aligned}
$$

where $F_{\pm}(X)$ is dependent on $\vec{a}, \vec{b}, \pm\gamma, w, m_x, m_y$ and $\lambda$.

Finally, the intensity distribution can be calculated by inserting eq. (5.13) in eq. (5.11) and determining the square of the absolute value

$$
I\left(\vec{a}, \vec{b}, \pm\gamma_{m_x,m_y}\right) = \frac{c\epsilon_0}{2}\left|E\left(\vec{a}, \vec{b}, \pm\gamma_{m_x,m_y}\right)\right|^2 \qquad (5.14)
$$

with $c$ the speed of light and $\epsilon_0$ the vacuum permittivity.

However, eq. (5.14) gives several possibilities for different experimental realizations. $\pm\gamma_{m_x,m_y}$ allows to modulate the DMD in a large number of different configurations. The number of mirrors, the tilt angle and even displaying the SIM pattern can be defined, because each mirror is addressed individually. The incident angle, which is crucial for an even intensity pattern, can be chosen by setting $\vec{a}$ properly. Then, the space needs to be sampled by varying $\vec{b}$ to determine the intensity $I$ at each spatial point. A software package was created to numerically perform these calculations (appendix A.1.3).

In the first implementation of the simulation, a single mirror was modeled which was either tilted in the ON- or OFF-state and an angle of incidence of 0° was chosen (fig. 5.3a). The respective intensity patterns display the expected mirrored distribution. In both cases, the main diffraction maximum was clearly visible and the first diffraction orders were lying in the $x$- and $y$-direction. Therefore, only one state was further investigated.

In the next iteration of the simulation, a two-dimensional array of mirrors was modeled. Here, an array of $100 \times 100$ mirrors was chosen which were all positioned in the OFF-state (fig. 5.3b). Since the main diffraction order is much brighter than the first diffraction orders, a logarithmic scale was chosen to display the data, and thus, the maxima look like crosses rather than round spots (which is the typical result for linearly scaled axes). Nevertheless, a comparison to the experimental results indicated that these simulated results are, indeed, valid.

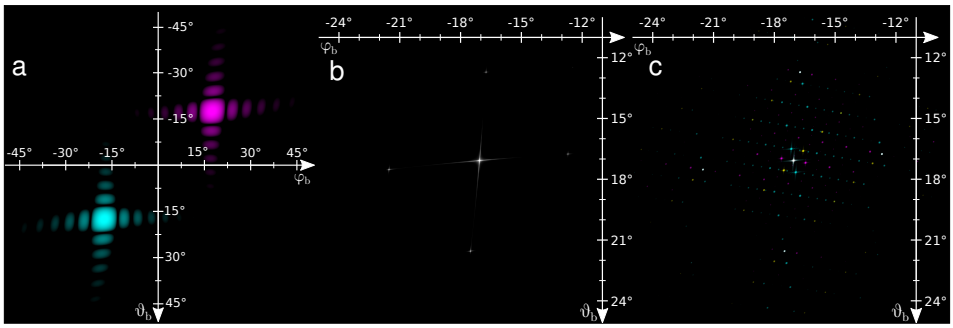


**Figure 5.3.:** Wave propagation and interference pattern simulation of a DMD surface. A fully coherent light source is simulated illuminating the DMD head-on (angle of incidence 0°) and with a Gaussian intensity profile. The diagrams show the reflected intensity plotted against the output angle (fig. 5.2), on a logarithmic scale. (a) Diffraction pattern of a (hypothetical) single mirror, in its two possible tilt states ("teal" is OFF and "magenta" is ON). (b) Diffraction pattern of the DMD surface when all micromirrors are oriented into the same OFF position. (c) DMD displaying a typical SIM pattern, while illuminated with coherent light. The full diffraction pattern arises from the inert diffraction properties of the DMD (mechanical mirror size and tilt) with the pixelated and binary SIM pattern superimposed. The underlying structure of the mirrors is the OFF position. The three colors indicate a different SIM pattern for each typical angle used for SIM.

Next, the case was modeled where a typical SIM grating pattern is displayed on the simulated DMD with the OFF-state as underlying structure (fig. 5.3c). In addition, the SIM grating pattern was rotated by two further angles (approx. 60°), so that the typical three angles were obtained that are used for space-filling 2D and 3D SIM. The result, as shown in fig. 5.3c, indicated that the diffraction orders of the underlying structure were, indeed, modulated and further diffraction maxima were obtained. Also, as can be seen in fig. 5.3c, the diffraction orders of the underlying structure stay at their original position, although a different pattern was being displayed on the DMD.

So far, the SIM pattern in the Fourier plane can be simulated if a DMD is used as the primary device to create interference patterns and the simulation results match with the experimental measurements. Next, all possible illumination conditions and their resulting blaze angles need to be identified in order to guide the experimental implementation. Therefore, the model was used to vary between a range of angles of incidence $\varphi_a$ and $\vartheta_a$ and to calculate the resulting intensity patterns. To determine the best candidates for the blaze angle, a comparison of the intensity of the first diffraction orders was chosen as this parameter indicated that it produces sufficiently close results (fig. 5.4a-c). If the intensities of the first diffraction orders are equal, it indicates that the blaze angle was found. This parameter is, however, specific for one SIM pattern angle but will likely be different for other pattern angles as can be seen in fig. 5.3c. This behavior can be contributed to the fact that the diffracted intensity pattern of a single mirror is the envelope function of the overall diffraction pattern (fig. 5.4a). Thus, it is necessary to match the maximum of the envelope function with the maximum of the main diffraction orders of the SIM pattern in order to obtain an even intensity distribution in all first diffraction orders that are used to create SIM patterns for all SIM pattern angles. To match the results, the distance between the maximum values was calculated. Since this process needs to be repeated for thousands of data sets running through all possible variations of angles, the simulation was implemented on a graphics card to accelerate the calculations. The result is shown in fig. 5.4d and it implies that there are a large number of potential blaze angles according to the dark rings in the figure, which indicate a good match.

To better correlate these results with the experiments, where the entire simulated DMD structure was rotated by 45°, such that now only the cross-line, where $\varphi_a = -\vartheta_a$, is of interest. Additionally, the results shown in fig. 5.1c and fig. 5.1d imply the use of the OFF-state as the underlying structure, and therefore this was also used for the simulations. Angle calculations due to different coordinate systems

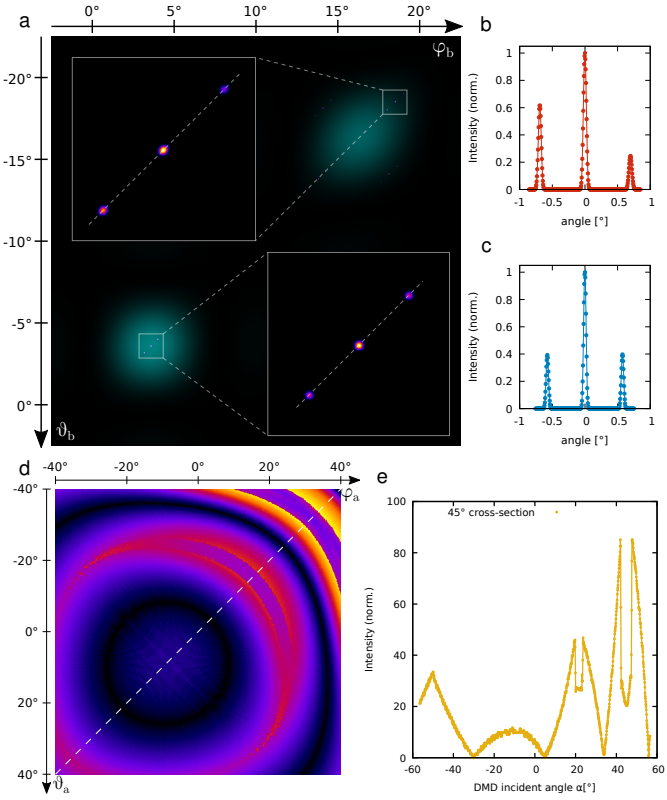


**Figure 5.4.:** Simulations of DMD wave propagation for optimized use with SIM. For all panels the OFF-state is the underlying structure. (a) Alignments of the SIM pattern (magenta/blue/white) to the diffraction envelope (teal) caused by a single mirror in the OFF-state (fig. 5.3a). In the top row, the main diffraction order of the SIM pattern does not coalign with the envelope, with yields an uneven intensity distribution in the $\pm 1$ side orders that create the SIM pattern (b). In the bottom row, the main SIM diffraction order coaligns with the envelop, with yields an even intensity distribution into the $\pm 1$ side orders (c). Axis are centered on the main SIM diffraction order and scaled in small angle approximation (b and c). Misalignment between main SIM diffraction order and maximum of the envelop, depending on the input angles (d) and along a 45° cross-section (dotted line, plot in panel e). Alignments close to zero yield equal intensities in the SIM side orders. The 45° line was chosen as it allows for an easy alignment of all angles in one plane (DMD mounted to a table).

were needed to allow for a proper comparison to the experimental results. At the 45° cross-section, $\alpha$ is determined by

$$\alpha = \arctan\left(\sqrt{2} \cdot \tan\left(\varphi_a\right)\right) \tag{5.15}$$

From fig. 5.4e it is apparent that minima at $y = 0$ occur at several points which indicate the spots where the blaze condition is fulfilled. For the DMD used in the experiments, the blaze angle was found at $\alpha$ = -27.9° (fig. 5.4e). As a control, a line plot across the main and first diffraction orders was analyzed to underline the result (fig. 5.4c). Also, in fig. 5.4a it can be seen that the center of the overall mirror envelope is an excellent match with the main diffraction order. To demonstrate a non-matching case, an incident angle of $\alpha$ = -53° was chosen and the difference in the first diffraction orders is clearly visible from fig. 5.4b.

### 5.2.4. Comparison of simulations and experimental results

The predictions made by the simulated DMD data, where an actual SIM pattern was modeled, had to be verified with experimental data. To facilitate this, the experimentally obtained intensity pattern diffracted by the DMD was projected onto a camera chip using a single lens. This arrangement guaranteed that the Fraunhofer diffraction condition was also fulfilled in the experimental case. The camera was positioned in the Fourier plane of the setup. In addition, the power of the laser beam used to illuminate the DMD had to be reduced by neutral density filters to avoid saturating the camera pixels. For the measurements all nine SIM patterns (three illumination angle and three associated phase shifts) were displayed by the DMD with a display time of 105 $\mu$s for each single frame. The exposure time of the camera was set to 5 ms. To find the blaze angle the incident angle $\alpha$ was set to -24° for the OFF case and to +25° for the ON case according to the results of fig. 5.1c and fig. 5.1d. To cover a wide range of angles $\alpha$ the DMD was gently tilted by ±0.5° and ±0.3° along the $x$- and $y$-direction between measurements using micrometer screws, respectively. This also allows to evaluate how critical the precise alignment of the blaze angle was in order to obtain the highest possible SIM modulation contrast.

First, the distribution of the diffraction orders in fig. 5.5a (ON) and b (OFF) were compared. As expected, the distribution in both cases was very similar, but it looked different when compared to the results obtained by the simulation (fig. 5.3c and fig. 5.6f). The characteristic cross shape from the simulations is not visible, instead a diagonal line can be seen. This is probably caused by two factors: First,

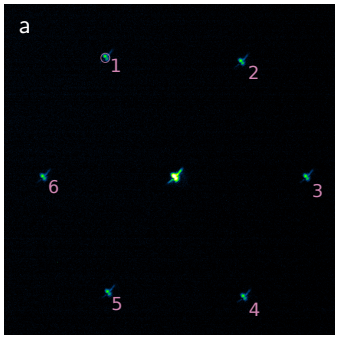


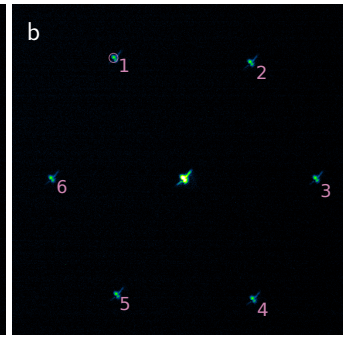


c

**Measured intensities**

| side order | normalized intensity | |
|---|---|---|
| | on | off |
| 1 | 0.88 | 0.94 |
| 2 | 0.87 | 0.99 |
| 3 | 0.93 | 1.00 |
| 4 | 0.92 | 0.91 |
| 5 | 0.98 | 0.94 |
| 6 | 1.00 | 0.99 |

**Figure 5.5.:** Measured diffraction intensity pattern in the Fourier plane with the SIM pattern displayed on the DMD. With a lens the intensity pattern was focused on a camera chip. In both cases (a-ON and b-OFF, exposure time 5 ms, DMD display time 105 $\mu$s) the measured blaze angle was chosen as the incident angle, which was +25.3° for ON and -23.9° for OFF. The difference compared to the simulated data is due to a different tilt angle $\gamma$. For a better visualization a log scale was set. The mean value of the circled area in (a,b) was analyzed to evaluate the quality of the found blazed angle (c).

the physical DMD microstructure might deviated from the ideal structure that was used in the simulations. Also, the DMD chip is covered by a protective glass plate, which was not taken into account in the simulations. Indeed, if a different spot of the DMD was illuminated, the diagonal line also moved. This leaded to the assumption that the glass cover caused a change in the light path and accordingly changed the distribution of the diffraction orders. Additional analyses, such as varying the beam diameter and inserting a Fourier mask, showed that the spots then changed to a spherical shape. This was an acceptable solution since in most SIM setups a Fourier mask is used to reject other diffraction orders, anyways.

The blaze angles for the DMD were experimentally found to be $\alpha = +25.3°$ in the ON case and $\alpha = -23.9°$ in the OFF case (fig. 5.5a and b). Since a high modulation depth is desired for best SIM performance, the intensity of the first diffraction orders belonging to the same SIM angle is supposed to be equal. The mean intensity values of the first diffraction orders were measured by choosing a region of interest (ROI) across each spot and evaluated their brightness (fig. 5.5c). For a fair comparison, only the intensities of the same SIM angles need to be compared, namely 1 and 4, 2 and 5, 3 and 6. The maximum difference was found to be 11 % (ON) and 5 % (OFF) for these spots - which remains very similar if the DMD is tilted in $x$- and $y$-direction by $\pm 0.5°$ and $\pm 0.3°$. Nevertheless, the absolute values of the experimentally found blaze angels were not the same as those obtained by the simulation. One has to keep in mind, though, that the simulated results were obtained using a fixed tilt angle of $\gamma = -12°$. According to the manufacturer, however, $\gamma$ varies from -11° to -13° in the OFF case. Therefore, the impact of different $\gamma$ values on the blaze angle needs to also be investigated.

In order to analyze the dependence of the blaze angle on the tilt angle $\gamma$ of the underlying structure, various cases of $\gamma$ were chosen for the simulations. Again, the distance of the envelope of one diffracting mirror to the main diffraction order (as shown in fig. 5.4d) was determined for different angles of incidence to evaluate the blaze angle. As can be seen from fig. 5.6a to fig. 5.6d, a small change of the tilt angle leads to rather significant changes in the graphs, resulting in very significant shifts of the blaze angle. Again, only the OFF case as underlying structure was simulated and shown due to the fact that the ON case should be a mirror image of this case. The dark rings which indicate solutions for the blaze condition have very different diameters. As seen previously in fig. 5.3d with $\gamma = -12°$, there were two solutions rings. If the tilt angle decreased to $\gamma = -11°$, the diameter of the two dark circles also decreased and the inner circle even disappeared entirely (fig. 5.6a). An increase of $\gamma$ to -13° leaded to large diameters of the dark rings (fig. 5.6c). Since the

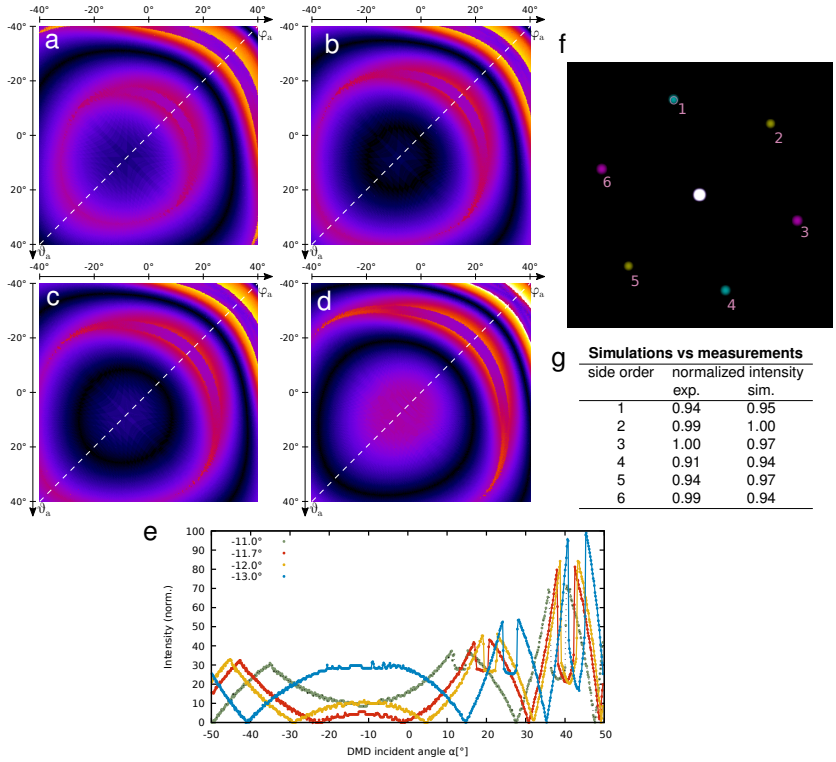


**Simulations vs measurements**

| side order | normalized intensity exp. | sim. |
|---|---|---|
| 1 | 0.94 | 0.95 |
| 2 | 0.99 | 1.00 |
| 3 | 1.00 | 0.97 |
| 4 | 0.91 | 0.94 |
| 5 | 0.94 | 0.97 |
| 6 | 0.99 | 0.94 |

**Figure 5.6.:** Evaluation of the dependence of the blaze angle on the tilt angle $\gamma$ of the DMD mirrors. Misalignment between main SIM diffraction order and maximum of envelope depending on $\gamma$ (a: -11°, b: -11.7°, c: -12°, d: -13°). In each simulated figure the incident angle was changed in order to find the blaze angle. Again, a cross-section at 45° was chosen to compare the simulations results (e) to the experimental data. The blaze condition at $y = 0$, where the plotlines come down to the x-axis, shifts clearly due to small changes of $\gamma$. For a direct comparison to the experimental results ($\alpha$ = -23.9°, $\gamma$ = -11.7°), the same case was simulated (f). Again, a log scale was set for a better visualization. Same colors of the first orders belong to the same SIM angle. The mean of the side orders in the displayed ROI is listed and directly compared to the experimental data of fig. 5.5c (g).

$\gamma$-range extends from -11° to -13°, and the position of the blaze condition shifted accordingly, a potential maximum value for the blaze angle can be determined. To find this value, the cross-section along the 45° axis, where $\varphi_a = -\vartheta_a$, was plotted for the different cases of $\gamma$ (fig. 5.6e). According to the simulation results a fairly wide range of values for the blaze angle is covered. For example, if $\gamma$ = -13°, one possible corresponding blaze angle is $\alpha$ = -41°.

Based on the simulations, a tilt angle of $\gamma$ = -11.7° was found for the underlying structure, leading to a blaze angle of $\alpha$ = -23.9° for the OFF case (fig. 5.6e). This matches perfectly with the experimentally measured blaze angle and the possible $\gamma$-range according to the manufacturer. Also, the experimentally measured blaze angle for the ON case, $\alpha$ = +25.3°, was consistent with the simulations, since a potentially wide range of blaze angles was covered due to the range of possible $\gamma$ values. To further support the results, the simulated diffraction pattern is shown if the tilt angle $\gamma$ were -11.7° and the angle of incidence $\alpha$ = -23.9° was the same as the experimentally measured blaze angle for the OFF case (fig. 5.6f). Again, as in fig. 5.5, basically the same ROIs covering the first diffraction orders were chosen and their mean values evaluated. A direct comparison shows that the simulated results are consistent with the experimental results (fig. 5.6g).

## 5.3. Construction of a compact and cost-efficient SIM system

Now, since the correct blaze angle was determined and measured, constructing the remaining components of the DMD-SIM microscope was straightforward. Compared to other SLM-based SIM microscopes, using a DMD is more cost-efficient and allows for a compact design due to the small pixel size of the DMD mirrors. This made it possible to construct a SIM microscope with a rather small footprint, which could be placed on a 40 cm x 90 cm optical bread board (fig. 5.7a). In addition, the laser and the camera were exchanged from scientific-grade to industry-grade components (table A.3). The laser is typically employed for light show applications and the industry-grade CMOS camera was already tested for other implementations of super-resolution microscopy such as dSTORM and SOFI, where its use had lead to sufficient results as long as the sample brightness does not require single photon counting [18, 232] (see chapters 3 and 4). Overall, the use of these components permits to keep the total cost of the system below 20 k€ which is more than ten times less expensive than commercial solutions and suits very well with the aim of this work.

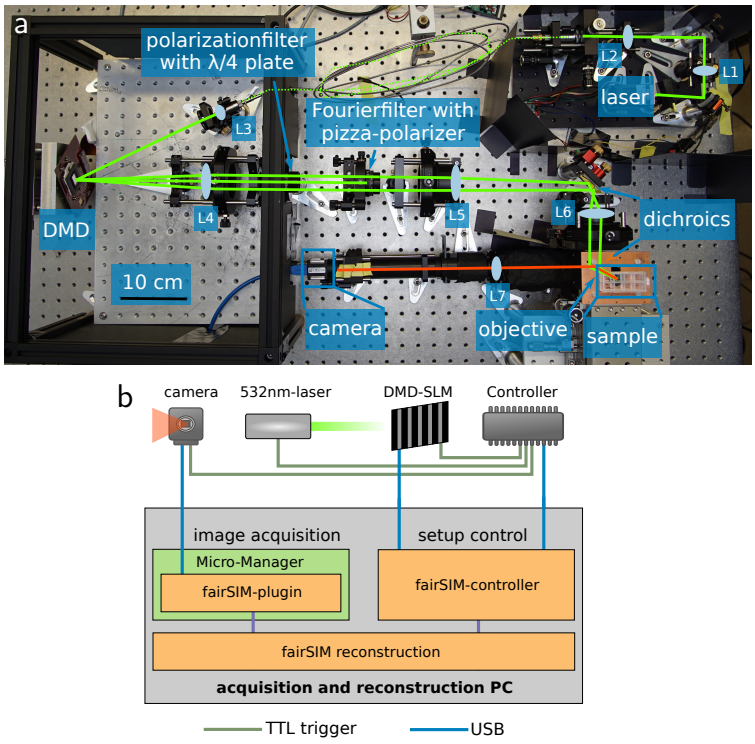


**Figure 5.7.:** Photograph of the custom-made SIM microscope and schematics of its data stream. (a) A 532 nm laser beam (green) is coupled into a fiber before illuminating the DMD at the blaze angle. Polarization optics were required to achieve the same linear polarization in the corresponding SIM angles. Two dichroic mirrors from the same batch were used to maintain the polarization state and to separate the excitation light from the fluorescence (red) signal. The same objective lens was used to excite the sample and to collect the fluorescence signal which was detected with an industry-grade CMOS camera. (b) Timing control and image data flow. Binary SIM pattern were stored on-board the DMD and selected in sequence by sending TTL trigger pulses to the DMD control board. The DMD, camera and laser light source were synchronized using a micro-controller. The raw image data is fed into a GPU-based real-time data processing system [25]. A detailed description of the used components can be found in table A.3.

The 532 nm diode laser is expanded ($f$(L1) = 30 mm, and $f$(L2) = 150 mm) and then coupled into a high-power fiber via a 10x objective. Thus, the beam profile is cleaned up and an easier adjustment of the illumination blaze angle was enabled. The laser power level cannot be controlled electronically, and therefore two neutral density filters (10 % and/or 50 %) were utilized if the laser power needed to be adjusted. With a customized collimator ($f$(L3) = 20 mm) the laser beam is paralleled and directed to the DMD with the blazed angle as the incident angle. The DMD itself was also mounted on a customized holder with a tilt of 45°. The holder can shift the DMD in $x$- and $y$-direction and adjust the tilt along the $xz$- and $yz$-plane. The grating patterns displayed on the DMD were calculated via a (modified) search algorithm used to find suitable binary gratings [25, 148, 233]. 8 % of the laser power incident on the DMD were ultimately maintained in the two corresponding SIM beams.

The L4 lens ($f$ = 200 mm) collects the diffracted light and a combination of polarization filter and $\lambda/4$ plate converts the elliptic polarized light to circular polarized light. In the Fourier plane of L4, only the first side orders of the main diffracted orders pass the Fourier filter. Directly afterwards these beams were linearly polarized by a "pizza"-polarizer, so that the side orders of the same SIM angle have the same linear polarization. To obtain the best possible modulation depth for SIM illumination, the relative polarization of the excitation beams is a critical factor. Ideally, the two corresponding beams have the same linear polarization [152, 153]. Therefore, several components to control the polarization of the excitation beams were utilized in the setup. A L5 lens ($f$ = 100 mm) collects the beams and the first dichroic mirror reflects them to L6 ($f$ = 150 mm) which is focusing the light in the back-focal plane of the objective. A dichroic mirror from the same batch as the first one, reflects the laser beam to the immersion oil objective which focuses the SIM beams in the sample. Using a perpendicular arrangement of two dichroic mirrors from the same batch, the polarization adjustment is maintained [150].

For the data acquisition the Zeiss 1.518 oil is used and a $xyz$-block is used for the focusing and maneuvering of the sample. The same objective collects the fluorescence signal, which then passes the second dichroic mirror and is reflected in direction to the camera. A detection filter is implemented to block unwanted laser light. Either an orange detection filter is used or a red detection filter, suitable to the used dye. The lens L7 ($f$ = 250 mm) is employed to focus the fluorescence emission on the camera. System synchronization, data acquisition and real-time SIM image processing is achieved through the fairSIM-VIGOR engine [25] and the $\mu$Manager software package [191, 192].

Acquiring SIM images with high frame rates requires precise timing between the DMD, the laser light source and the camera. The DMD control board allowed to upload predefined sequences of pattern, which were displayed with either fixed timing or in reaction to external trigger inputs. The camera equally allowed for external triggering of the start of an image exposure, and the laser light source can be switched at high speeds. An inexpensive micro-controller was used as a master clock device to generate these timing pulses.

The raw images acquired by the camera were fed into a real-time processing pipeline (called fairSIM-VIGOR) [25]. Compared to its original implementation, this microscope only needed to process a single color channel with reduced frame rate, so a single computer equipped with a graphics processing unit (GPU) suffices to handle data acquisition, processing and storage. Due to the real-time processing of the image data, the user obtains immediate feedback in super-resolved images and can directly evaluate the usability of the data during the experiment.

To test the functionality of the DMD-SIM setup, TetraSpeck beads (TS) with a diameter of 200 nm were imaged and then reconstructed with fairSIM [25, 138]. For the reconstruction a calculated optical transfer function (OTF) was used and OTF attenuation to suppress out-of-focus fluorescence signals [234, 235]. Besides the summed up wide-field image (WF), a filtered wide field image (fWF) was generated by applying the generalized Wiener filter step inherent to SIM reconstructions also to the WF data. This is important for a fair visual comparison, as the fWF image provides better contrast, but only the SIM image can truly reveal more details and separate individual beads (fig. 5.8a-c).

The SIM reconstruction process also allows to estimate the pattern modulation depth achieved by the instrument. Here, this estimate yields 0.75, 0.79 and 0.74 for the respective SIM angles, which are reasonable values for a well-aligned 2D SIM system. To further quantify the system performance, the lateral resolution gain was determined. To this end, 100 nm TS beads were imaged in order to apply a Fourier Ring Correlation (FRC) analysis [46, 221]. In brief, FRC takes two measurement of the same structure, but with independent noise contribution, as input. It then computes the correlation of those measurements at different spatial frequencies, assuming no directionality (hence averaging over 'rings'). The resulting graph can be interpreted as the available signal level of the imaging method at any given spatial frequency, and thus yields a model-free indicator of resolution. By applying this method to the DMD-SIM microscope data, a steep, expected drop-off was found in both the WF and the SIM data sets towards their respective resolution limits. By fitting these drop-offs (fig. 5.8d), the FRC curve for SIM images dropped off at

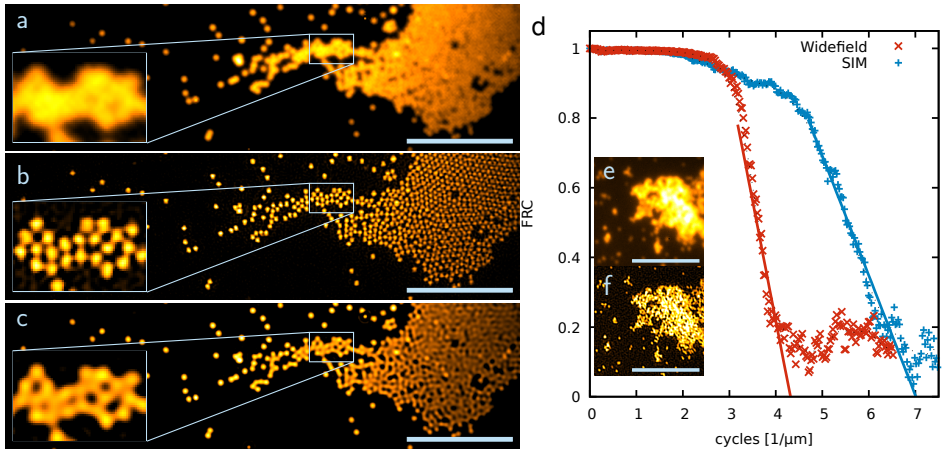


**Figure 5.8.:** Fluorescence images of 200 nm TS beads (a-c) and FRC statistics (d). (a) Summed up wide-field image of the recorded nine SIM frames and filtered wide-field image (c) determined by Wiener filtering. (b) Reconstructed SIM image of the 200 nm TS beads by fairSIM [138]. The inset clearly shows that single beads can be distinguished through SIM (scale bar 5 $\mu$m, inset 2.1 $\mu$m x 1.4 $\mu$m, exposure time per raw frame 20 ms). Quantification of the resolution enhancement via FRC analysis on 100 nm beads (see inset e-WF, f-SIM), which are approximate point sources better than 200 nm beads (scale bar 5 $\mu$m, exposure time per raw frame 50 ms). Two successive SIM imaged were acquired, reconstructed and analyzed via [46, 50]. The resulting graph (d) for both wide-field and SIM can be interpreted as the available signal ($y$-axis) at any given structure size (x-axis). By fitting both WF and SIM, a shift of 1.62× is found, which corresponds well with the expected resolution enhancement of 1.75×.

1.62× higher spatial frequency than the WF signal. The SIM pattern in use was set to approximately 280 nm line spacing, with should yield an approximately 1.75× resolution improvement at perfect SNR. However, the high frequency component accessible through SIM was dampened by the not fully modulated SIM pattern. Thus, the estimated modulation depths, the experimentally determined resolution calculated from FRC, and the theoretically expected resolution calculated from the SIM pattern spacing and optical parameters were fully consistent.

## 5.4. SIM images of biological samples

To further demonstrate the full functionality of the DMD-SIM microscope, the imaging quality was fist tested on fixed cells stained with different fluorescent dyes. Subsequently, various intracellular organelles labeled by fluorescent proteins were used to demonstrate that different structures can be resolved in vitro with the SIM microscope. Lastly, to further ensure that this system proves useful in a biological laboratory setting, its live-cell imaging compatibility was checked.

### 5.4.1. Resolving subdiffraction sized structures in fixed cells

As an initial sample, fixed U2OS cells embedded in glycerol were used, where their actin cytoskeleton was stained with Phalloidin Atto532. These filaments are perfect organelles to demonstrate the resolution enhancement (fig. 5.9). In the WF images close by single filaments cannot be resolved and appear as a single line. When switching to SIM mode, however, it becomes quite apparent that these are composed of more than one filament. These data also show that the instrument achieves an even illumination distribution over a large field of view. Therefore, extended structures with subdiffraction details in more than one cell can potentially be observed and analyzed.

Next, the actin cytoskeleton of fixed HEK293T cells were stained with the red fluorescent protein mScarlet by gene transfection (fig. 5.10a and b). A direct comparison between fig. 5.9 and fig. 5.10 is not particularly suitable because the cell lines are different and mScarlet attaches to a different domain of the actin cytoskeleton than Phalloidin. Nonetheless, it was of interest to demonstrate SIM with mScarlet since fluorescent proteins are not as photostable as organic fluorescent dyes. Although a 532 nm laser is not the best choice for the excitation of mScarlett, the DMD-SIM microscope proved to have sufficient sensitivity to resolve the actin filaments which appeared as single structures in the WF image.

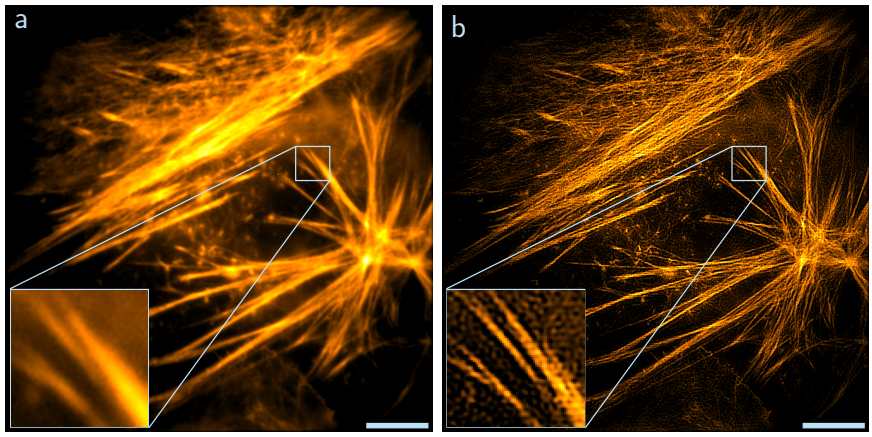


**Figure 5.9.:** Fixed U2OS cell labeled with Phalloidin Atto532, WF (a) and SIM (b) image (exposure time per raw frame 20 ms). The size of the images is 36 $\mu$m x 36 $\mu$m which is also the possible field of view with the microscope. The actin filaments are now distinguishable in the SIM image. Scale bar 5 $\mu$m, inset 2.8 $\mu$m x 2.8 $\mu$m.

Furthermore, the outer membrane of lysosomes in HEK293T cells were labeled with mScarlet and subsequently the cells were fixed. This organelle is of interest because it has a spherical shape and is present in a range of different diameters, from 100 nm to 1 $\mu$m. Such spherical structures serve as a good quality check for SIM microscopes. If the resolution enhancement should be irregular in some directions, the organelle would appear elliptical rather than spherical. In addition, some lysosomes can be resolved via WF imaging but the smallest ones cannot. The DMD-SIM microscope can resolve small spherical lysosomes (fig. 5.10c-g). In case the lysosomes had a larger diameter than 250 nm, WF imaging was sufficient to resolve the outer membrane structure (fig. 5.10c and f). To underline this statement, fWF was applied to increase the contrast, and this clearly shows that WF resolution is sufficient to resolve these organelles (fig. 5.10d and f). For structures with a diameter well below the diffraction limit, however, SIM was required and lysosomes with a diameter of 180 nm can be resolved which were not visible in WF (fig. 5.10e and g).

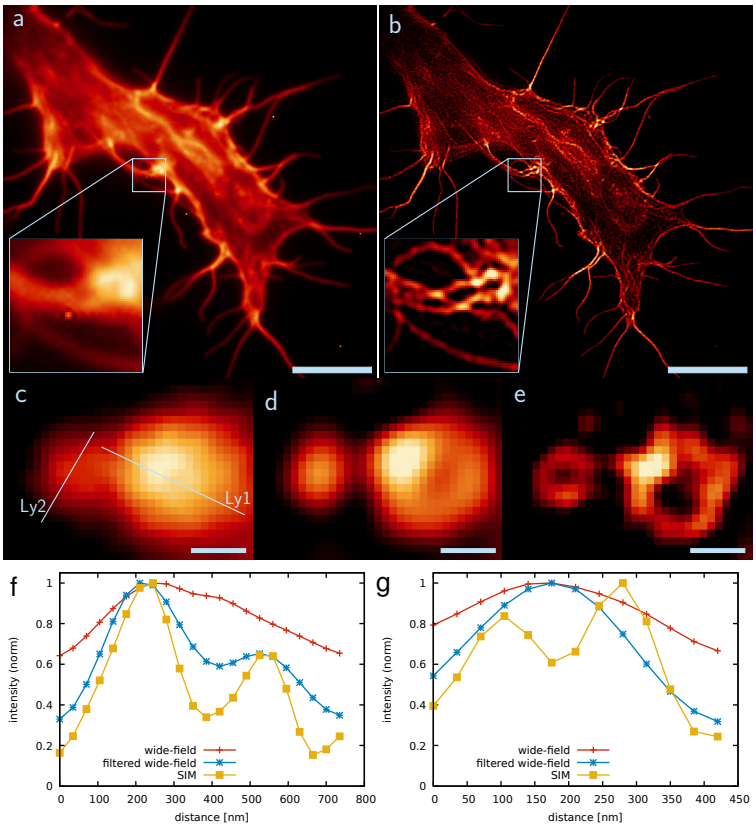


**Figure 5.10.:** Fixed HEK293T cells transfected with the fluorescent protein mScarlet, to either label actin (a,b) or lysosomes (c-e). Actin filaments that are very close to each other cannot be distinguished in the WF image (a), but the SIM image reveals that more than one filament is present (b). Scale bar 5 $\mu$m, inset 2.1 $\mu$m x 2.1 $\mu$m, exposure time per raw frame 50 ms. Lysosomes have different diameters and with the used plasmid, the outer membrane was stained. The membrane structure of bigger lysosomes (cross-section Ly1, plot e) can be revealed with conventional WF imaging (c) and additional filtering (d), but for smaller lysosomes (cross-section Ly2, plot f) SIM imaging is required. Scale bar 250 nm, exposure time per raw frame 50 ms.

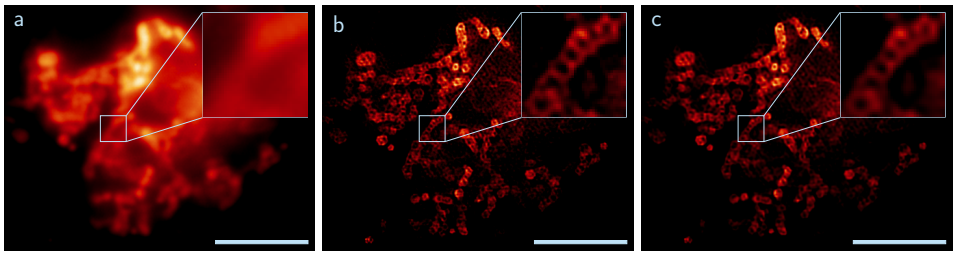


**Figure 5.11.:** Live cell images of mitochondrial motility in U2OS cells. The organelle was stained with MitoTrackerRed and the data were recorded at room temperature. The insets show clearly that the inner structure, the cristae, cannot be resolved with WF imaging (a). For the SIM reconstruction, background signal from the raw data was subtracted and Richardson-Lucy deconvolution (10 iterations) was applied to the input and output images (b). Hessian denoising leads to further improvement of the image quality (c) (scale bar 5 $\mu$m, inset 1.4 $\mu$m x 1.4 $\mu$m, exposure time per raw frame 100 ms).

### 5.4.2. Live-cell imaging

In contrast to imaging fixed samples, live-cell imaging is more challenging. On the one hand, the refractive index of the medium surrounding the cells is different as they are now covered by water instead of being embedded in glycerol. On the other hand, the organelles are now mobile which might lead to motion-blur in the images. To circumvent these factors, image data were recorded at room temperature and more processing for the image reconstruction was utilized. First, background signal was subtracted from the raw data in fairSIM in order to get rid of unwanted background contributions. To further enhance the contrast, fairSIM also allows to apply Richardson-Lucy deconvolution to the input and output data [236]. Finally, by applying Hessian denoising to the reconstructed data it is possible to further smooth the fluorescence signal and further enhance the contrast although some resolution improvement will be lost (parameters: $\mu = 100$, $\sigma = 0.8$) [142].

For the first live-cell experiments mitochondria were stained in U2OS cells using the live cell stain MitoTrackerRed (fig. 5.11). This organelle has an inner structure, the so-called cristae, which is basically a folded membrane. With WF the cristae cannot be resolved because they are too close together, and therefore mitochondria are a popular organelle to demonstrate super-resolution microscopy. With the DMD-SIM microscope live-cell images of mitochondria were recorded. The summed

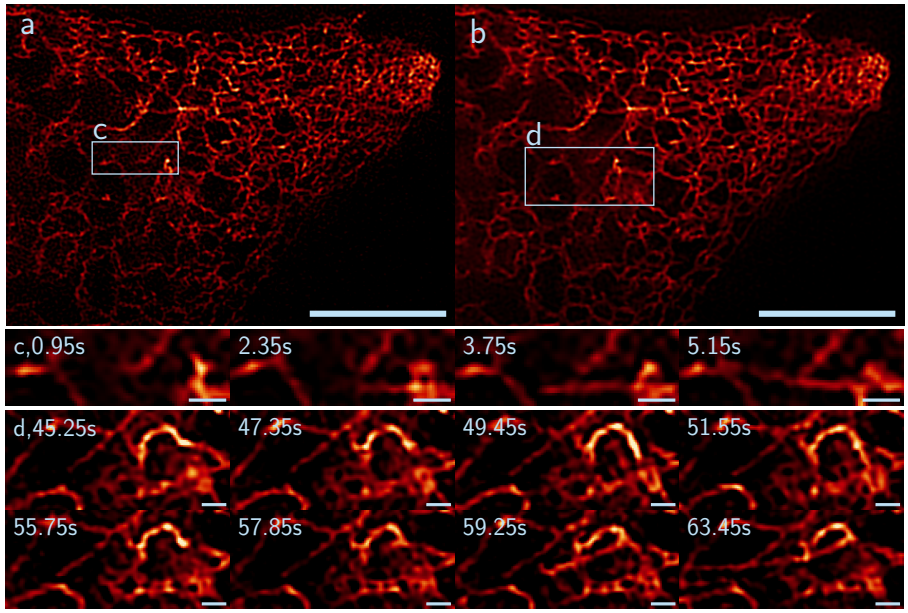


**Figure 5.12.:** Endoplasmic reticulum (ER) network in a living U2OS cell. The organelle was stained with ER-Tracker Red and the data was recorded with a delay of 250 ms between each SIM sequence at room temperature. (a) SIM image at time point 0 s reveals many filaments. (b) Hessian denoising of the SIM frame reduces the background signal and smooths the filaments (scale bar 5 $\mu$m, exposure time per raw frame 50 ms). The time sequence (c) is an inset and shows the elongation of a fiber (scale bar 500 nm). In addition, a detachment can be observed with a subsequent attachment to another point and a further elongation (d, second inset, scale bar 500 nm). Both insets display the Hessian denoised data.

up WF image reveals no inner structure (fig. 5.11a). However, at this point the real-time reconstruction with fairSIM-VIGOR was very convenient because it provided immediate feedback already during the data acquisition that confirmed that in SIM mode it is possible to resolve the cristae. For further post-processing of the recorded data, spurious background contributions were subtracted since the dye also attaches in a small amount to other organelles. In addition, Richardson-Lucy deconvolution was applied to the raw input data to fairSIM, as well as the reconstructed output data, which reduces reconstruction artifacts. This results in a super-resolution image that resolves the inner structure of mitochondria quite well with a conclusive signal to noise ratio (fig. 5.11b). Nonetheless, by applying Hessian denoising to these data, the image quality can be further improved (fig. 5.11c).

To further demonstrate the live-cell imaging compatibility of the DMD-SIM microscope, the movement of the endoplasmic reticulum (ER) network was recorded in living U2OS cells (fig. 5.12). Here, the organelle was stained with ER-TrackerRed and a delay time of 250 ms was set between the SIM frames to keep the stress level for the cells to a minimum and to avoid photobleaching. Therefore, it was possible to record live cell movies which last at least two minutes. Again, the real-time image reconstruction was very convenient for navigating the sample and finding sample areas of high mobility. With SIM the dense ER network can be resolved and the movement of single filaments can easily be resolved (fig. 5.12a). Further image processing with Hessian denoising was very convenient in this case, because it smooths the filaments and makes it easier to follow their movement (fig. 5.12b-d). In fig. 5.12c it is visible that one filament elongates along the $x$-axis. In addition, the detachment of a filament can be observed at a knot within the network and, direct following, its attachment to another point, which is a typical behavior for ER (fig. 5.12d, first row) [155]. Directly at this point the fiber then elongates over a long distance (fig. 5.12d, second row).

## 5.5. SIM revealing the morphology of microgels

Microgels are polymer particles with a spherical shape [237] which can be used for drug delivery, in sensors or as surface coatings. In case these microgels are called *smart*, they respond to an external stimulus such as temperature change with a transformation in size and morphology [238]. It is of interest to study their internal morphology in order to gain more insight in the formation of the polymer network and the dependence on external stimuli. However, due to their small size, approximately 500 nm in diameter, super-resolution microscopy is required to

quantify the internal morphology. Recent work demonstrated that dSTORM is sufficient for the visualization of the internal network [237]. For this study, three different microgels with a core-shell configuration were analyzed with SIM and compared with dSTORM data. These microgels decrease in size of the shell which are further named as *thick*, *intermediate* and *thin* (details in appendix A.2.4). The core has a denser network, and therefore most of the fluorescent dyes are stuck in the shell, so that a ring-shape structure is imaged in 2D.

### 5.5.1. Imaging conditions and modifications

For the experiments, the microgels were embedded in water at 17 °C and imaged with the DMD-SIM setup with real-time reconstruction. However, for 2D-SIM matching the refractive index of the used immersion oil is crucial, because otherwise spherical aberration will result in a poor resolution enhancement. Due to a lower temperature, the refractive index of the oil needed to be lowered as well in order to achieve the same SIM results as if the imaging process would occur at room temperature. Therefore, an immersion oil of 1.510 NA was chosen instead of 1.518 NA. For the imaging process the laser power was set to approximately 250 $\mu$W at the sample and the exposure time was 50 ms for a single raw frame so that the recording only lasted half a second.

The Fiji plugin fairSIM [138] was again used for the SIM reconstruction. The image processing was started by subtracting background signal, namely 75 counts, and corrected for the different illumination intensities in phase and angle. Further, an estimated optical transfer function, with an estimated emission wavelength of $\lambda = 575$ nm, an algorithm-specific compensation of $a = 0.3$ nm under the usage of an oil immersion objective (NA=1.35) was utilized. For the SIM reconstruction itself, the Richardson-Lucy algorithm (one iteration) was applied on the input and output data to reduce reconstruction artifacts.

### 5.5.2. Visualize internal structure

With SIM it was possible to visualize the internal morphology of all three core-shell configurations since the ring-shape structure is clearly visible (fig. 5.13). An analysis with a line plot suggest that the shells had a diameter of approximately 290 nm (thick, fig. 5.13d), 270 nm (intermediate, fig. 5.13h) and 250 nm (thin, fig. 5.13l). However, these were values which should be resolvable with conventional wide-field microscopy. Indeed, the core-shell structure was resolved with WF and further verified in deconvoluted wide-field (dWF), but due to the dense labeling only a few

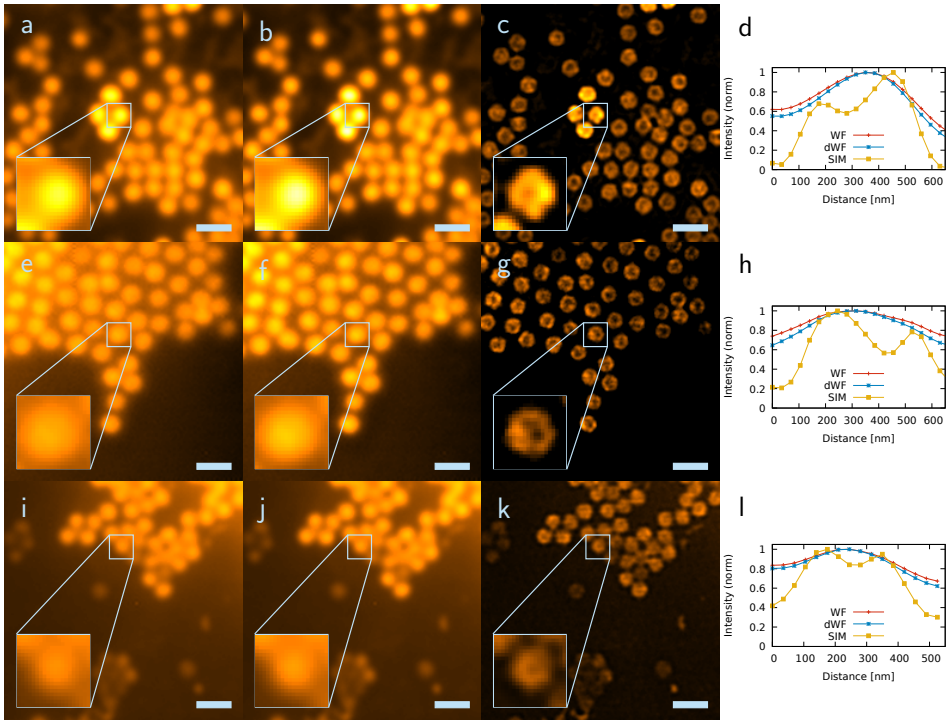


**Figure 5.13.:** Microgels with core-shell configuration with a thick (a-d), intermediate (e-h) or thin (i-l) shell. The first row displays the WF image, second dWF and third SIM. The data sets for the line plots (d,h,l) are taken from the displayed insets. With SIM, the resulting ring-shaped structure can be resolved. The fluorescent dye R6G is mainly present in the shell because the core has a network that is too dense. Scale bar 1 $\mu$m, exposure time per raw frame 50 ms, immersion oil NA 1.510, temperature 17°C.

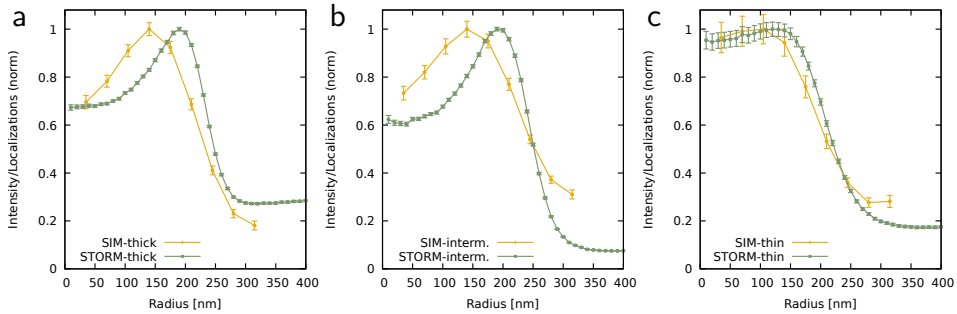


**Figure 5.14.:** Radial intensity/localization distribution of R6G in core-shell microgels 'thick' (a), 'intermediate' (b) and 'thin' (c). At least 15 microgels from fig. 5.13 were taken into account for the analysis. With SIM (yellow) the low density in the core can be resolved, whereas dSTORM data (green) provides a finer sampling (dSTORM data provided by Stephan Bergmann).

microgels could be visualized with the ring-shape. Further, WF and dWF is not sufficient for quantitative image analysis of such microgels because their diameters are close to the diffraction limit, and therefore poorly resolvable.

To further analyze the internal morphology of the core-shell microgel, at least 15 microgels were taken into account to analyze the intensity distribution along their radius. Single microgels were selected manually and then calculated with the Fiji plugin *Radial Profile Extended* [239]. Here, the intensity distribution of a circular region of interest was sectioned in rings concentric to the origin and with increasing radius. Each ring was analyzed and calculated from a 2D shape to an one dimensional data set. By averaging and normalization of the intensity distribution in dependence on the radius of all selected microgels, the SIM data sets reveal a maximum intensity at approximately 140-150 nm for all three configurations (fig. 5.14).

Analysis of microgel data of dSTORM recordings reveals that the obtained results with SIM were consistent with a few limitations (fig. 5.14). On the one hand, both methods confirm the same ring-shape structure. Even the higher intensity distribution of fluorescent dyes in the core of the 'thin' configuration was imaged with SIM and dSTORM. On the other hand, the quantification of the radius show slightly different results because most localizations in dSTORM were imaged at a radius of 200 nm. Indeed, an investigation of the radius of the core only by dSTORM imaging yields a radius of 140 nm. Thus, the maximum intensity of the

shell should be further apart from the core which is verified by dSTORM data. It is expected that dSTORM is more suitable to quantify the internal morphology of microgels since it has the higher resolution gain, and therefore a higher sampling of the microgel is possible. Yet, SIM proved its functionality to visualize and resolve the ring-shape of all three configurations.

## 5.6. Discussion and conclusion

This work provides two significant contributions that further facilitate the overall use of digital micromirror devices for coherent illumination, which is required to utilize them for structured illumination microscopy to its fullest potential. The simulations provided specific information on how the blazed grating effect caused by the DMD substructure affects the SIM illumination pattern, how to identify ideal alignment angles for the device, as well as how manufacturing tolerances in the device affect this alignment. In detail, the simulations demonstrated the impact of the exact tilt angle on the blaze angle. Slight differences results in a huge impact, so that a precise analysis is required.

The design of a SIM system then utilized these findings to employ a DMD as the light modulator, resulting in a very compact and cost-effective SIM system. Additionally, real-time SIM reconstruction can be employed on this system which is convenient for the user to directly evaluate the SIM data. By providing calibration measurements, the resolution enhancement by SIM compared to conventional wide-field was verified. Further, the DMD-SIM system is fully capable of imaging fixed cell samples with chemical dyes and even fluorescent proteins. Live-cell imaging at sub-second acquisition times, revealing dynamics of mitochondria and ER, are also provided by the system. Lastly, microgels were imaged and their internal morphology was visualized. Here, the SIM system presented comparable results to dSTROM measurements.

This work can be viewed as a contribution to the growing efforts of democratizing super-resolution microscopy. Digital micromirror devices are both cost-effective and readily available in many variations, which makes them an attractive alternative to the specialized SLM devices typically employed for SIM, which require more difficult to implement timing schemes [25, 150]. By providing a thorough characterization of the blazed grating effect in the context of SIM, it should now be easy to employ DMDs in different and more complex variations of novel SIM systems for example systems using multiple excitation wavelengths.

# 6. Comprehensive conclusion and outlook

In this thesis, I demonstrated the experimental realization of conventional fluorescence microscopy and optical super-resolution techniques based on compact and cost-efficient implementations. Three specific projects, each focused on a different aspect, were successfully accomplished. In the first concept, a conventional fluorescence microscope with fast 3D image acquisition was realized. Here, the main focus was placed on the construction of a compact, robust and highly portable optical system, employing a space-saving design. The final optical microscope system was shipped to our collaborators at the ISMMS in New York City to perform live-cell imaging in a biosafety laboratory. In the second project, the microscope was slightly modified in order to perform super-resolution microscopy experiments by super-resolved optical fluctuation imaging (SOFI). Here, a cost-efficient industry-grade CMOS camera was qualitatively and quantitatively compared to high-end scientific-grade CMOS and CCD cameras. The results showed that industry-grade CMOS cameras are well suited and sufficient for SOFI imaging and that our custom-built conventional microscope platform is capable of performing SOFI measurements. Lastly, for the cost-efficient implementation of super-resolution structured illumination microscopy (SIM), a digital micromirror device (DMD) was utilized to enable two beam coherent SIM [13]. The detailed characterization of the blazed grating effect inherent to these devices enabled us to set up a fully functional SIM system capable of live-cell imaging.

The compact 3D fluorescence microscope was successfully shipped to ISMMS in New York City to visualize HIV-1 transfer at the virological synapse between T cells. Virus particles were imaged and the subsequent deconvolution step could be efficiently implemented during the imaging process. The imaging results were confirmed by 3D-SIM on fixed samples, so that the 3D fluorescence microscope could be proven as suitable optical system for imaging HIV-1 transfer between living cells. Nevertheless, the microscope can be further improved by reducing the overall size and costs. Novel concepts such as the use of mobile phones in microscopic

imaging [240] and 'cellSTORM' [209] showed that even cellphone cameras can be utilized as sensitive detectors. On the software side, several concepts for real-time deconvolution exist [241, 242], which could be implemented on our microscope. This would allow for directly seeing the images without out-of-focus blur, which enables a better control of the experiment even during data acquisition.

The industry-grade CMOS camera used for the compact fluorescence microscope was further investigated by a direct comparison to scientific-grade cameras in terms of its usefulness for the super-resolution technique SOFI. For this second project, the CMOS camera was first tested on a commercial scientific microscope. The results were of similar quality as those obtained on high-end emCCD cameras, and only slightly worse than those obtained by the latest generation of sCMOS cameras. Additionally, the compact fluorescence microscope system was slightly modified to allow for SOFI data acquisition, and indeed, the custom-built system is fully capable of SOFI imaging. Likewise, the same CMOS cameras are sufficient for single molecule detection by dSTORM [18] experiments, which could be additionally implemented in the compact system by integrating more powerful lasers of suitable wavelengths. The custom-built microscope was even extended to a biplane configuration, which enabled SOFI recordings of two different focal planes simultaneously. Recent work showed that SOFI is also compatible with multi-plane image acquisition [212, 243] which could be integrated easily in the custom-built microscope by exchanging the 50/50 beamsplitter with a multi-plane prism. Overall, the size of the compact fluorescence microscope was preserved, and therefore, it could again be shipped to collaborators, whereas now even super-resolution microscopy is possible.

For the final project, a DMD was utilized in a SIM setup to generate the two beam interference pattern required by this method. Here, cost-efficient components such as the industry-grade CMOS camera and lasers typically used for laser light-show applications were employed to reduce the overall cost. The DMD-based SIM constructed in the course of this work costs less than 20k€, which is a factor of ten times less than the price of commercial SIM system. The custom-built SIM also provides real-time image reconstruction [25], so that the SIM image can be viewed directly during the experiment. The resolution enhancement enables the visualization of single filamentous structures in fixed and live-cell samples with both chemical dyes and fluorescent proteins. Furthermore, the SIM microscope was utilized to resolve the internal structure of microgels. For future work, the blazed grating effect simulation software can help implement multi-color imaging on the DMD-based SIM. For this approach, a single DMD could be required for the

entire setup. Also, the DMD-based SIM could be developed in order to perform TIRF-SIM [58] and even 3D-SIM [14]. Also a combination with SMLM is possible with this setup [157] to double the localization precision. The overall size of the SIM microscope is compact and small in comparison to commercial systems, and therefore it would be possible to easily make this system portable, too. Lastly, the features of the conventional fluorescence microscope could also be merged with the SIM system. Thus, it should be possible to demonstrate a fully equipped configuration capable of SOFI, SIM, dSTORM and conventional imaging, which would still be compact and could be shipped to collaborators at remote sites. This would, for example, allow us to send the system to our collaborators in New York City to visualize and study the transfer of HIV-1 at the virological synapse with live-cell imaging and at super-resolution.

In summary, the work presented here demonstrated that fluorescence microscopy systems can be realized in a compact and cost-efficient manner. As a result, this leads to a valuable contribution to the scientific community [21], so that more researchers in the life sciences could more readily have access to affordable implementations of advanced fluorescence microscopy with super-resolution imaging capability.

# Bibliography


[1] L. Schermelleh et al. “Super-resolution microscopy demystified”. *Nature Cell Biology* 21.1 (2019), pp. 72–84. DOI: 10.1038/s41556-018-0251-8.

[2] E. Abbe. “Beiträge zur Theorie des Mikroskops und der mikroskopischen Wahrnehmung”. *Archiv für mikroskopische Anatomie* 9.1 (1873), pp. 456–468. DOI: 10.1007/BF02956173.

[3] J. R. Swedlow and M. Platani. “Live Cell Imaging Using Wide-Field Microscopy and Deconvolution”. *Cell Structure and Function* 27.5 (2002), pp. 335–341. DOI: 10.1247/csf.27.335.

[4] J. H. Xiao et al. “Characterization of Influenza Virus Pseudotyped with Ebolavirus Glycoprotein”. *Journal of Virology* 92.4 (2018). DOI: 10.1128/JVI.00941-17.

[5] S. Boorboor et al. “Visualization of Neuronal Structures in Wide-Field Microscopy Brain Images”. *IEEE Transactions on Visualization and Computer Graphics* 25.1 (2019), pp. 1018–1028. DOI: 10.1109/TVCG.2018.2864852.

[6] M. Orrit. “Celebrating optical nanoscopy”. *Nature Photonics* 8 (2014). DOI: 10.1038/nphoton.2014.288.

[7] S. W. Hell and J. Wichmann. “Breaking the diffraction resolution limit by stimulated emission: stimulated-emission-depletion fluorescence microscopy”. *Opt. Lett.* 19.11 (1994), pp. 780–782. DOI: 10.1364/OL.19.000780.

[8] E. Betzig et al. “Imaging Intracellular Fluorescent Proteins at Nanometer Resolution”. *Science* 313.5793 (2006), pp. 1642–1645. DOI: 10.1126/science.1127344.

[9] M. J. Rust, M. Bates, and X. Zhuang. “Sub-diffraction-limit imaging by stochastic optical reconstruction microscopy (STORM)”. *Nature Methods* 3.10 (2006), pp. 793–796. DOI: 10.1038/nmeth929.

[10] S. van de Linde et al. “Direct stochastic optical reconstruction microscopy with standard fluorescent probes”. *Nature Protocols* 6 (2011), pp. 991–1009. DOI: 10.1073/pnas.0609643104.

[11] A. Sharonov and R. M. Hochstrasser. “Wide-field subdiffraction imaging by accumulated binding of diffusing probes”. *Proceedings of the National Academy of Sciences* 103 (2006), pp. 18911–18916. DOI: 10.1073/pnas.0609643104.

[12] T. Dertinger et al. “Fast, background-free, 3D super-resolution optical fluctuation imaging (SOFI)”. *Proceedings of the National Academy of Sciences* 106.52 (2009), pp. 22287–22292. DOI: 10.1073/pnas.0907866106.

[13] M. G. Gustafsson. “Surpassing the lateral resolution limit by a factor of two using structured illumination microscopy”. *Journal of microscopy* 198.2 (2000), pp. 82–87. DOI: 10.1046/j.1365-2818.2000.00710.x.

[14] M. G. Gustafsson et al. “Three-dimensional resolution doubling in wide-field fluorescence microscopy by structured illumination”. *Biophysical journal* 94.12 (2008), pp. 4957–4970. DOI: 10.1529/biophysj.107.120345.

[15] S. J. Sahl, S. W. Hell, and S. Jakobs. “Fluorescence nanoscopy in cell biology”. *Nature Reviews Molecular Cell Biology* 18 (2017), pp. 685–701. DOI: 10.1038/nrm.2017.71.

[16] P. G. Pitrone et al. “OpenSPIM: an open-access light-sheet microscopy platform”. *Nature Methods* (2013). DOI: 10.1038/nmeth.2507.

[17] T. Holm et al. “A Blueprint for Cost-Efficient Localization Microscopy”. *ChemPhysChem* 15.4 (2014), pp. 651–654. DOI: 10.1002/cphc.201300739.

[18] R. Diekmann et al. “Characterization of an industry-grade CMOS camera well suited for single molecule localization microscopy - high performance super-resolution at low cost”. *Scientific Reports* 7 (2017), p. 14425. DOI: 10.1038/s41598-017-14762-6.

[19] Y. S. Zhang et al. “A cost-effective fluorescence mini-microscope for biomedical applications”. *Lab Chip* 15 (2015), pp. 3661–3669. DOI: 10.1039/C5LC00666J.

[20] K. Yamagata et al. “Fluorescence Cell Imaging and Manipulation Using Conventional Halogen Lamp Microscopy”. *PLOS ONE* 7.2 (2012), pp. 1–8. DOI: 10.1371/journal.pone.0031638.

[21] R. M. Power and J. Huisken. “Putting advanced microscopy in the hands of biologists”. *Nature Methods* (2019). DOI: 10.1038/s41592-019-0618-1.

[22] R. Witte et al. “Concepts in Light Microscopy of Viruses”. *Viruses* 10.4 (2018). DOI: 10.3390/v10040202.

[23] N. Parveen et al. “Single Viruses on the Fluorescence Microscope: Imaging Molecular Mobility, Interactions and Structure Sheds New Light on Viral Replication”. *Viruses* 10.5 (2018). DOI: 10.3390/v10050250.

[24] J. Chojnacki and C. Eggeling. “Super-resolution fluorescence microscopy studies of human immunodeficiency virus”. *Retrovirology* 15.1 (2018). DOI: 10.1186/s12977-018-0424-3.

[25] A. Markwirth et al. “Video-rate multi-color structured illumination microscopy with simultaneous real-time reconstruction”. *Nature Communications* 10 (2019). DOI: 10.1038/s41467-019-12165-x.

[26] J. R. Lakowicz. *Principles of Fluorescence Spectroscopy*. Springer, 2006.

[27] U. Kubitscheck, ed. *Fluorescence Microscopy*. Wiley-Backwell, 2013.

[28] B. Bransden and C. Joachain. *Physics of Atoms and Molecules*. Pearson Education, 2003.

[29] J. Popp et al., eds. *Handbook of Biophotonics, Vol. 1 Basics and Techniques*. Wiley-VCH, 2011.

[30] J. B. Pawley, ed. *Handbook of biological confocal microscopy*. 2. ed. New York: Plenum Press, 1995.

[31] P. J. Cranfill et al. “Quantitative assessment of fluorescent proteins”. *Nature Methods* 13 (2016), pp. 557–562. DOI: 10.1038/nmeth.3891.

[32] F. Ströhl. “Theoretical and Experimental Concepts to Increase the Performance of Structured Illumination Microscopy”. PhD thesis. University of Cambridge, 2018.

[33] E. Hecht. *Optik*. De Gruyter, 2014.

[34] L. R. F.R.S. “XXXI. Investigations in optics, with special reference to the spectroscope”. *The London, Edinburgh, and Dublin Philosophical Magazine and Journal of Science* 8.49 (1879), pp. 261–274. DOI: 10.1080/14786447908639684.

[35] C. M. Sparrow. “On Spectroscopic Resolving Power”. *Astrophysical Journal* 44 (1916), p. 76. DOI: 10.1086/142271.

[36] J. W. Goodman. *Introduction to Fourier optics*. 3. ed. Englewood, Colo.: Roberts, 2005.

[37] D. A. Boas, C. Pitris, and N. Ramanujam, eds. *Handbook of Biomedical Optics*. CRC Press, 2011.

[38] Y. Wu and H. Shroff. "Faster, sharper, and deeper: structured illumination microscopy for biological imaging". *Nature methods* (2018), p. 1. DOI: 10.1038/s41592-018-0211-z.

[39] S. Koho et al. "Fourier ring correlation simplifies image restoration in fluorescence microscopy". *Nature Communications* 10 (2019). DOI: 10.1038/s41467-019-11024-z.

[40] A. T. Wassie, Y. Zhao, and E. S. Boyden. "Expansion microscopy: principles and uses in biological research". *Nature Methods* 16 (2019), pp. 33–41. DOI: 10.1038/nmeth.2843.

[41] B. Zhang, J. Zerubia, and J.-C. Olivo-Marin. "Gaussian approximations of fluorescence microscope point-spread function models". *Appl. Opt.* 46.10 (2007), pp. 1819–1829. DOI: 10.1364/AO.46.001819.

[42] R. W. Cole, T. Jinadasa, and C. M. Brown. "Measuring and interpreting point spread functions to determine confocal microscope resolution and ensure quality control". *Nature Protocols* 6 (2011), pp. 1929–1941. DOI: 10.1038/nprot.2011.407.

[43] H. Deschout et al. "Precisely and accurately localizing single emitters in fluorescence microscopy". *Nature Methods* 11 (2014), pp. 253–266. DOI: 10.1038/nmeth.2843.

[44] R. Diekmann et al. "Chip-based wide field-of-view nanoscopy". *Nature Photonics* 11 (2017), pp. 322–328. DOI: 10.1038/nphoton.2017.55.

[45] J. Enderlein, E. Toprak, and P. R. Selvin. "Polarization effect on position accuracy of fluorophore localization". *Opt. Express* 14.18 (2006), pp. 8111–8120. DOI: 10.1364/OE.14.008111.

[46] R. P. Nieuwenhuizen et al. "Measuring image resolution in optical nanoscopy". *Nature Methods* 10.6 (2013), p. 557. DOI: 10.1038/nmeth.2448.

[47] N. Banterle et al. "Fourier ring correlation as a resolution criterion for super-resolution microscopy". *Journal of Structural Biology* 183 (2013), pp. 363–367. DOI: 10.1016/j.jsb.2013.05.004.

[48] C. A. Schneider, W. S. Rasband, and K. W. Eliceiri. "NIH Image to ImageJ: 25 years of image analysis". *Nature Methods* 9.7 (2012), pp. 671–675. DOI: 10.1038/nmeth.2089.

[49] J. Schindelin et al. "Fiji: an open-source platform for biological-image analysis". *Nature Methods* 9.7 (2012), pp. 676–682. DOI: 10.1038/nmeth.2019.

[50] O. Burri. *IJP-FRC Fourier ring correlation plugin*. https://github.com/BIOP/ijp-frc.

[51] R. Diekmann. "Extending the application range of optical nanoscopy". PhD thesis. Universität Bielefeld, 2017.

[52] M. Sauer, J. Hofkens, and J. Enderlein. *Handbook of Fluorescence Spectroscopy and Imaging*. Wiley-VCH, 2011.

[53] K. K. Ghosh et al. "Miniaturized integration of a fluorescence microscope". *Nature Methods* 8 (2011), pp. 871–878. DOI: 10.1038/nmeth.1694.

[54] S. Schaefer, S. A. Boehm, and K. J. Chau. "Automated, portable, low-cost bright-field and fluorescence microscope with autofocus and autoscanning capabilities". *Appl. Opt.* 51.14 (2012), pp. 2581–2588. DOI: 10.1364/AO.51.002581.

[55] V. Mönkemöller. "Optical Super-Resolution Microscopy of the Structure and Dynamics of Cellular Nanopores". PhD thesis. Universität Bielefeld, 2016.

[56] J Vangindertael et al. "An introduction to optical super-resolution microscopy for the adventurous biologist". *Methods and Applications in Fluorescence* 6.2 (2018), p. 022003. DOI: 10.1088/2050-6120/aaae0c.

[57] M. Tokunaga, N. Imamoto, and K. Sakata-Sogawa. "Highly inclined thin illumination enables clear single-molecule imaging in cells". *Nature Methods* 5 (2008), pp. 159–161. DOI: 10.1038/nmeth1171.

[58] M. L. Martin-Fernandez, C. J. Tynan, and S. E. D. Webb. "A 'pocket guide' to total internal reflection fluorescence". *Journal of Microscopy* 252 (2013), pp. 16–22. DOI: 10.1111/jmi.12070.

[59] J. Art. "Photon Detectors for Confocal Microscopy". *Handbook Of Biological Confocal Microscopy*. Boston, MA: Springer US, 2006, pp. 251–264. DOI: 10.1007/978-0-387-45524-2_12.

[60] A. Marktwirth. "Development of a video rate, multi-colour structured illumination microscope". Diploma thesis. Universität Bielefeld, 2016.

[61] W. S. Boyle and G. E. Smith. "Charge Coupled Semiconductor Devices". *Bell System Technical Journal* 49.4 (1970), pp. 587–593. DOI: 10.1002/j.1538-7305.1970.tb01790.x.

[62] M. S. Robbins. "Electron-Multiplying Charge Coupled Devices – EMCCDs". *Single-Photon Imaging*. Springer Berlin Heidelberg, 2011, pp. 103–121. DOI: 10.1007/978-3-642-18443-7_6.

[63] G. Holst. “Camera Tutorial - How to choose and use the right camera for a microscopy application”. *Focus on Microscopy*. 2014.

[64] R. J. Baker. *CMOS: Circuit Design, Layout, and Simulation*. 3. ed. IEEE Press series on microelectronic systems. IEEE Press, 2010.

[65] H. Nyquist. “Certain Topics in Telegraph Transmission Theory”. *Transactions of the American Institute of Electrical Engineers* 47 (1928), pp. 617–644. DOI: 10.1109/T-AIEE.1928.5055024.

[66] C. E. Shannon. “Communication in the Presence of Noise”. *Proceedings of the IRE* 37 (1949), pp. 10–21. DOI: 10.1109/JRPROC.1949.232969.

[67] W. Wallace, L. H. Schäfer, and J. R. Swedlow. “A workingperson’s guide to deconvolution in light microscopy”. *BioTechniques* 31 (2001), pp. 1076–1097. DOI: 10.2144/01315bi01.

[68] C. Wang et al. “Deconvolution of subcellular protrusion heterogeneity and the underlying actin regulator dynamics from live cell imaging”. *Nature Communications* 9.1688 (2018). DOI: 10.1038/s41467-018-04030-0.

[69] J. L. Starck, E. Pantin, and F. Murtagh. “Deconvolution in Astronomy: A Review”. *Astronomical Society of the Pacific* (2002). DOI: 10.1086/342606.

[70] A. Boryat and B. Joshi. “A Review Paper: Noise models in digital image processing”. *Signal and Image Processing: An International Journal* 6 (2015). DOI: 10.5121/sipij.2016.60206.

[71] J. R. Swedlow. “Quantitative Fluorescence Microscopy and Image Deconvolution”. *Methods in Cell Biology* 81 (2007), pp. 447–465. DOI: 10.1016/S0091-679X(06)81021-6.

[72] J. G.McNally et al. “Three-Dimensional Imaging by Deconvolution Microscopy”. *Methods* 19 (1999), pp. 373–385. DOI: doi.org/10.1006/meth.1999.0873.

[73] H. Kirshner et al. “3-D PSF fitting for fluorescence microscopy: implementation and localization application”. *Journal of Microscopy* 249.1 (2013), pp. 13–25. DOI: 10.1111/j.1365-2818.2012.03675.x.

[74] M. Born and E. Wolf. *Principles of optics*. 4. ed. Oxford: Pergamon Press, 1970.

[75] S. F. Gibson and F. Lanni. “Diffraction by a circular aperture as a model for three-dimensional optical microscopy”. *J. Opt. Soc. Am. A* 6.9 (1989), pp. 1357–1367. DOI: 10.1364/JOSAA.6.001357.

[76] D. Sage et al. “DeconvolutionLab2: An open-source software for deconvolution microscopy”. *Methods* 115 (2017), pp. 28–41. DOI: 10.1016/j.ymeth.2016.12.015.

[77] N. Wiener. *Extrapolation, interpolation, and smoothing of stationary time series*. Cambridge, Mass.: M.I.T. Pr., 1970.

[78] W. H. Richardson. “Bayesian-Based Iterative Method of Image Restoration”. *J. Opt. Soc. Am.* 62.1 (1972), pp. 55–59. DOI: 10.1364/JOSA.62.000055.

[79] L. Lucy. “An iterative technique for the rectification of observed distributions”. *Astronomical Journal* 79 (1974). DOI: 10.1086/111605.

[80] W. E. Moerner and L. Kador. “Optical detection and spectroscopy of single molecules in a solid”. *Phys. Rev. Lett.* 62 (1989), pp. 2535–2538. DOI: 10.1103/PhysRevLett.62.2535.

[81] S. W. Hell and M. Kroug. “Ground-state-depletion fluorscence microscopy: A concept for breaking the diffraction resolution limit”. *Applied Physics B* 60.5 (1995), pp. 495–497. DOI: 10.1007/BF01081333.

[82] T. A. Klar et al. “Fluorescence microscopy with diffraction resolution barrier broken by stimulated emission”. *Proceedings of the National Academy of Sciences* 97.15 (2000), pp. 8206–8210. DOI: 10.1073/pnas.97.15.8206.

[83] L. Schermelleh, R. Heintzmann, and H. Leonhardt. “A guide to super-resolution fluorescence microscopy”. *The Journal of Cell Biology* 190.2 (2010), pp. 165–175. DOI: 10.1083/jcb.201002018.

[84] C. G. Galbraith and J. A. Galbraith. “Super-resolution microscopy at a glance”. *Journal of Cell Science* 124.10 (2011), pp. 1607–1611. DOI: 10.1242/jcs.080085.

[85] M. Hofmann et al. “Breaking the diffraction barrier in fluorescence microscopy at low light intensities by using reversibly photoswitchable proteins”. *Proceedings of the National Academy of Sciences* 102.49 (2005), pp. 17565–17569. DOI: 10.1073/pnas.0506010102.

[86] K. I. Willig et al. “STED microscopy reveals that synaptotagmin remains clustered after synaptic vesicle exocytosis”. *Nature* 440 (2006), pp. 935–939. DOI: 10.1038/nature04592.

[87] N. Kilian et al. “Assessing photodamage in live-cell STED microscopy”. *Nature Methods* 15 (2018), pp. 755–756. DOI: 10.1038/s41592-018-0145-5.

[88] G. Leménager et al. “Super-resolution fluorescence imaging of biocompatible carbon dots”. *Nanoscale* 6 (2014), pp. 8617–8623. DOI: 10.1039/C4NR01970A.

[89] D. Wildanger et al. “Solid Immersion Facilitates Fluorescence Microscopy with Nanometer Resolution and Sub-Ångström Emitter Localization”. *Advanced Materials* 24.44 (2012), pp. 309–313. DOI: 10.1002/adma.201203033.

[90] P. Ilgen et al. “STED Super-Resolution Microscopy of Clinical Paraffin-Embedded Human Rectal Cancer Tissue”. *PLOS ONE* 9.7 (2014), pp. 1–8. DOI: 10.1371/journal.pone.0101563.

[91] E. D’Este et al. “STED Nanoscopy Reveals the Ubiquity of Subcortical Cytoskeleton Periodicity in Living Neurons”. *Cell Reports* 10.8 (2015), pp. 1246–1251. DOI: 10.1016/j.celrep.2015.02.007.

[92] E. D’Este et al. “Ultrastructural anatomy of nodes of Ranvier in the peripheral nervous system as revealed by STED microscopy”. *Proceedings of the National Academy of Sciences* 114.2 (2017), pp. 191–199. DOI: 10.1073/pnas.1619553114.

[93] H. Nishimune et al. “Dual-color STED microscopy reveals a sandwich structure of Bassoon and Piccolo in active zones of adult and aged mice”. *Scientific Reports* 6 (2016). DOI: 10.1038/srep27935.

[94] C. Eggeling et al. “Direct observation of the nanoscale dynamics of membrane lipids in a living cell”. *Nature* 457 (2009), pp. 1159–1162. DOI: 10.1038/nature07596.

[95] S. J. Sahl et al. “Fast molecular tracking maps nanoscale dynamics of plasma membrane lipids”. *Proceedings of the National Academy of Sciences* 107.15 (2010), pp. 6829–6834. DOI: 10.1073/pnas.0912894107.

[96] J. Tønnesen et al. “Spine neck plasticity regulates compartmentalization of synapses”. *Nature Neuroscience* 17 (2014), pp. 678–685. DOI: 10.1038/nn.3682.

[97] R. M. Dickson et al. “On/off blinking and switching behaviour of single molecules of green fluorescent protein”. *Nature* 388.6640 (1997), pp. 355–358. DOI: 10.1038/41048.

[98] S. T. Hess, T. P. K. Girirajan, and M. D. Mason. “Ultra-high resolution imaging by fluorescence photoactivation localization microscopy”. *Biophysical journal* 91.11 (2006), pp. 4248–4272. DOI: 10.1529/biophysj.106.091116.

[99] M. Heilemann et al. “Subdiffraction-Resolution Fluorescence Imaging with Conventional Fluorescent Probes”. *Angewandte Chemie International Edition* 47.33 (2008), pp. 6172–6176. DOI: 10.1002/anie.200802376.

[100] R. Jungmann et al. “Multiplexed 3D cellular super-resolution imaging with DNA-PAINT and Exchange-PAINT”. *Nature Methods* 11 (2014), pp. 313–318. DOI: 10.1038/nmeth.2835.

[101] R. Henriques et al. “QuickPALM: 3D real-time photoactivation nanoscopy image processing in ImageJ”. *Nature methods* 7.5 (2010), pp. 339–340. DOI: 10.1038/nmeth0510-339.

[102] S. Wolter et al. “rapidSTORM: accurate, fast open-source software for localization microscopy”. *Nature methods* 9.11 (2012), pp. 1040–1041. DOI: 10.1038/nmeth.2224.

[103] M. Ovesnỳ et al. “ThunderSTORM: a comprehensive ImageJ plug-in for PALM and STORM data analysis and super-resolution imaging”. *Bioinformatics* 30.16 (2014), pp. 2389–2390. DOI: 10.1093/bioinformatics/btu202.

[104] D. Sage et al. “Super-Resolution Fight Club: Assessment of 2D and 3D Single-Molecule Localization Microscopy Software”. *Nature Methods* 16.5 (2018), pp. 387–395. DOI: 10.1038/s41592-019-0364-4.

[105] B. Huang et al. “Three-Dimensional Super-Resolution Imaging by Stochastic Optical Reconstruction Microscopy”. *Science* 319.5864 (2008), pp. 810–813. DOI: 10.1126/science.1153529.

[106] H. Shroff et al. “Dual-color superresolution imaging of genetically expressed probes within individual adhesion complexes”. *Proceedings of the National Academy of Sciences* 104.51 (2007), pp. 20308–20313. DOI: 10.1073/pnas.0710517105.

[107] A. Löschberger et al. “Super-resolution imaging visualizes the eightfold symmetry of gp210 proteins around the nuclear pore complex and resolves the central channel with nanometer resolution”. *Journal of Cell Science* 125.3 (2012), pp. 570–575. DOI: 10.1242/jcs.098822.

[108] A. Szymborska et al. “Nuclear Pore Scaffold Structure Analyzed by Super-Resolution Microscopy and Particle Averaging”. *Science* 341.6146 (2013), pp. 655–658. DOI: 10.1126/science.1240672.

[109] K. Xu, G. Zhong, and X. Zhuang. "Actin, Spectrin, and Associated Proteins Form a Periodic Cytoskeletal Structure in Axons". *Science* 339.6118 (2013), pp. 452–456. DOI: 10.1126/science.1232251.

[110] A. Dani et al. "Superresolution Imaging of Chemical Synapses in the Brain". *Neuron* 68.5 (2010), pp. 843–856. DOI: 10.1016/j.neuron.2010.11.021.

[111] R. Salvador-Gallego et al. "Bax assembly into rings and arcs in apoptotic mitochondria is linked to membrane pores". *The EMBO Journal* 35.4 (2016), pp. 389–401. DOI: 10.15252/embj.201593384.

[112] T. Dertinger et al. "Achieving increased resolution and more pixels with Superresolution Optical Fluctuation Imaging (SOFI)". *Opt. Express* 18.18 (2010), pp. 18875–18885. DOI: 10.1364/OE.18.018875.

[113] T. Dertinger et al. "Advances in superresolution optical fluctuation imaging (SOFI)". *Quarterly Reviews of Biophysics* 46.2 (2013), pp. 210–221. DOI: 10.1017/S0033583513000036.

[114] J. M. Mendel. "Tutorial on higher-order statistics (spectra) in signal processing and system theory: theoretical results and some applications". *Proceedings of the IEEE* 79.3 (1991), pp. 278–305. DOI: 10.1109/5.75086.

[115] S. Geissbuehler, C. Dellagiacoma, and T. Lasser. "Comparison between SOFI and STORM". *Biomed. Opt. Express* 2.3 (2011), pp. 408–420. DOI: 10.1364/BOE.2.000408.

[116] P. Dedecker et al. "Localizer: fast, accurate, open-source, and modular software package for superresolution microscopy". *Journal of Biomedical Optics* 17.12 (2012), pp. 1 –5. DOI: 10.1117/1.JBO.17.12.126008.

[117] A. Girsault et al. "SOFI Simulation Tool: A Software Package for Simulating and Testing Super-Resolution Optical Fluctuation Imaging". *PLOS ONE* 11.9 (2016), pp. 1–13. DOI: 10.1371/journal.pone.0161602.

[118] S. Geissbuehler et al. "Mapping molecular statistics with balanced superresolution optical fluctuation imaging (bSOFI)". *Optical Nanoscopy* 1 (2012). DOI: 10.1186/2192-2853-1-4.

[119] W. Vandenberg and P. Dedecker. "Effect of probe diffusion on the SOFI imaging accuracy". *Scientific Reports* 7 (2017). DOI: 10.1038/srep44665.

[120] Y. Peeters et al. "Correcting for photodestruction in super-resolution optical fluctuation imaging". *Scientific Reports* 7 (2017). DOI: 10.1038/s41598-017-09666-4.

[121] S. Duwé, W. Vandenberg, and P. Dedecker. “Live-cell monochromatic dual-label sub-diffraction microscopy by mt-pcSOFI”. *Chem. Commun.* 53 (2017), pp. 7242–7245. DOI: 10.1039/C7CC02344H.

[122] M. Andresen et al. “Structural basis for reversible photoswitching in Dronpa”. *Proceedings of the National Academy of Sciences* 104.32 (2007), pp. 13005–13009. DOI: 10.1073/pnas.0700629104.

[123] T. Dertinger et al. “Superresolution Optical Fluctuation Imaging with Organic Dyes”. *Angewandte Chemie International Edition* 49.49 (2010), pp. 9441–9443. DOI: 10.1002/anie.201004138.

[124] X. Zhang et al. “Development of a Reversibly Switchable Fluorescent Protein for Super-Resolution Optical Fluctuation Imaging (SOFI)”. *ACS Nano* 9.3 (2015), pp. 2659–2667. DOI: doi.org/10.1021/nn5064387.

[125] A. M. Chizhik et al. “Super–Resolution Optical Fluctuation Bio-Imaging with Dual-Color Carbon Nanodots”. *Nano Letters* 16 (2016), pp. 237 –242. DOI: 10.1021/acs.nanolett.5b03609.

[126] Z. Sun et al. “Semiconducting Polymer Dots with Modulated Photoblinking for High-Order Super-Resolution Optical Fluctuation Imaging”. *Advanced Optical Materials* 7.9 (2019). DOI: 10.1002/adom.201900007.

[127] T. Dertinger et al. “SOFI-based 3D superresolution sectioning with a widefield microscope”. *Optical Nanoscopy* 1 (2012). DOI: 10.1186/2192-2853-1-2.

[128] S. Geissbuehler et al. “Live–cell multiplane three–dimensional super–resolution optical fluctuation imaging”. *Nature Communication* 5 (2014). DOI: 10.1038/ncomms6830.

[129] H. Deschout et al. “Complementarity of PALM and SOFI for super-resolution live-cell imaging of focal adhesions”. *Nature Communications* 7 (2016). DOI: 10.1038/ncomms13693.

[130] R. Heintzmann and C. G. Cremer. “Laterally modulated excitation microscopy: improvement of resolution by using a diffraction grating”. *Optical Biopsies and Microscopic Techniques III*. Vol. 3568. International Society for Optics and Photonics. 1999, pp. 185–197. DOI: 10.1117/12.336833.

[131] J. T. Frohn. “Super-resolution fluorescence microscopy by structured ligth illumination”. Nr. 13916. PhD thesis. Technische Wissenschaften ETH Zürich, 2000. DOI: 10.3929/ethz-a-004064016.

[132] R. Heintzmann and T. Huser. "Super-Resolution Structured Illumination Microscopy". *Chemical Reviews* 177.23 (2017), pp. 13890–13908. DOI: 10.1021/acs.chemrev.7b00218.

[133] J. Demmerle et al. "Strategic and practical guidelines for successful structured illumination microscopy". *Nature Protocols* 12.5 (2017), p. 988. DOI: 10.1038/nprot.2017.019.

[134] K. Wicker et al. "Phase optimisation for structured illumination microscopy". *Optics express* 21.2 (2013), pp. 2032–2049. DOI: 10.1364/OE.21.002032.

[135] B.-J. Chang et al. "Isotropic image in structured illumination microscopy patterned with a spatial light modulator". *Optics express* 17.17 (2009), pp. 14710–14721. DOI: 10.1364/OE.17.014710.

[136] N. Chakrova. "Versatile Structured Illumination Microscopy". PhD thesis. TU Delft, 2017.

[137] K. Wicker. "Non-iterative determination of pattern phase in structured illumination microscopy using auto-correlations in Fourier space". *Optics express* 21.21 (2013), pp. 24692–24701. DOI: 10.1364/OE.21.024692.

[138] M. Müller et al. "Open-source image reconstruction of super-resolution structured illumination microscopy data in ImageJ". *Nature Communications* 7 (2016), p. 10980. DOI: 10.1038/ncomms10980.

[139] A. Lal, C. Shan, and P. Xi. "Structured illumination microscopy image reconstruction algorithm". *IEEE Journal of Selected Topics in Quantum Electronics* 22.4 (2016). DOI: 10.1109/JSTQE.2016.2521542.

[140] P. Křížek et al. "SIMToolbox: a MATLAB toolbox for structured illumination fluorescence microscopy". *Bioinformatics* 32.2 (2016), pp. 318–320. DOI: 10.1093/bioinformatics/btv576.

[141] T. Lukeš et al. "Three-dimensional super-resolution structured illumination microscopy with maximum a posteriori probability image estimation". *Opt. Express* 22.24 (2014), pp. 29805–29817. DOI: 10.1364/OE.22.029805.

[142] X. Huang et al. "Fast, long-term, super-resolution imaging with Hessian structured illumination microscopy". *Nature Biotechnology* (2018). DOI: 10.1038/nbt.4115.

[143] Q. Yang et al. "Method of lateral image reconstruction in structured illumination microscopy with super resolution". *Journal of Innovative Optical Health Sciences* (2015). DOI: 10.1142/S1793545816300020.

[144] C. Karras et al. “Successful optimization of reconstruction parameters in structured illumination microscopy–A practical guide”. *Optics Communications* 436 (2019), pp. 69–75. DOI: 10.1016/j.optcom.2018.12.005.

[145] G. Ball et al. “SIMcheck: a Toolbox for Successful Super-resolution Structured Illumination Microscopy”. *Scientific reports* 5 (2015). DOI: 10.1038/srep15915.

[146] E. H. Rego and L. Shao. “Practical Structured Illumination Microscopy”. *Advanced Fluorescence Microscopy: Methods and Protocols*. Springer New York, 2015, pp. 175–192. DOI: 10.1007/978-1-4939-2080-8_10.

[147] R. Fiolka et al. “Time-lapse two-color 3D imaging of live cells with doubled resolution using structured illumination”. *Proceedings of the National Academy of Sciences* 109.14 (2012), pp. 5311–5315. DOI: 10.1073/pnas.1119262109.

[148] R. Förster et al. “Simple structured illumination microscope setup with high acquisition speed by using a spatial light modulator”. *Optics Express* 22.17 (2014), pp. 20663–20677. DOI: 10.1364/OE.22.020663.

[149] D. Dan et al. “DMD-based LED-illumination Super-resolution and optical sectioning microscopy”. *Scientific reports* 3 (2013). DOI: 10.1038/srep01116.

[150] H.-W. Lu-Walther et al. “fastSIM: a practical implementation of fast structured illumination microscopy”. *Methods and Applications in Fluorescence* 3.1 (2015). DOI: 10.1088/2050-6120/3/1/014001.

[151] L. Song et al. “Fast structured illumination microscopy using rolling shutter cameras”. *Measurement Science and Technology* 27.5 (2016). DOI: 10.1088/0957-0233/27/5/055401.

[152] M. Brunstein et al. “Full-field dual-color 100-nm super-resolution imaging reveals organization and dynamics of mitochondrial and ER networks”. *Opt. Express* 21.22 (2013), pp. 26162–26173. DOI: 10.1364/OE.21.026162.

[153] K. O’Holleran and M. Shaw. “Polarization effects on contrast in structured illumination microscopy”. *Optics letters* 37.22 (2012), pp. 4603–4605. DOI: 10.1364/OL.37.004603.

[154] L. J. Young, F. Ströhl, and C. F. Kaminski. “A guide to structured illumination TIRF microscopy at high speed with multiple colors”. *Journal of visualized experiments: JoVE* 111 (2016). DOI: 10.3791/53988.

[155] Y. Guo et al. “Visualizing Intracellular Organelle and Cytoskeletal Interactions at Nanoscale Resolution on Millisecond Timescales”. *Cell* 175.5 (2018), pp. 1–13. DOI: 10.1016/j.cell.2018.09.057.

[156] B.-C. Chen et al. “Lattice light-sheet microscopy: Imaging molecules to embryos at high spatiotemporal resolution”. *Science* 346.6208 (2014). DOI: 10.1126/science.1257998.

[157] L. Reymond et al. “SIMPLE: Structured illumination based point localization estimator with enhanced precision”. *Optics Express* 27.17 (2019), pp. 24578–24590. DOI: 10.1364/OE.27.024578.

[158] J. Cnossen et al. “Localization microscopy at doubled precision with patterned illumination”. *bioRxiv* (2019). DOI: 10.1101/554337.

[159] L. Gu et al. “Molecular resolution imaging by repetitive optical selective exposure”. *Nature Methods* (2019). DOI: 10.1038/s41592-019-0544-2.

[160] E. H. Rego et al. “Nonlinear structured-illumination microscopy with a photoswitchable protein reveals cellular structures at 50-nm resolution”. *Proceedings of the National Academy of Sciences* 109.3 (2012), pp. 135–143. DOI: 10.1073/pnas.1107547108.

[161] S. Abrahamsson et al. “Multifocus structured illumination microscopy for fast volumetric super-resolution imaging”. *Biomedical optics express* 8.9 (2017), pp. 4135–4140. DOI: 10.1364/BOE.8.004135.

[162] A. Descloux et al. “High speed multi-plane super-resolution structured illumination microscopy of living cells using an image-splitting prism”. *bioRxiv* (2019). DOI: 10.1101/773440.

[163] R. D. Goldman and J. R. Swedlow, eds. *Live Cell Imaging: A Laboratory Manual*. 2. Cold Spring Harbor Laboratory Press, 2010.

[164] J. D. Watson and F. H. C. Crick. “Molecular Structure of Nucleic Acids: A Structure for Deoxyribose Nucleic Acid”. *Nature* 171 (1953), pp. 737–738. DOI: 10.1038/171737a0.

[165] K. Munk and D. Jahn, eds. *Genetik*. Taschenlehrbuch Biologie. Stuttgart: Thieme, 2010.

[166] W. Müller-Esterl, ed. *Biochemie*. 2. Heidelberg: Spektrum, Akad. Verl., 2011.

[167] J. Graw. *Genetik*. 5. Berlin: Springer, 2010.

[168] M Chalfie et al. “Green fluorescent protein as a marker for gene expression”. *Science* 263.5148 (1994), pp. 802–805. DOI: 10.1126/science.8303295.

[169] O. Shimomura, F. H. Johnson, and Y. Saiga. “Extraction, Purification and Properties of Aequorin, a Bioluminescent Protein from the Luminous Hydromedusan, Aequorea”. *Journal of Cellular and Comparative Physiology* 59.3 (1962), pp. 223–239. DOI: 10.1002/jcp.1030590302.

[170] R. Y. Tsien. “The Green Fluorescent Protein”. *Annual Review of Biochemistry* 67.1 (1998), pp. 509–544. DOI: 10.1146/annurev.biochem.67.1.509.

[171] D. S. Bindels et al. “mScarlet: a bright monomeric red fluorescent protein for cellular imaging”. *Nature Methods* 14 (2016), pp. 53–56. DOI: 10.1038/nmeth.4074.

[172] B. Alberts and U. Schäfer, eds. *Molekularbiologie der Zelle*. 5. Weinheim: Wiley-VCH, 2011.

[173] H. Batra and S. Pawar. “Current clinical trials update on HIV/AIDS: a systematic review”. *HIV & AIDS Review. International Journal of HIV-Related Problems* 18 (2019). DOI: 10.5114/hivar.2019.86371.

[174] W. E. Johnson. “Origins and evolutionary consequences of ancient endogenous retroviruses”. *Nature Reviews Microbiology* 17 (2019). DOI: 10.1038/s41579-019-0189-2.

[175] S. B. Joseph et al. “Bottlenecks in HIV-1 transmission: insights from the study of founder viruses”. *Nature Reviews Microbiology* 13 (2015). DOI: 10.1038/nrmicro3471.

[176] P. M. Sharp and B. H. Hahn. “Origins of HIV and the AIDS pandemic”. *Cold Spring Harb Perspect Med* 1 (2011). DOI: 10.1101/cshperspect.a006841.

[177] D. H. Barouch. “Challenges in the development of an HIV-1 vaccine”. *Nature* 455 (2008), pp. 613–619. DOI: 10.1038/nature07352.

[178] F Barre-Sinoussi et al. “Isolation of a T-lymphotropic retrovirus from a patient at risk for acquired immune deficiency syndrome (AIDS)”. *Science* 220.4599 (1983), pp. 868–871. DOI: 10.1126/science.6189183.

[179] E. O. Freed. “HIV-1 assembly, release and maturation”. *Nature Reviews Microbiology* 13 (2015). DOI: 10.1038/nrmicro3490.

[180] S. D. Fuller et al. “Cryo-electron microscopy reveals ordered domains in the immature HIV-1 particle”. *Current Biology* 7 (1997), pp. 729–738. DOI: 10.1016/S0960-9822(06)00331-9.

[181] A. de Marco et al. “Structural Analysis of HIV-1 Maturation Using Cryo-Electron Tomography”. *PLOS Pathogens* 6.11 (2010), pp. 1–9. DOI: 10.1371/journal.ppat.1001215.

[182] W. Hübner et al. “Quantitative 3D Video Microscopy of HIV Transfer Across T Cell Virological Synapses”. *Science* 323.5922 (2009), pp. 1743–1747. DOI: 10.1126/science.1167525.

[183] K. Marno et al. “The evolution of structured illumination microscopy in studies of HIV”. *Methods* 88 (2015), pp. 20–27. DOI: 10.1016/j.ymeth.2015.06.007.

[184] P. Carravilla et al. “Molecular recognition of the native HIV-1 MPER revealed by STED microscopy of single virions”. *Nature Communications* 10 (2019). DOI: 10.1038/s41467-018-07962-9.

[185] E. O. Freed. “HIV-1 Gag Proteins: Diverse Functions in the Virus Life Cycle”. *Virology* 251.1 (1998). DOI: {10.1006/viro.1998.9398}.

[186] M. A. Checkley, B. G. Luttge, and E. O. Freed. “HIV-1 envelope glycoprotein biosynthesis, trafficking, and incorporation”. *Journal of molecular biology* 410.4 (2012). DOI: {10.1016/j.jmb.2011.04.042}.

[187] K. T. Arrildt, S. B. Joseph, and R. Swanstrom. “The HIV-1 env protein: a coat of many colors”. *Curr HIV/AIDS Rep* 9.1 (2012). DOI: {10.1007/s11904-011-0107-3}.

[188] L. Wang et al. “Visualization of HIV T Cell Virological Synapses and Virus-Containing Compartments by Three-Dimensional Correlative Light and Electron Microscopy”. *Journal of Virology* 91.2 (2017). DOI: 10.1128/JVI.01605-16.

[189] L. Wang et al. “Sequential trafficking of Env and Gag to HIV-1 T cell virological synapses revealed by live imaging”. *Retrovirology* 16.2 (2019). DOI: {10.1186/s12977-019-0464-3}.

[190] C. A. Buttler et al. “Single molecule fate of HIV-1 envelope reveals late-stage viral lattice incorporation”. *Nature Communications* 9.1 (2018). DOI: {10.1038/s41467-018-04220-w}.

[191] A. Edelstein et al. “Computer control of microscopes using $\mu$Manager”. *Current protocols in molecular biology* (2010), pp. 14–20. DOI: 10.1002/0471142727.mb1420s92.

[192] A. D. Edelstein et al. “Advanced methods of microscope control using $\mu$Manager software”. *Journal of biological methods* 1.2 (2014). DOI: 10.14440/jbm.2014.36.

[193] C. B. Wilen, J. C. Tilton, and R. W. Doms. “HIV: cell binding and entry”. *Cold Spring Harb Perspect Med* 2 (2012). DOI: 10.1101/cshperspect.a006866.

[194] C. Jolly et al. “HIV-1 Cell to Cell Transfer across an Env-induced, Actin-dependent Synapse”. *Journal of Experimental Medicine* 199.2 (2004), pp. 283–293. DOI: 10.1084/jem.20030648.

[195] B. M. Dale et al. “Cell-to-Cell Transfer of HIV-1 via Virological Synapses Leads to Endosomal Virion Maturation that Activates Viral Membrane Fusion”. *Cell Host & Microbe* 10 (2011), pp. 551–562. DOI: 10.1016/j.chom.2011.10.015.

[196] P. Chen et al. “Predominant Mode of Human Immunodeficiency Virus Transfer between T Cells Is Mediated by Sustained Env-Dependent Neutralization -Resistant Virological Synapses”. *Journal of Virology* 81.22 (2007), pp. 12582–12595. DOI: 10.1128/JVI.00381-07.

[197] W.-S. Hu and S. H. Hughes. “HIV-1 reverse transcription”. *Cold Spring Harb Perspect Med* 2.10 (2012). DOI: 10.1101/cshperspect.a006882.

[198] W. Hübner et al. “Sequence of Human Immunodeficiency Virus Type 1 (HIV-1) Gag Localization and Oligomerization Monitored with Live Confocal Imaging of a Replication-Competent, Fluorescently Tagged HIV-1”. *Journal of Virology* 81.22 (2007), pp. 12596–12607. DOI: 10.1128/JVI.01088-07.

[199] S. Nakane, A. Iwamoto, and Z. Matsuda. “The V4 and V5 Variable Loops of HIV-1 Envelope Glycoprotein Are Tolerant to Insertion of Green Fluorescent Protein and Are Useful Targets for Labeling”. *Journal of Biological Chemistry* 290.24 (2015), pp. 15279–15291. DOI: 10.1074/jbc.M114.628610.

[200] G. N. Llewellyn et al. “Nucleocapsid Promotes Localization of HIV-1 Gag to Uropods That Participate in Virological Synapses between T Cells”. *PLOS Pathogens* 6.10 (2010). DOI: 10.1371/journal.ppat.1001167.

[201] C. Jolly. “T Cell Polarization at the Virological Synapse”. *Viruses* 2.6 (2010). DOI: 10.3390/v2061261.

[202] G. N. Llewellyn et al. “HIV-1 Gag Associates with Specific Uropod-Directed Microdomains in a Manner Dependent on Its MA Highly Basic Region”. *Journal of Virology* 87.11 (2013), pp. 6441–6454. DOI: 10.1128/JVI.00040-13.

[203] W. Vandenberg et al. “Diffraction-unlimited imaging: from pretty pictures to hard numbers”. *Cell and tissue research* 360.1 (2015), pp. 151–178. DOI: 10.1007/s00441-014-2109-0.

[204] K. Kwakwa et al. “easySTORM: a robust, lower-cost approach to localisation and TIRF microscopy”. *Journal of biophotonics* 9.9 (2016), pp. 948–957. DOI: 10.1002/jbio.201500324.

[205] H. Ma et al. “A simple and cost-effective setup for super-resolution localization microscopy”. *Scientific reports* 7.1 (2017), p. 1542. DOI: 10.1038/s41598-017-01606-6.

[206] B. Diederich et al. “Using machine-learning to optimize phase contrast in a low-cost cellphone microscope”. *PloS one* 13.3 (2018). DOI: 10.1371/journal.pone.0192937.

[207] H. P. Babcock. “Multiplane and Spectrally-Resolved Single Molecule Localization Microscopy with Industrial Grade CMOS cameras”. *Scientific reports* 8.1 (2018), p. 1726. DOI: 10.1038/s41598-018-19981-z.

[208] P. Almada et al. “Automating multimodal microscopy with NanoJ-fluidics”. *Nat. Commun.* 10 (2019), p. 1223. DOI: 10.1038/s41467-019-09231-9.

[209] B. Diederich et al. “cellSTORM-cost-effective super-resolution on a cellphone using dSTORM”. *PLoS One* 14.1 (2019), pp. 1–18. DOI: 10.1371/journal.pone.0209827.

[210] P. Dedecker et al. “Widely accessible method for superresolution fluorescence imaging of living systems”. *Proceedings of the National Academy of Sciences* 109.27 (2012), pp. 10909–10914. DOI: 10.1073/pnas.1204917109.

[211] S. Duwé et al. “Expression-enhanced fluorescent proteins based on enhanced green fluorescent protein for super-resolution microscopy”. *ACS nano* 9.10 (2015), pp. 9528–9541. DOI: 10.1021/acsnano.5b04129.

[212] S. Geissbuehler et al. “Live-cell multiplane three-dimensional super-resolution optical fluctuation imaging”. *Nature communications* 5 (2014), p. 5830. DOI: 10.1038/ncomms6830.

[213] T. Lukeš et al. “Quantifying protein densities on cell membranes using super-resolution optical fluctuation imaging”. *Nature communications* 8.1 (2017), p. 1731. DOI: 10.1038/s41467-017-01857-x.

[214] A. H. Hainsworth et al. “Super-resolution imaging of subcortical white matter using stochastic optical reconstruction microscopy (storm) and super-resolution optical fluctuation imaging (sofi)”. *Neuropathology and applied neurobiology* 44.4 (2018), pp. 417–426. DOI: 10.1111/nan.12426.

[215] G. C. Mo et al. “Genetically encoded biosensors for visualizing live-cell biochemical activity at super-resolution”. *Nature methods* 14.4 (2017), p. 427. DOI: 10.1038/nmeth.4221.

[216] F. Hertel et al. “RefSOFI for mapping nanoscale organization of protein-protein interactions in living cells”. *Cell Rep.* 14.2 (2016), p. 390. DOI: 10.1016/j.celrep.2015.12.036.

[217] R. Ando, H. Mizuno, and A. Miyawaki. “Regulated Fast Nucleocytoplasmic Shuttling Observed by Reversible Protein Highlighting”. *Science* 306.5700 (2004), pp. 1370–1373. DOI: 10.1126/science.1102506.

[218] T. J. Lambert. “FPbase: a community-editable fluorescent protein database”. *Nature Methods* 16.4 (2019), pp. 277–278. DOI: 10.1038/s41592-019-0352-8.

[219] M. S. Robbins and B. J. Hadwen. “The noise performance of electron multiplying charge-coupled devices”. *IEEE Transactions on Electron Devices* 50.5 (2003), pp. 1227–1232. DOI: 10.1109/TED.2003.813462.

[220] B. Moeyaert et al. “Green-to-Red Photoconvertible Dronpa Mutant for Multimodal Super-resolution Fluorescence Microscopy”. *ACS Nano* 8.2 (2014), pp. 1664–1673. DOI: 10.1021/nn4060144.

[221] M. Van Heel and M. Schatz. “Fourier shell correlation threshold criteria”. *Journal of structural biology* 151.3 (2005), pp. 250–262. DOI: 10.1016/j.jsb.2005.05.009.

[222] D. Li et al. “Extended-resolution structured illumination imaging of endocytic and cytoskeletal dynamics”. *Science* 349.6251 (2015), aab3500. DOI: 10.1126/science.aab3500.

[223] N. Chakrova et al. “Adaptive illumination reduces photobleaching in structured illumination microscopy”. *Biomed. Opt. Express* 7.10 (2016), pp. 4263–4274. DOI: 10.1364/BOE.7.004263.

[224] S. Shin et al. “Super-resolution three-dimensional fluorescence and optical diffraction tomography of live cells using structured illumination generated by a digital micromirror device”. *Scientific Reports* 7 (2018). DOI: 10.1038/s41598-018-27399-w.

[225] A. G. York et al. “mScarlet: a bright monomeric red fluorescent protein for cellular imaging”. *Nature Methods* 9 (2012), pp. 749–754. DOI: 10.1038/nmeth.2025.

[226] M. Lei et al. “Fast DMD based super-resolution structured illumination microscopy”. *Frontiers in Optics 2016*. Optical Society of America, 2016, FF3A.5. DOI: 10.1364/FIO.2016.FF3A.5.

[227] X. Yang et al. “Fringe optimization for structured illumination super-resolution microscope with digital micromirror device”. *Journal of Innovative Optical Health Sciences* 12.3 (2019), p. 1950014.

[228] C.-H. Lee and S.-H. Ma. “Dual-layer blazed grating fabricated by the roll-to-roll microreplication process for chromostereoscopy”. *Appl. Opt.* 51.16 (2012), pp. 3614–3621. DOI: 10.1364/AO.51.003614.

[229] N. Chakrova, B. Rieger, and S. Stallinga. “Development of a DMD-based fluorescence microscope”. *Pro. SPIE* 9330 (2015). DOI: 10.1117/12.2077677.

[230] DLPA037. *Using Lasers with DLP DMD technology*. Tech. rep. Texas Instruments, 2008.

[231] X. Chen et al. “Diffraction of digital micromirror device gratings and its effect on properties of tunable fiber lasers”. *Appl. Opt.* 51.30 (2012), pp. 7214–7220. DOI: 10.1364/AO.51.007214.

[232] R. V. den Eynde et al. “Quantitative comparison of camera technologies for cost-effective super-resolution optical fluctuation imaging (SOFI)”. *Journal of Physics: Photonics* 1.4 (2019), p. 044001. DOI: 10.1088/2515-7647/ab36ae.

[233] *Implementation of the grating search algorithm*. https://github.com/fairSIM/fastSIM-GratingSearch.

[234] M. Shaw, L. Zajiczek, and K. O’Holleran. “High speed structured illumination microscopy in optically thick samples”. *Methods* 88 (2015), pp. 11–19. DOI: 10.1364/OL.37.004603.

[235] K. O'Holleran and M. Shaw. "Optimized approaches for optical sectioning and resolution enhancement in 2D structured illumination microscopy". *Biomedical optics express* 5.8 (2014), pp. 2580–2590. DOI: 10.1364/BOE.5.002580.

[236] V. Perez, B.-J. Chang, and E. H. K. Stelzer. "Optimal 2D-SIM reconstruction by two filtering steps with Richardson-Lucy deconvolution". *Scientific reports* 6 (2016), p. 37149. DOI: 10.1038/srep37149.

[237] S. Bergmann et al. "Super-resolution optical microscopy resolves network morphology of smart colloidal microgels". *Phys. Chem. Chem. Phys.* 20 (2018), pp. 5074–5083. DOI: 10.1039/C7CP07648G.

[238] M. Karg et al. "Nanogels and Microgels: From Model Colloids to Applications, Recent Developments, and Future Trends". *Langmuir: the ACS journal of surfaces and colloids* 35.19 (2019), pp. 6231–6255. DOI: 10.1021/acs.langmuir.8b04304.

[239] *Fiji Plugin: Radial Profile Extended*. https://questpharma.u-strasbg.fr/html/radial-profile-ext.html.

[240] A. Orth et al. "A dual-mode mobile phone microscope using the onboard camera flash and ambient light". *Scientific Reports* (2018). DOI: 10.1038/s41598-018-21543-2.

[241] M. A. Bruce and M. J. Butte. "Real-time GPU-based 3D Deconvolution". *Opt. Express* 21.4 (2013), pp. 4766–4773. DOI: 10.1364/OE.21.004766.

[242] B. Schmid and J. Huisken. "Real-time multi-view deconvolution". *Bioinformatics* 31.20 (2015), pp. 3398–3400. DOI: 10.1093/bioinformatics/btv387.

[243] A Descloux et al. "Combined multi-plane phase retrieval and super-resolution optical fluctuation imaging for 4D cell microscopy". *Nature Photonics* 12.3 (2018), p. 165. DOI: 10.1038/s41566-018-0109-4.

[244] W. Vandenberg et al. "Model-free uncertainty estimation in stochastical optical fluctuation imaging (SOFI) leads to a doubled temporal resolution". *Biomed. Opt. Express* 7.2 (2016), p. 467. DOI: 10.1364/BOE.7.000467.

[245] Y. Yan, M. Grossman, and V. Sarkar. "JCUDA: A programmer-friendly interface for accelerating Java programs with CUDA". *European Conference on Parallel Processing*. Springer. 2009, pp. 887–899. DOI: 10.1007/978-3-642-03869-3_82.

[246] A. O. Chertkova et al. “Robust and Bright Genetically Encoded Fluorescent Markers for Highlighting Structures and Compartments in Mammalian Cells”. *bioRxiv* (2017). DOI: 10.1101/160374.

# A. Materials and methods

## A.1. Optical setups and data evaluation

### A.1.1. Detailed component lists

The mainly used items for the fluorescence microscopes designed in this thesis can be found in tables A.1 to A.3. All the other commercial optomechanics are mainly basic components from Thorlabs like the cage system. Here, for instance, construction rods, mounting brackets and posts were utilized.

### A.1.2. SOFI analysis

#### FRC analysis for SOFI

To acquire pseudo-wide-field input data sets for the FRC analysis [46, 50, 221], images 1-5 and 6-10 of each stack were summed up. This proved enough to eliminate artifacts introduced by the blinking of the probes, but less enough to not pick up camera correlation artifacts. These arise when averaging over large amounts of acquired data (e.g. 250 frames of a SOFI stack) and manifest in high-frequency correlations far beyond the microscope's passband (and thus unphysical). They likely arise due to imperfections in the camera sensor and read-out electronics, giving rise to static noise patterns that yield high-frequency correlations.

To acquire SOFI input data sets, the full stack of 500 images was split in a blocked fashion, i.e. images 1-50, 101-150,..., 401-450 were assigned to data set A, and 51-100, 151-200,..., 451-500 were assigned to data set B, and then reconstructed with the SOFI algorithm. This blocking scheme proved necessary, as both of the simpler alternatives introduce artifacts: Splitting the stack in the middle (1-250 to A, 251-500 to B) leads to a situation where data set B is disproportionally affected by photo-bleaching. Splitting the stack in an even/odd fashion (1, 3, 5,..., 499 to A, 2, 4, 6,..., 500 to B) avoids this and would be very suitable for localization microscopy, but destroys the time correlation inherent to the data and picked up by the SOFI algorithm.

**Table A.1.:** List of the most important components of the compact 3D fluorescence microscope. The position of the optics and description of the lenses can be seen in fig. 3.1b and c.

| | component | product number |
|---|---|---|
| main optics | 473 nm laser | SN 50001, 2008<br>Spectra Physics Excelsior, USA |
| | 561 nm laser | SN 1145071.098307, 2008<br>Coherent Compass, Germany |
| | AOTF | SN 26074 and 25278, 2006<br>AA OptoElectronic AOTF, France |
| | $z$-piezo | PIFOC P-721 and E-709<br>Physik Instrumente PIFOC, Germany |
| | objective | Olympus, UPLSAPO60XO, 1.35 NA |
| | cameras | IDS$\mu$Eye UI-3060CP-M-GL Rev.2 |
| lenses | L1 | 40 mm, plano-concave |
| | L2 | 80 mm, plano-convex |
| | L3 | 30 mm, biconvex |
| | L4 | 200 mm, biconcave |
| | L5 | 20 mm, biconcave |
| | L6 | 200 mm, plano-concave |
| | L7 | 180 mm, plano-concave |
| filters and dichroics | F1 | BP 473/10 |
| | F2 | BP 561/10 |
| | F3 | BrightLine, 520/60 |
| | F4 | Chroma, ET 610/75 M |
| | F5 | BrightLine, 593/40 |
| | D1 | Semrock, LM01-503-25 |
| | D2 | Semrock, HC BS R488/561 |
| | D3 | Semrock, HC BS 560i |
| | ND | Thorlabs, NE210B |

**Table A.2.:** List of the most important components of the SOFI measurements for the direct camera comparison. The position of the optics and description of the lenses can be seen in fig. 4.1.

| | component | product number |
|---|---|---|
| main optics | microscope body | Nikon Eclipse TI2 |
| | 488 nm laser | Oxxius L6Cc laser combiner box |
| | 50/50 beamsplitter | ANR:236513, Qioptiq |
| | objective | CFI Apo TIRF 100XC, 1.49 NA |
| cameras | emCCD | Andor Ixon-Ultra 897 |
| | sCMOS | Hamamatsu Fusion |
| | CMOS | IDS$\mu$Eye UI-3060CP-M-GL Rev.2 |
| lenses | L2 | 125 mm, AC-254-125A, Thorlabs |
| | L3 or L4 | 200 mm, emCCD |
| | | 75 mm, sCMOS |
| | | 80 mm, CMOS |
| filter, dichroic | F1 | ZET405/488/561/640 nm |
| | D1 | ZT405/488/561/640rpcv2 |

**Table A.3.:** List of the most important components of the DMD-SIM setup. The position of the optics and description of the lenses can be seen in fig. 5.7a.

| | component | product number |
|---|---|---|
| main optics | diode laser | QBAIHE 523nm 100mW 12V, 532MD-100-FB-12V-2 |
| | DMD | Texas Instruments, DLP6500FYE and DLP LightCrafter 6500 Evaluation Module |
| | objective | Olympus, UPLSAPO60XO, 1.35 NA |
| | camera | IDS uEye UI-3060CP-M-GL Rev.2 |
| lenses | L1 | 30 mm, 1 inch, biconvex |
| | L2 | 150 mm, 1 inch, plano-concave |
| | L3 | Thorlabs, AC080-020-A-ML |
| | L4 | Thorlabs, AC508-200-A-ML with CXY2 |
| | L5 | Thorlabs, AC508-100-A-ML with CXY2 |
| | L6 | Thorlabs, AC508-150-A-ML with CXY2 |
| | L7 | Thorlabs, AC254-250-A-ML with CXY1 |
| polar. optics | polymer circular polarizer | Thorlabs, CP1L532 with RSP1/M |
| | pizza-polarizer | CODIXX, colorPol VIS 038 BC3 CW01 with Thorlabs, K6XS |
| other | ND-filter 10 % | Thorlabs, NE210B |
| | ND-filter 50 % | Thorlabs, NE203B |
| | high-power fiber | OZ Optics, QSMJ-A3HPC 3S-488-3.5/125-3AS |
| | dichroic mirror | Semrock, Di03-R532-t3-25x36 |
| | sample stage | Newport, M-562-XYZ |
| | filter orange | Semrock, FF01-575/59-25 |
| | filter red | Chroma, ET 632/60 M |
| | micro-controller | ATMEGA328 processor Arduino Uno board |

### SNR analysis

For the determination of the SNR value of the required SOFI images, the framework introduced in [244] was utilized. Briefly, the images used as input to the SOFI analysis are resampled to produce an uncertainty estimate of the SOFI image using the jackknife algorithm. The actual SOFI image is then divided by this estimate, which produces a per-pixel estimate of the SNR. A histogram of the pixel values or this image is then generated, revealing multiple distinct peaks (figs. A.1 to A.3). While a minimum of two peaks is expected, related to the area of the image sensor where there is no cell (at SNR=0) and related the area with the expressing cell, in practice often three distinct peaks are observed which can be related to out-of-focus parts of the sample, with the in-focus SNR at a higher value. To compare different histograms a fit with the sum of three Gaussian distributions is performed with the highest mean being reported as the SNR of the histogram.

### Spatial correlation analysis

The theory for cross-correlation SOFI was introduced in Dertinger et al. [112] (see also section 2.3.3). The formula given there for second order SOFI can be broken up in three parts: a constant determined by the behavior of the dye, a constant determined by the separation between the pixels used in the calculation and the shape of the PSF and a term depending on the location of the emitters in the sample and the PSF. This final term proves the unbiased super resolution imaging performance of the technique. To investigate if additional correlations are introduced by the microscope, the second constant (determined by the emitter separation) is compared with the theoretically proposed form.

Here, the assumption is made that other sources of correlation would not show the same dependency. For this comparison the fact is used that on average the structure being imaged should be uncorrelated to the camera at a sub-pixel level. Using this information, the sample dependent term becomes constant compared to other shifts. In practice, the full SOFI image is calculated for all shifts within a three by three grid. Afterwards, for each shift, the image is averaged to yield a single value. According to theory, a very good approximation of the dependency of this value on the distance between the pixels is described by a Gaussian curve [112]. Here, the width of the Gaussian is $\sqrt{2}$ larger than the PSF width. In practice, some points follow this curve, while some do not. The assumption at this point is that the points deviating from this behavior are being caused by additional correlation between the pixels, deriving from a source beside single molecule fluctuations. In

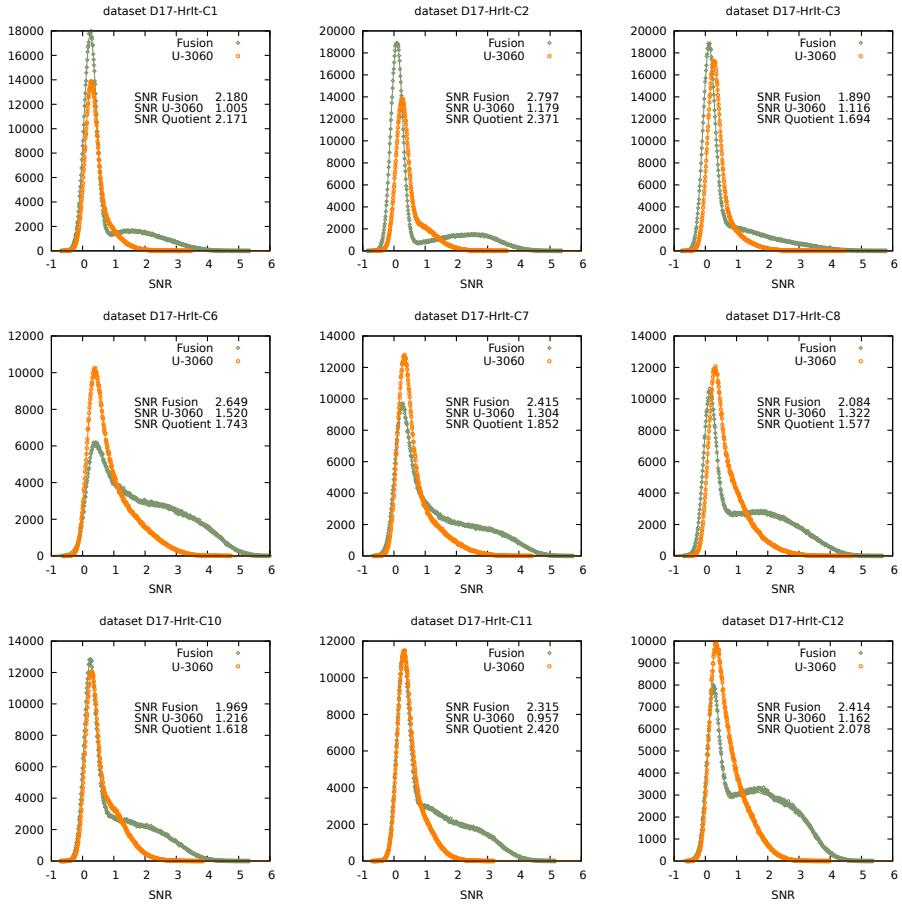


**Figure A.1.:** SNR analysis of multiple Cos-7 cells stained with ffDronpa. Each cell was imaged with the Hamamatsu Fusion sCMOS and the IDS U-3060 CMOS camera simultaneously, see fig. 4.1 for the experimental setup. For these data sets, the Fusion sCMOS camera was mounted on the reflective path of the beamsplitter, the IDS U-3060 CMOS camera was mounted on the transmission path of the splitter. In each plot, the fitted position of the signal SNR peak is quoted, and the quotient between both cameras' SNRs as SNR Fusion / SNR IDS CMOS.

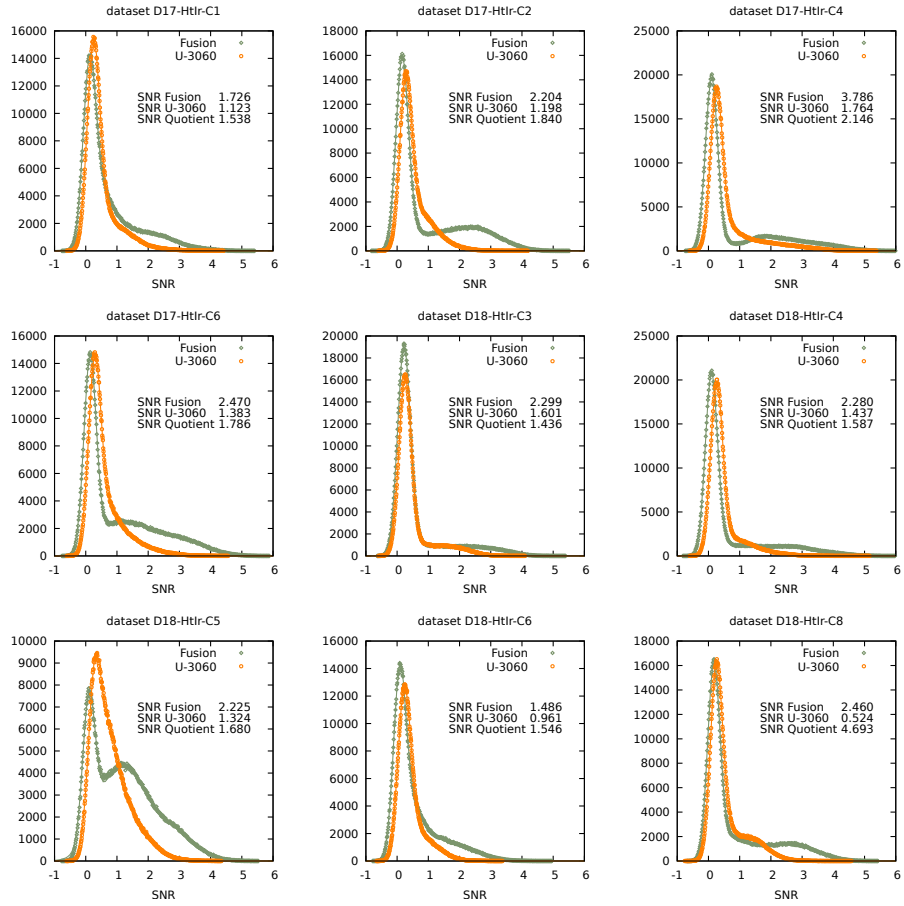


**Figure A.2.:** SNR analysis of multiple Cos-7 cells stained with ffDronpa. Each cell was imaged with the Hamamatsu Fusion sCMOS and the IDS U-3060 CMOS camera simultaneously, see fig. 4.1 for the experimental design. For these data sets, the Fusion sCMOS camera was mounted on the transmission path of the beamsplitter, the IDS U-3060 CMOS camera was mounted on the reflective path of the splitter. In each plot, the fitted position of the signal SNR peak is quoted, and the quotient between both cameras' SNR as SNR Fusion / SNR IDS CMOS.

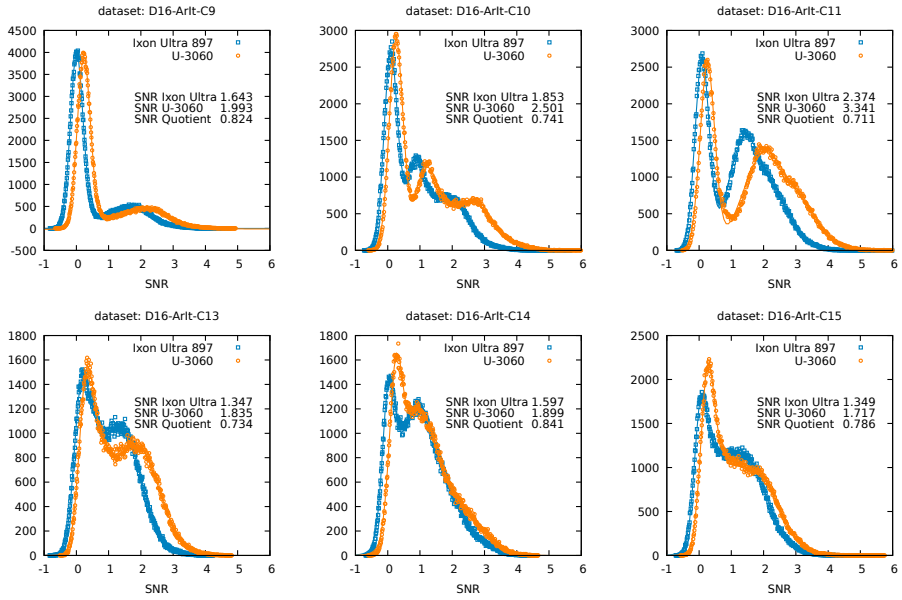


**Figure A.3.:** SNR analysis of multiple Cos-7 cells stained with ffDronpa. Each cell was imaged with the Andor Ixon emCCD and the IDS U-3060 CMOS camera simultaneously, see fig. 4.1 for the experimental design. For these data sets, the Andor emCCD camera was mounted on the reflective path of the beamsplitter, the IDS U-3060 CMOS camera was mounted on the transmission path of the splitter. In each plot, the fitted position of the signal SNR peak is quoted, and the quotient between both cameras' SNR as SNR Ixon emCCD / SNR IDS CMOS.

the practical application of this approach, these points typically show up with a higher than expected correlation, and thus do not follow the Gaussian fall-off expected for the SOFI PSF curve. Additionally, since pixel correlations introduced by the camera typically show a directionality (occurring more along the $x$- or $y$-axis of the sensor), the PSF estimation will show a 'spread' of points, with only contributions stemming from a direction exhibiting the correlation showing up as too high. In the analysis, these points are labeled as 'spurious correlation' which originate from the camera operation, and were excluded from the Gaussian fit used to extract the PSF parameters.

### A.1.3. Blazed grating angle determination software

A software package to simulate the blazed grating effect and determine the intensity distributions depending on the angle of incidence, light wavelength and SIM pattern has been created. The software is written in Java to work as a plugin to scientific image processing package ImageJ [48]/FIJI [49] and provides GPU acceleration through the jCuda framework [245]. The source code is available under an open-source (GPLv3) licence in an online repository: github.com/biophotonics-bielefeld/coherent-dmd-sim-simulator.

## A.2. Sample preparation

### A.2.1. Calibration sample

For the bead slides TetraSpeck Microspheres were purchased from Thermo Fischer in the sizes 200 nm (#T-7280) and 100 nm (#T-7219). Both bead slides were prepared the same way and will be addressed as TS. The TS stock solution was diluted with double distilled water down to a 1:10 concentration. A small droplet of approximately 1 $\mu$l was placed on a $\varnothing$12 mm coverslip and spread all over it with the pipette tip. After an incubation time of 1 h at room temperature in the dark, the droplet was dried. Now, 2 $\mu$l of glycerol was added on the coverslip and a cover glass was placed on top without getting bubbles in the glycerol. Lastly, the sample was sealed with nail polish at the edge of the coverslip on the cover glass.

## A.2.2. HIV-1 imaging

### Live-cell HIV imaging

HIV-1 samples for live-cell imaging with the compact fluorescence microscope were prepared by Lili Wang. In brief, the Jurkat-T cells (host cells) were transfected with the plasmid encoding mCherry-Gag and sfGFP-Env and incubated overnight at 37°C. Next, primary T cells (target cell) and Jurkat-T cells were mixed at a ratio of approximately 2:1 and cocultured at 37°C. After 3 h, the mixture was fixed with 4 % PFA (paraformaldehyde) diluted in PBS (phosphate-buffered saline).

### Counterstaining of fixed HIV samples

The fixed sample mixture of HIV+ Jurkat-T cells and primary T cells was suspended in PBS and stored in an Eppendorf 1 mL tube. The tube needed to be flipped carefully in order to dilute the suspended cells. Now, the tip of a pipette was cut of and used to remove 20 $\mu$L of the sample solution. The droplet was placed on a ∅12 mm coverslip and incubated at room temperature in the dark for 20 min. For the membrane stain, WGA647 (0.1 $\mu$L, 1:2000 solution) was used if sfGFP was present, otherwise FastDiO (1 $\mu$L, stock solution). In both cases, the membrane dyes incubated for 10 min within the sample mixture at room temperature in the dark. Next, the solution was completely removed, so that coverslip was nearly dry. On the localization of the cells, 4 $\mu$L Vectashield including DAPI (Vector Laboratories, #H1200) was added and a cover glass was placed on top without inducing bubbles in the Vectashield. Lastly, the sample was sealed with nail polish.

## A.2.3. SOFI samples

Cos-7 cells were cultured in DMEM (Dulbecco's Modified Eagle's Medium) supplemented with FBS (fetal bovine serum), glutamax and gentamycin at 37°C with 5 % $CO_2$. Cells were washed and detached from the growth flask using a 0.05 % Trypsin solution. The cell suspension was then seeded on 35 mm glass bottom culture dishes (#1.5 thickness, MatTek) to ensure a confluency of 50 % - 80 % for transfection. Cells were then transfected with pcDNA::MAP4-ffDronpa [121] using FuGENE6 (Promega) according to manufacturer's instructions, and cells were incubated for a maximum of 24 h before imaging. For the imaging process the media was replaced with PBS.

### A.2.4. DMD-SIM samples

#### Fixed cells

HEK293T cells were transfected for transcient expression of LifeAct-mScarlet and vLamp1-mScarlet fusions with Lipofectamine 3000 (#L3000015, ThermoFisher) according to the manufacturer's protocol. pLifeAct-mScarlet-N1 and Lamp1-mScarlet-I were a gift from Dorus Gadella (Addgene plasmid # 85054; http://n2t.net/addgene:85054; RRID:Addgene_85054 and Addgene plasmid # 98827; http://n2t.net/addgene:98827; RRID:Addgene_98827) [171, 246]. The cells were fixed 24 h post-transfection with 4 % paraformaldehyde at room temperature for 10 min.

#### Living cells

U2OS cells were stained for mitochondria or endoplasmic reticulum with respectively MitoTracker Red (ThermoFisher, #M22425) or ERTracker Red (ThermoFisher, #E34250) according to the manufacturer's protocols.

#### Core-shell microgels

The microgels were synthesized by Pia Otto and further processed by Stephan Bergmann. The core consists of PNIPMAM (poly-N-isopropylmethacrylamide) and the shell is made of PNNPAM (poly-N-n-propylacrylamide). The particles were stained with rhodamine 6G.

# B. Acronyms

| | |
|---|---|
| **AC** | auto-cumulants |
| **AFM** | atomic force microscopy |
| **AIDS** | acquired immunodeficiency syndrome |
| **AOTF** | acousto-optical tunable filter |
| **BP** | band-pass |
| **CC** | cross-cumulants |
| **CCD** | charge coupled device |
| **CMOS** | complementary metal-oxide semiconductor |
| **DMD** | digital micromirror device |
| **DMEM** | Dulbecco's Modified Eagle's Medium |
| **DNA** | deoxyribonucleic acid |
| **dSTORM** | direct stochastic optical reconstruction microscopy |
| **dWF** | deconvoluted wide-field |
| **emCCD** | electron multiplying charge coupled device |
| **ER** | endoplasmic reticulum |
| **FBS** | fetal bovine serum |
| **FCS** | fluorescence correlation microscopy |
| **FLCOS** | ferro-electric light modulators |
| **FP** | fluorescent protein |
| **FRAP** | fluorescence recovery after photobleaching |
| **FRC** | Fourier ring correlation |
| **fWF** | filtered wide-field |
| **FWHM** | full-width-at-half-maximum |
| **GFP** | green fluorescent protein |
| **GPU** | graphics processing unit |
| **HILO** | highly inclined and laminated optical sheet |
| **HIV** | human immunodeficiency virus |
| **ISMMS** | Icahn school of medicine at Mount Sinai |

| | |
|---|---|
| **LED** | light-emitting diode |
| **LP** | long-pass |
| **MOSFET** | metal-oxide-semiconductor field-effect transistor |
| **mRNA** | messanger ribonucleic acid |
| **NA** | numerical aperture |
| **ND** | neutral density |
| **NPC** | nuclear pore complex |
| **OTF** | optical transfer function |
| **PAINT** | points accumulation for imaging in nanoscale topography |
| **PALM** | photo-activated localization microscopy |
| **PBS** | phosphate-buffered saline |
| **PSF** | point spread function |
| **RESOLFT** | reversible saturable/switchable optical linear fluorescence transitions |
| **RNA** | ribonucleic acid |
| **sCMOS** | scientic-grade complementary metal-oxide semiconductor |
| **SERS** | surface-enhanced Raman scattering |
| **sfGFP** | super-folded green fluorescent protein |
| **SIM** | structured illumination microscopy |
| **SLM** | spatial light modulator |
| **SMLM** | single molecule localization microscopy |
| **SNR** | signal-to-noise ratio |
| **SOFI** | super-resolution optical fluctuation imaging |
| **SR** | super-resolution |
| **STED** | stimulated emission depletion |
| **STORM** | stochastic optical reconstruction microscopy |
| **TIRF** | total internal reflection fluorescence |
| **tRNA** | transfer ribonucleic acid |
| **TTL** | transistor-transistor logic |
| **TS** | TetraSpeck |
| **VS** | virological synapse |
| **WF** | wide-field |

# C. Publications

This work is based in major parts on the following publications and preprints:

Alice Wilking, Lili Wang, Benjamin K. Chen, Thomas Huser, Wolfgang Hübner. Imaging HIV Particles at the Virological Synapse. *G.I.T. Imaging & Microscopy*, 2017.

Author contributions: A.W. performed 3D-SIM imaging, data analysis and sample preparation. L.W. prepared the live HIV-1 samples. B.C., T.H. and W.H. conceived the project. A.W. and W.H. wrote the manuscript.

Robin Van den Eynde*, Alice Sandmeyer*, Wim Vandenberg, Sam Duwé, Wolfgang Hübner, Thomas Huser, Peter Dedecker, Marcel Müller. Quantitative comparison of camera technologies for cost-effective super-resolution optical fluctuation imaging (SOFI). *J. Phys. Photonics*, **1** (4), 2019.

Author contributions: R.V.D.E build the beam-splitting system, performed measurements and SOFI reconstructions, and wrote parts of the manuscript. A.S. performed measurements, built the freestanding microscope system, and wrote parts of the manuscript. W.V. performed SOFI reconstructions and analysis. S.D. provided the ffDronpa constructs and helped with the measurements. W.H. performed the cell transfections. P.D. and T.H. conceived of and supervised the project, and helped writing the manuscript. M.M. supervised the projects, performed data analysis, and helped writing the manuscript. All authors participated in the reading and editing of the final manuscript.

Robin Van den Eynde*, Alice Sandmeyer*, Wim Vandenberg, Sam Duwé, Wolfgang Hübner, Thomas Huser, Peter Dedecker, Marcel Müller. A cost-effective approach to Super-resolution Optical Fluctuation (SOFI) microscopy using an industry-grade CMOS camera. *bioRxiv*, 2018.

Author contributions: R.V.D.D. performed measurements and SOFI reconstructions, and wrote parts of the manuscript. A.S. performed measurements, built the freestanding microscope system, and wrote parts of the manuscript. W.V. performed SOFI reconstructions and analysis. S.D.

provided the ffDronpa constructs and helped with the measurements. W.H. performed the cell transfections. P.D. and T.H. conceived of and supervised the project, and helped writing the manuscript. M.M. supervised the projects, performed data analysis, and helped writing the manuscript. All authors participated in the reading and editing of the final manuscript.

Alice Sandmeyer*, Mario Lachetta*, Hauke Sandmeyer, Wolfgang Hübner, Thomas Huser, Marcel Müller. DMD-based super-resolution structured illumination microscopy visualizes live cell dynamics at high speed and low cost. *bioRxiv*, 2019.

Author contributions: A.S. built the DMD-SIM microscope, performed the blazed grating effect and SIM measurements, processed the SIM reconstructions, prepared samples, and wrote the manuscript. M.L. wrote the DMD simulation software, set up electronics and control software of the microscope, and wrote parts of the manuscript. H.S. helped to implemented and crosschecked math and simulation of the blazed grating effect. W.H. prepared the fixed and live-cell samples. T.H. supervised the project, and helped write the manuscript. M.M. conceived of and supervised the project, performed FRC analysis, and wrote parts of the manuscript. All authored took part in editing and approve of the manuscript.

Pia Otto*, Stephan Bergmann*, Alice Sandmeyer, Maxim Dirksen, Oliver Wrede, Thomas Hellweg, Thomas Huser. Resolving the internal morphology of core-shell microgels with super-resolution fluorescence microscopy. *Nanoscale Advances*, submitted, 2019.

P.O. performed the syntheses of the microgels, performed the Photon Correlation Spectroscopy (PCS) experiments, and wrote parts of the manuscript. S.B. performed SMLM experiments, evaluated and reconstructed the related dSTORM images and wrote parts of the manuscript. A.S. performed the SIM experiments and wrote parts of the manuscript. Maxim Dirksen conducted the atomic force microscopy (AFM) measurements. O.W. wrote parts of the manuscript and structured the whole article. T.He. and T.Hu. supervised the work and proofread the manuscript.

(*equal contribution)

# D. Acknowledgments

Mein erster Dank geht an meinen Doktorvater Prof. Thomas Huser, der es mir ermöglicht hat, diese Arbeit anzufertigen. Sein Rat und die Freiheit, die er mir in den Projekten gewährt hat, sorgten für eine angenehme und willkommene Arbeitsatmosphäre.

Weiterhin möchte ich Prof. Hütten danken, dass er ein Gutachten über diese Dissertation anfertigt. Zusammen mit Prof. Anselmetti und Prof. Borghini ist Prof. Hütten Teil der Prüfungskommission. Hierfür und für die schnelle und unkomplizierte Planung der Disputation möchte ich allen Professoren bedanken.

Ein besonders großer Dank geht an Dr. Marcel Müller, dessen großartige Unterstützung in allen Projekten dafür gesorgt hat, dass diese Promotion zu dem geworden ist, was sie ist. Seine ruhige und unermüdliche Art hat eine Zusammenarbeit sehr angenehm gemacht. Auch die Diskussionen und Besprechungen waren stets konstruktiv, was während stressigen Phasen sehr geholfen hat.

Dr. Wolfgang Hübner hat mich während der ganzen Promotion in biologischen Fragestellungen und besonders im HIV-Projekt unterstützt. Ich möchte mich bei ihm für diese Hilfe und die "Tutorials" im Labor herzlich bedanken.

Schon seit Beginn der Bachelorarbeit war Dr. Gerd Wiebusch immer da, wenn es um Anliegen bezüglich der Optik ging. Er hat während all der Jahre immer freundlich und geduldig alle Fragen beantwortet und seine Hilfe im Labor hat schon so manchen Tag gerettet. Auch bei ihm will ich mich aufrichtig für all die Unterstützung bedanken.

An dieser Stelle möchte ich den internationalen Kooperationspartnern meinen Dank aussprechen. Die Arbeit mit Robin van den Eynde sowie Dr. Wim Vandenberg von der KU Leuven im SOFI Projekt war stets unkompliziert und angenehm. Der reibungslose Ablauf im Labor und die Kommunikation hat immer gut funktioniert. Auch das Zusammenarbeiten mit Dr. Lili Wang und Prof. Benjamin Chen im HIV-Projekt hat konstant über die Jahre schön funktioniert. A huge "Thank you" to all of you!

Meinem Kollegen und guten Kumpel Stephan Bergmann danke für die sehr gute Atmosphäre in Büro und Labor. Seine geduldige Art und zum Teil nüchternen Feststellungen haben schon so manchen Tag gerettet. Die langen Abende im Büro,

wenn mal wieder eine Deadline einzuhalten war, wurden durch seine Anwesenheit wesentlich erträglicher. Auf eine gute (voraussichtliche) Zusammenarbeit in Bonn!

Henning Hachmeister und Dr. Christian Pilger waren stets hilfsbereit, wenn es um optomechanische Herausforderungen ging. Für diese Hilfe und die netten Stunden mit Kaffee in deren Büro bedanke ich mich herzlich.

Bei Mario Lachetta und Olliver Wrede möchte ich mich für die gute und erfolgreiche Zusammenarbeit in den Projekten bedanken.

Auch geht ein großer Dank an die mechanische Werkstatt der Fakültät für Physik. Die zuverlässige Anfertigung von Komponenten und deren schnelle Bearbeitung haben Wartezeiten sehr angenehm verkürzt.

Außerdem möchte ich mich bei ehemaligen Mitgliedern von D3 bedanken. Zum einen ist da Dr. Robin Diekmann, der immer einen guten Rat hatte und als Bürokollege für ein entspanntes Arbeiten gesorgt hat. Dr. Viola Mönkemöller hat besonders in der Anfangszeit der Promotion hervorragende Hilfe geleistet und war stets unterstützend. Dr. Elina Oberlander hatte immer ein offenes Ohr, wenn Dinge nicht ideal liefen. Dr. Matthias Simonis ist auch ein sehr hilfsbereiter Kollege gewesen, mit dem ich mir auch jahrelang ein Büro geteilt habe. Sein Rat über die Obstschale wird bis heute befolgt.

Selbstverständlich geht auch ein riesiges Dankeschön an die jetzigen Mitglieder von D3, mit denen die morgendliche Kaffeerunde und das mittägliche Experiment "Mensa" sehr schön und angenehm waren. Hier zu nennen sind: Anders, Stephan, Kathi, Maren, Luis, Alex, Gabriel, Oleg, Jakub, Henning und Julian - nicht zu vergessen auch Marc und Anna-Lena.

Neben der Promotion haben Sara, Kira, Alina, Anna-Lena, Flo, Daniel und Stephan dafür gesorgt, dass man bei gemütlichem Kaffee und epischen Spieleabenden den Stress der Promotion vergessen konnte, wofür ich mich herzlich bedanken möchte.

Meiner Familie und der Familie Sandmeyer spreche ich großen Dank aus für all die Unterstützung während der Promotion und das Verständnis, das mir entgegengebracht wurde.

Mein finaler Dank geht an meinem Mann Hauke, der mein Leben in jeglicher Hinsicht bereichert hat. Auch wenn er selber eine Promotion zu bewältigen hatte, so war er immer unterstützend an meiner Seite. Ich danke dir für alles!

# E. Statutory declaration

Hiermit erkläre ich,

- dass mir die geltende Promotionsordnung der Fakultät für Physik der Universität Bielefeld bekannt ist.
- dass ich die vorliegende Dissertation selbst angefertigt, dabei keine Textabschnitte von Dritten oder eigener Prüfungsarbeiten ohne Kennzeichnung übernommen und alle von mir benutzten Hilfsmittel und Quellen in der Arbeit angegeben habe.
- dass Dritte weder unmittelbar noch mittelbar geldwerte Leistungen von mir für Vermittlungstätigkeiten oder für Arbeiten erhalten haben, die im Zusammenhang mit dem Zustandekommen oder dem Inhalt dieser vorliegenden Dissertation stehen.
- dass ich diese vorliegende Dissertation oder wesentliche Teile davon nicht als Prüfungsarbeiten für eine staatliche oder andere wissenschaftliche Prüfung eingereicht habe.
- dass ich die gleiche, eine in wesentlichen Teilen ähnliche oder in eine andere Abhandlung nicht bei einer anderen Hochschule als Dissertation eingereicht habe.

Bielefeld, 31.10.2019

Alice Sandmeyer